UTS UNIVERSITY OF TECHNOLOGY SYDNEY

Dynamic Characterisation and Active Vibration Control for Improved 3D Printing Quality in Vibration-Prone Environments

by Zimu Guo

Thesis submitted in fulfilment of the requirements for the degree of

Doctor of Philosophy

under the supervision of A/Prof Benjamin Halkon and Dr Sipei Zhao

University of Technology Sydney
Faculty of Engineering and Information Technology

July 2025

Certificate of Original Authorship

I, *Zimu Guo*, declare that this thesis is submitted in fulfilment of the requirements for the award of *Doctor of Philosophy*, in the *School of Mechanical and Mechatronic Engineering*, *Faculty of Engineering and Information Technology* at the University of Technology Sydney.

This thesis is wholly my own work unless otherwise referenced or acknowledged. In addition, I certify that all information sources and literature used are indicated in the thesis.

This document has not been submitted for qualifications at any other academic institution.

This research was supported by an Australian Government Research Training Program (RTP) Scholarship doi.org/10.82133/C42F-K220.

SIGNATURE: Production Note: Signature removed prior to publication.

DATE: August 1, 2025

Abstract

Additive Manufacturing (AM), particularly fused filament fabrication (FFF), has revolutionised prototyping and small-scale production, yet deployment in dynamic or vibration-prone environments, such as in vehicles, ships, and aircraft, remains constrained. Key challenges include limited printer structural stiffness, inadequate real-time quality control, and insufficient characterisation of how external environmental disturbances affect print quality and the modal properties of FFF printed components. This thesis addresses some of these gaps through numerical modelling, simulation, and experimental validation.

In the first part, the dynamic behaviour of carbon fibre-reinforced FFF printed components was characterised through experimental modal analysis across varying infill densities and patterns. Results show that increasing infill density leads to higher natural frequencies due to enhanced effective stiffness, consistent with theoretical predictions. These measurements establish a baseline for subsequent experimental studies evaluating transportation-type vibrations - with identical acceleration levels but distinct frequency contents - on surface quality and dynamic behaviour of 3D printed parts. Low-frequency dominant vibrations resulted in the highest surface roughness, measured at 11.29 µm, due to increased relative motion between the print head and build plate. An image-based method for assessing surface roughness and waviness was developed and validated.

In the second part, the thesis investigates active vibration control (AVC) for stepper motor-driven systems commonly found in small-scale FFF. For a moving stage linear positioning system with time-varying dynamics, a customised piezoelectric stack actuator was integrated, and a feedback affine projection least mean square (FbAPLMS) algorithm was proposed to handle scenarios with low correlation between reference and target signals. Simulations showed that the FbAPLMS algorithm achieved a 5.2 dB reduction, 3 dB

more than feedforward APLMS, with effective suppression of low-frequency noise below 40 Hz while maintaining stability under dynamic conditions. To manage time-varying secondary paths, an online switching scheme among pre-identified secondary path models improved system stability and delivered a 4 dB reduction at the dominant 1664 Hz harmonic, with an overall 2 dB of reduction.

Finally, feedforward AVC using the filtered-x least mean square (FxLMS) algorithm was experimentally demonstrated on an FFF printer subjected to external vibrations. Across multiple disturbance scenarios, the controller reduced the vibration power spectral density by more than 1.6 dB and improved surface quality by over 20%. Overall, the thesis presents a coherent framework for dynamic characterisation and active vibration control in 3D printing, demonstrating that high-precision desktop FFF is achievable in challenging environments and extending AM toward reliable, on-demand fabrication in the field.

Declaration of using generative AI

During the preparation of this thesis, the author used OpenAI ChatGPT [1] to identify and correct grammatical issues. All content was subsequently reviewed and edited by the author, who takes full responsibility for the final text.

Acknowledgments

First and foremost, I would like to express my deepest gratitude to my principal supervisor, A/Prof. Benjamin Halkon and my co-supervisor, Dr Sipei Zhao, for their continued guidance, support, and encouragement throughout this research. Their expertise, mentorship, and thoughtful feedback have been invaluable to my academic and personal growth. I am especially grateful for the life skills I have developed under their supervision over the past few years.

I gratefully acknowledge the financial support provided by the China Scholarship Council and the University of Technology Sydney, which made this research possible.

I would also like to thank the members of the Centre for Audio, Acoustics and Vibration. In particular, I am grateful to my colleagues, Dr Tong Xiao and Dr Qiaoxi Zhu, whose insights have enriched this research. I am especially thankful to Dr Zhu for vital technical assistance and encouragement during the more challenging phases. I also thank the university's technical staff for their expert help with equipment and experimental setups throughout my studies.

Finally, I extend my deepest gratitude to my parents and family for their unwavering love and support throughout this journey, despite the distance that separates us. I am also deeply thankful to my girlfriend for her patience, understanding, and constant encouragement, and to my friends in Sydney for making this experience memorable and meaningful.

Table of Contents

List of Figures

FIGURE **Page**

List of Tables

CHAPTER 1

Introduction

1.1 Additive manufacturing (AM) overview

Additive manufacturing (AM), commonly termed as 3D printing, represents a transformative class of advanced manufacturing technologies characterised by layer-by-layer material deposition. The foundation of modern AM was established with the invention of stereolithography (SLA) by Charles W. Hull in 1984, which was later patented in 1986 [2]. This process integrates lithographic techniques with computer-aided design (CAD) and computer-aided manufacturing, enabling the fabrication of three-dimensional objects through layer-by-layer solidification and bonding.

Figure 1.1 illustrates a schematic of Hull's SLA system. The setup includes a container (1) filled with UV-curable resin (2), forming a working surface (3). A programmable UV light source (4) directs a focused beam (5) onto the surface via an optical scanning system, with positioning controlled by a computer (6). A motorised elevator platform (7) moves incrementally within the container, enabling layer-by-layer fabrication. As the process advances, successive cured layers (8a, 8b, 8c) integrate to form the final three-dimensional object (8) with high precision. SLA revolutionised manufacturing by enabling rapid prototyping (RP) and direct fabrication of complex geometries, overcoming the limitations of traditional subtractive and formative manufacturing techniques.

This technology has since then diversified into various other methods,

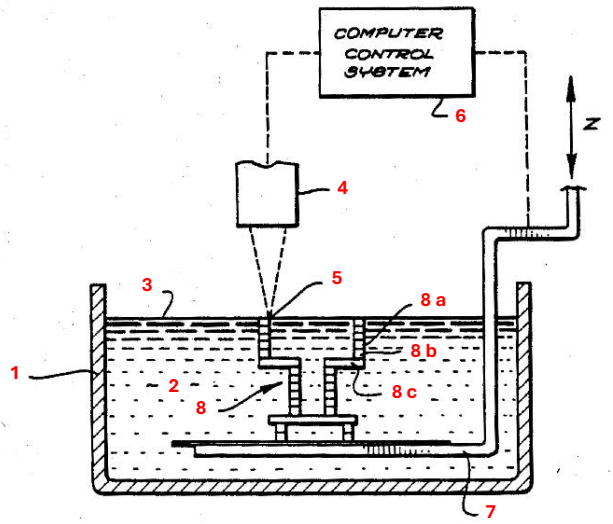

Figure 1.1: Schematic of the SLA designed by Charles W. Hull in 1984 (modified from [2])

including powder bed fusion, fused deposition modelling, and inkjet printing [3]. With the rapid expansion of the global market, the adoption of AM is increasing in both industrial and domestic settings, and its market value is projected to reach US$ 31 billion by the end of 2024 [4]. Key advantages of AM include RP, low energy consumption, accessibility, and cost-effectiveness [5, 6]. According to the ISO/ASTM 52900 standard, AM processes are classified into seven categories: Binder Jetting, Directed Energy Deposition (DED), Material Extrusion (MEX), Material Jetting, Powder Bed Fusion (BPF), Sheet Lamination, and Vat Photopolymerisation (VPP) [7]. Among these, MEX and VPP are the most commonly used and cost-effective methods. VPP includes techniques such as stereolithography and digital light processing, while MEX mainly includes Fused Filament Fabrication (FFF), also known as Fused Deposition Modelling (FDM). FFF has become the dominant small-scale AM technique due to its affordability, compact size and straightforward operation [5, 8].

1.2 Desktop-scale FFF and its challenges

Despite the advantages of FFF, various challenges are linked to this technique. Small- or desktop-scale FFF 3D printers are limited in print scale, making

them unsuitable for large-scale industrial manufacturing [9]. The two main aspects investigated here are the processing materials on the dynamic properties of FFF, and the internal and external vibration-induced error in the FFF printed parts. Firstly, variability in materials, process parameters, and build environment results in relatively poor repeatability, even when using identical geometric setups [10, 11]. More importantly, the lack of quality control of the process and the characterisation of printed parts are significant challenges of this manufacturing technique [12, 13, 14]. This is probably due to the nature of the relatively small scale of FFF, as compared to large-scale AM, such as DED and PBF, which are not likely to be influenced by the structural resonances of the system during operation. In conventional Cartesian desktop FFF, the relative motion between a build plate and a print head is always in the form of translation and is generally limited to three degrees of freedom (DOF), with a fixed fabrication orientation along the z-axis. This extrusion-based printing method introduces several drawbacks, including poor surface finish due to the layer-by-layer deposition process, anisotropic mechanical properties influenced by the build orientation, and the need for support materials to fabricate overhanging structures.

In FFF, the three most common motion mechanisms are the bed-slinger, moving gantry, and CoreXY architectures. In the bed-slinger configuration, the print head moves along the x-axis, while the build plate moves along the y-axis. The x-gantry is elevated in the z-direction by lead screws. This design is simple and cost-effective, but suffers from limited print speed and positional accuracy due to the inertia of the moving build plate. An example of the bed-slinger FFF printer is shown in **Figure 1.2a**. By contrast, the moving gantry mechanism uses two orthogonal gantries to control the x- and y-axis motions of the print head separately, while the build plate moves solely along the z-axis. This arrangement reduces the moving mass compared to the previous arrangement, as the stepper motors that control the x- and y-axis motion are moved to the stationary frame. The reduction in moving inertia enables smoother and more precise motion control, thereby improving positional accuracy. An example of the moving gantry FFF printer is presented in **Figure 1.2b**. In comparison, the CoreXY mechanism may appear similar to the moving gantry mechanism, but it operates on a different kinematic principle. Instead of relying on two mechanically independent orthogonal axes, CoreXY uses two stationary motors

and a pair of crossed belts that couple the x- and y-axis motions through kinematic coordination. This compact and rigid design minimises the moving mass, which allows high acceleration and printing precision, while requiring careful mechanical alignment and belt tensioning. An example of the CoreXY FFF printer is shown in **Figure 1.2c**. These three architectures represent the dominant motion configurations among desktop-scale FFF printers, each offering distinct trade-offs between mechanical simplicity, dynamic stability, and achievable print speed.

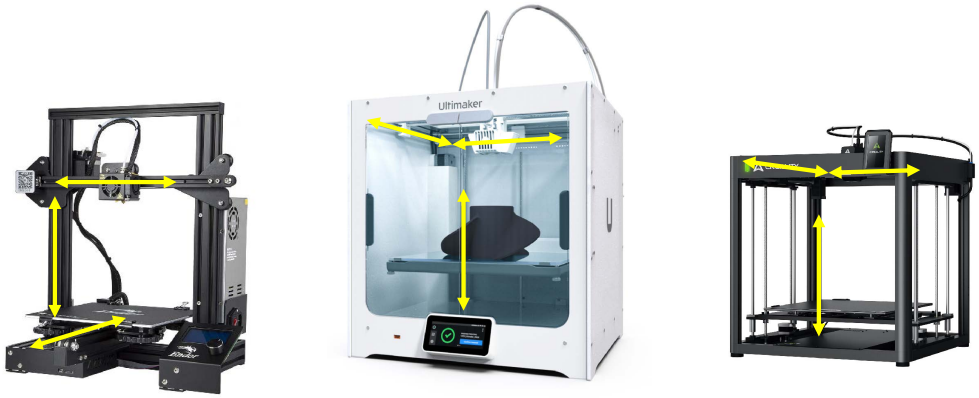

(a) (b) (c)

Figure 1.2: Examples of three FFF motion mechanisms: (a) bed-slinger [15], (b) moving gantry [16], and (c) CoreXY [15]. The yellow arrows represent directions of motion.

During the printing process of FFF, a thermoplastic filament is heated to a semi-liquid state and extruded through a nozzle, depositing material layer by layer according to a toolpath generated from computer slicing software, which is derived from a designed CAD model. Each deposited layer fuses with the previous one and solidifies as it cools on the heated (or unheated) print bed, forming the final 3D object.

1.2.1 Effects of process parameters on mechanical properties

The mechanical properties of FFF products have always been one of the most significant issues of this technique, which are comparatively lower than those manufactured via traditional manufacturing. Moreover, the mechanical properties of the printed parts are anisotropic and highly dependent on the various

process parameters [17]. These parameters include processing parameters such as print speed, printing temperature, structural parameters such as layer height, infill density, raster angle, etc [5, 17]. A summary of commonly used parameters is shown in **Table 1.1**.

Table 1.1: A summary of the common FFF process parameters.

Parameters		**Description**
Processing	Printing temperature	The temperature used for printing
	Build plate temperature	The temperature used for the heated build plate
	Print speed	The speed at which printing happens
	Print acceleration	The acceleration with which printing happens
Structural	Layer height	The height of each layer
	Wall line count	The number of walls
	Wall thickness	The thickness of the walls in the horizontal direction
	Raster angle	The angle at which the filament is deposited
	Infill geometry	The pattern of the infill material of the print
	Infill density	The density of infill of the print

Many studies have established correlations between process parameters and mechanical properties of FFF-printed parts, including tensile, flexural, impact, and compression strength. For example, a comprehensive review investigated these relationships across different materials such as ABS, PLA, PEI, PC, as well as various FFF models, concluding that the mechanical properties of FFF parts are determined by the filament bonding, which is directly or indirectly affected by all process parameters [17]. Critical parameters, such as build orientation, raster angle, layer thickness, and infill percentage, have shown a strong influence on mechanical properties. In particular, small layer thickness and raster width have been found to enhance the tensile strength in printed parts.

Despite these advances, existing research faces several limitations. Most studies adopt test standards originally developed for traditional plastics, as there is currently no standardised testing protocol for 3D printed specimens.

Commonly applied standards include ASTM D638 for tensile testing, ASTM D790 for flexural testing, ASTM D256 for impact strength, and ASTM D695 for compression strength. Additionally, generating statistically validated results requires testing a large number of printed specimens following these standards. To address this, researchers have proposed predictive models to link the process parameters with mechanical properties to reduce the required number of tests. For example, the Taguchi design of experiments has been applied to reduce the number of required test specimens while optimising printing parameters based on predictive models [18, 19, 20].

Although a standard for AM process characteristics has been published [21], the lack of specific testing conditions for mechanical properties of FFF-printed parts, unlike those established for plastics, metals, and composite materials, hinders consistent characterisation and comparison. This challenge extends to 3D printed composites reinforced with fibres, which are known for their enhanced strength, stiffness, weight reduction, cost-effectiveness, and environmental benefits over polymers [22, 23, 24]. Therefore, future research should focus on developing standardised test conditions for FFF specimens, including predefined printing parameters, to enhance the reliability and reproducibility of mechanical property evaluations.

Overall, significant research efforts have focused on understanding the influence of FFF process parameters on mechanical properties using different approaches, providing insights for tailoring mechanical performance to specific applications. Nonetheless, the research reviewed above primarily focuses on the mechanical properties of 3D printed parts. The impact of process parameters on their dynamic characteristics remains underexplored in the literature. It should also be noted that many of the FFF test specimens reported in the literature are relatively small, constrained by the limited size of the build plate. The measured mechanical properties of these samples are therefore highly sensitive to geometry, and any defects introduced by vibrations during printing can further amplify such variations. These vibration-induced effects are discussed in the following section.

1.2.2 Structural vibration effects on print quality

Low print quality in FFF, characterised by poor geometrical accuracy, surface finish, and defects, remains a persistent challenge. Among the contributing

factors, system-induced vibrations generated by the print head, build plate motion, and structural resonances are major sources of dimensional inaccuracy and surface imperfection. Experimental studies have shown that vibrations during extrusion disturb the deposition path, increasing surface roughness and reducing geometric accuracy, particularly at high printing speeds [25, 26]. Surface roughness has also been associated with toolpath dynamics, where accelerations at directional changes, such as sharp corners, excite structural resonances in the printer frame [26]. In addition, printing parameters such as infill pattern also influence printer vibration profiles. Recent work employed long short-term memory neural networks to predict acceleration profiles for different infill types, which optimises printing parameters to minimise vibration-induced errors [27].

Beyond surface quality issues, print head vibrations and mechanical resonances within the printer frame can produce more severe defects, including layer shifting, delamination, and incomplete printing. **Figure 1.3** presents an example of a missed printing defect caused by structural vibrations [28]. This type of defect occurs when print head motions cause nozzle misalignment, leading to deviations from the intended deposition path [29]. As a result, the nozzle fails to extrude material accurately, generating incomplete or misaligned layers that compromise structural integrity and dimensional accuracy.

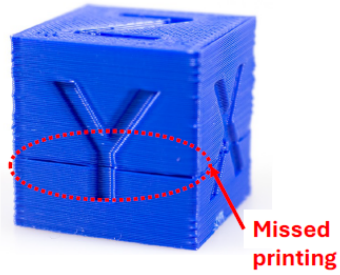

Figure 1.3: An example of missed printing on a small calibration block.

To mitigate these issues, research efforts have concentrated on two main directions: structural modification and real-time control. Structural modification aims to improve the stiffness and damping of the printer frame to reduce resonances. For example, finite element analysis has been used to predict the dynamic behaviour of the 3D printer, which allows for structural modifications to improve print quality [30]. Experimental investigations have also demonstrated that reducing modal displacement through structural adjustment

improves printing accuracy in all directions [29]. Additionally, modifications such as anti-vibration blocks, anti-vibration mounts, stiffened axis screws, and inclined rods have been shown to directly impact print quality [31]. Among these, increased frame stiffness and reduced chatter are the most effective improvements for small-scale FFF systems. Beyond purely structural reinforcement, a recent study introduced a model-based approach that uses dynamic simulation of the 3D printer gantry to develop and tune a passive mass-spring-damper system [32]. By attaching a tuned passive mass-spring-damper system to the extruder carriage of a printer gantry, the study achieved a substantial reduction in vibration-induced positional errors at higher printing speeds without the need for a closed-loop control system, which is useful to optimise passive vibration control systems prior to implementation.

In addition to hardware-based solutions, researchers have also explored online, real-time software-based control strategies to dynamically suppress structural vibrations in 3D printers. One example is the limited-preview filtered B-spline approach, which compensates for tracking errors in a desktop FFF 3D printer. This method effectively reduced vibration-induced surface waviness and layer-to-layer registration errors, while maintaining higher print speeds in a stepper motor-driven FFF printer [33]. Following this approach, a similar control strategy was applied to a delta 3D printer, which exhibits position-dependent dynamic characteristics. The results demonstrated a 39% improvement in print quality after control implementation [34]. The similar methodology was also extended to H-frame FFF 3D printers, where it led to a significant reduction in racking errors and a 43% improvement in the shape accuracy of the printed parts [35].

Together, these structural and control-based approaches demonstrate the importance of both passive and active vibration mitigation strategies. While structural modifications provide a stable foundation for reducing resonant behaviour, software-based control techniques offer adaptive, real-time corrections that further enhance print quality, especially under dynamic operating conditions.

1.3 3D printing in vibration-prone environments

The studies reviewed above primarily address laboratory conditions in which 3D printers operate in controlled, vibration-free environments. In parallel, AM has moved into sectors including agriculture, mining, maritime, and space exploration. A notable direction is on-site AM in dynamic, vibrating, and harsh environments such as vehicles [36], ships [37], aircraft, and space [38]. For example, the Danish shipping company Maersk has deployed 3D printers on vessels to produce replacement parts on board [39]. On-site printing offers several advantages: rapid mobility, continuous operational support, and digital fabrication capability in locations where traditional manufacturing facilities are unavailable. It also enhances logistical efficiency and reduces reliance on complex supply chains [40].

When the printers are operated under vibration conditions, they are exposed to continuous base excitations that vary in frequency, amplitude, and spectral content depending on the operating platform. When environmental vibration frequencies coincide with the structural modes of the 3D printer, resonance effects further amplify vibrations, exacerbating deposition errors and reducing part consistency. Small-scale FFF systems are particularly sensitive due to their relatively low stiffness. Experiments show that base excitation transmitted through the printer frame can cause layer misalignment, warping, and surface waviness even when the printer itself is functioning normally [41, 37]. In these studies, passive isolation methods were typically employed, similar to those used to mitigate structural resonances during standard printing operations.

Despite these isolated efforts, the systematic analysis of FFF printer dynamics under external vibration remains limited. Unlike lab-based manufacturing, where conditions remain stable, 3D printing in dynamic environments requires an assessment of part quality over time, as continuous exposure to vibrations can degrade equipment performance and affect print consistency [42]. Moreover, passive isolation systems (e.g., rubber mounts and damping pads) are effective only over narrow frequency ranges and degrade when vibration frequencies vary, as in vehicles and ships with changing engine speeds. Therefore, developing adaptive vibration suppression methods that can dynamically

compensate for base excitation effects is essential for reliable AM in real-world vibration environments. This gap directly motivates the research presented in this thesis.

1.4 Mechanism of active vibration control (AVC)

Vibration control techniques in structures can be broadly categorised into passive and active approaches. Classical passive vibration control methods include vibration source reduction, vibration isolation, and system modification. While these techniques can effectively reduce vibrations, they modify the structural characteristics of the system, making them less effective when operating conditions change.

To overcome these limitations, active vibration control (AVC) has been developed as an alternative to reduce mechanical vibrations by dynamically adjusting the structural response of a system in real time. An AVC system typically consists of three key components: sensors, which detect vibration, an electronic controller, which processes and manipulates the sensor signal, and actuators, which actively influence the system response based on the controller output signal. Actuators in AVC systems can be classified into semi-active and fully active types [43]. Semi-active actuators function as adaptive passive elements, capable of storing or dissipating energy rather than directly supplying mechanical power. Fully active actuators, on the other hand, supply external mechanical power to the system, enabling direct vibration suppression. Common examples include electromagnetic shakers, piezoelectric actuators, magnetostrictive devices, and electrohydraulic actuators. By generating a secondary vibrational response that interferes destructively with the primary disturbance, these actuators reduce the overall vibration. This thesis focuses exclusively on active control systems that employ fully active actuators.

AVC strategies are generally classified into feedforward, feedback, and hybrid schemes. Feedforward control measures the external disturbance before it influences the system, which requires a reference sensor that provides a time-advance signal of the primary disturbance, as shown in **Figure 1.4a**. Feedback control monitors the system response and adjusts the control signal reactively to maintain stability and reduce the vibration, so no reference sensor

is needed in feedback systems, as shown in **Figure 1.4c**. The hybrid control strategy combines both approaches to achieve a better control performance, as shown in **Figure 1.4e**.

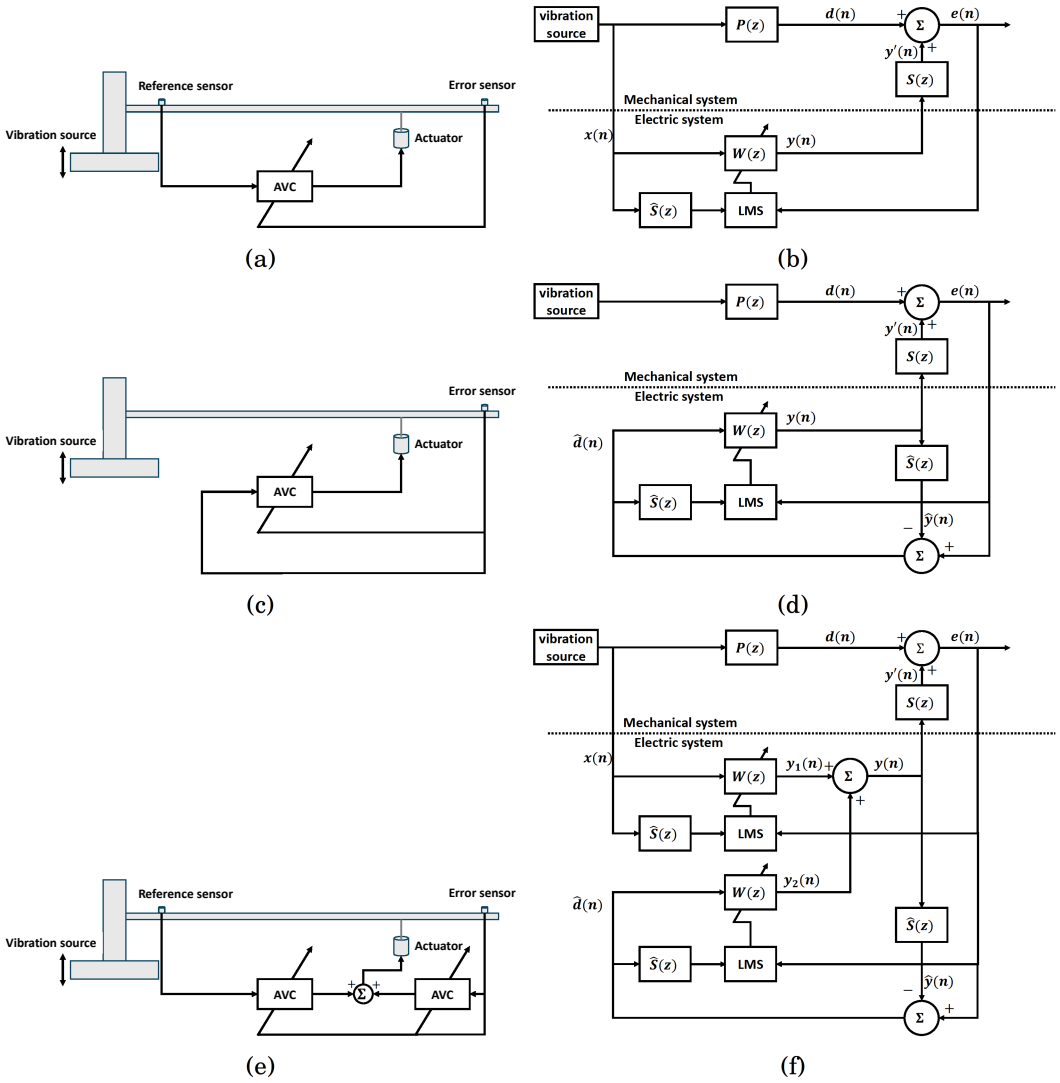

Figure 1.4: Schematics of single-channel (a) feedforward, (c) feedback, and (e) hybrid AVC systems. Block diagram of the FxLMS algorithm in single-channel (b) feedforward, (d) feedback, and (f) hybrid AVC systems.

1.5 Adaptive AVC techniques

Incorporating AVC into engineering systems has significant implications for precision manufacturing, structural health monitoring, aerospace, and auto-

motive applications, where vibration suppression is essential for performance, durability, and safety. Traditional control methods, such as PID and state-space techniques, require precise system modelling. However, due to the complexity and high dynamic characteristics of 3D printer systems, especially when process parameters vary, applying model-based control algorithms is challenging. The printer operates as a time-varying system, which is influenced by multiple process-dependent factors, making fixed-parameter control approaches ineffective.

To address this challenge, adaptive algorithms such as the least mean square (LMS) algorithm can update control output in real time, allowing the system to adapt to changing dynamics. The block diagram of the LMS algorithm in feedforward, feedback, and hybrid configurations is shown in **Figure 1.4b**, **1.4d** and **1.4f**, respectively. Among these, the feedforward filtered-x least mean square (FxLMS) algorithm has been extensively studied due to its simplicity, robustness, and lack of reliance on detailed system modelling [44]. Instead of requiring a full system model, it relies on an accurate model of the secondary path, which represents the transfer function between the actuator and the error sensor. Additionally, FxLMS utilises a reference sensor that provides signals correlated with the primary disturbance. The algorithm iteratively adjusts filter coefficients based on the error signal, continuously refining the control action to minimise vibrations. The FxLMS algorithm has been widely explored in automotive [45] and aerospace systems [46] for suppressing broadband vibrations, demonstrating its real-time adaptability to shifting disturbance frequencies [47]. Furthermore, adaptive AVC techniques tailored to dynamic environments could provide a more effective solution to 3D printing in challenging environments, ensuring real-time compensation for varying disturbance conditions and improving the quality and consistency of 3D printed parts.

1.6 Research objectives and motivations

As FFF 3D printing becomes more common, vibration-induced defects remain a primary concern. In small-scale FFF systems, vibrations from the print head, build plate motion, and the printer's own structural resonances cause dimensional inaccuracies, poor surface roughness, and variations in the modal

properties of printed parts. These problems worsen in vibration-prone environments like vehicles, ships, and aeroplanes, where external vibrations further degrade print quality.

A key challenge in FFF is understanding how process parameters influence the modal properties of printed parts. Although recent studies have increasingly examined mechanical properties, key modal characteristics, such as natural frequencies and damping ratios, are still not well understood. This knowledge gap limits the use of FFF parts in engineering applications where vibration resistance is critical.

Another persistent issue is the effect of structural vibrations on print quality. System-induced vibrations originating from the print head and build plate motion disrupt the extrusion path, leading to geometrical inaccuracies and surface imperfections. At higher printing speeds, these vibrations can excite structural resonances that lead to layer shifting, delamination, or even print failure, ultimately reducing the consistency and reliability of printed parts.

Printing in mobile or unstable environments introduces further complexities. External vibrations in vehicles, ships, and spacecraft induce resonance effects, which amplify structural vibrations and degrade print quality. Passive vibration isolation has been explored to counter such effects, but these methods are effective only within limited frequency ranges and cannot adapt to varying operational conditions, which is an important limitation for high-precision printing. Similarly, traditional control strategies require precise system modelling. However, due to the time-varying nature of 3D printer dynamics, these model-based approaches become impractical for real-time control, limiting their effectiveness in active vibration suppression.

Adaptive control algorithms offer a promising alternative because they can suppress vibrations without requiring a detailed system model. Among these, the FxLMS algorithm has demonstrated robust performance in automotive and aerospace applications due to its real-time adaptability and ability to handle broadband vibrations. However, most existing research focuses on systems with stationary or slowly varying dynamics. In contrast, systems with rapidly time-varying dynamics, such as moving stage linear positioning systems commonly found in FFF printers and CNC machines, remain relatively underexplored in the context of AVC.

This study extends AVC to the domain of 3D printing by implementing the FxLMS algorithm in an FFF system subjected to external environmental vibrations. The novelty lies not only in applying adaptive control to a new context but also in addressing the challenges posed by time-varying structural dynamics during actual printing. To the author's knowledge, this is the first experimental demonstration of real-time adaptive control for mitigating environmental vibrations in small-scale FFF, while simultaneously assessing its influence on surface quality and modal properties. The findings bridge a critical research gap and establish a foundation for enabling high-precision FFF in dynamic, real-world, challenging environments.

1.7 Thesis contributions and outline

To fill the identified gap, this thesis focuses on the characterisation of 3D printed parts and the development of an adaptive AVC framework for vibration suppression in FFF 3D printing, with a particular focus on dynamic and challenging environments. The characterisation approach serves as the basis for evaluating the performance of the AVC system, ensuring a systematic and integrated approach to enhancing 3D printing in vibration-prone environments. Overall, the findings of this research contribute to improving the precision, repeatability, and reliability of 3D printing systems, making them more suitable for on-site applications.

- **Chapter 2: Modal characteristics of Fused Filament Fabrication parts**
  This chapter investigates how FFF process parameters, especially infill density and infill pattern, influence the modal properties of 3D printed carbon fibre-reinforced specimens. While previous studies focused mainly on static strength, the modal behaviour of carbon fibre-reinforced FFF specimens remains underexplored. The novelty of this chapter lies in the combined use of experimental modal analysis and numerical modelling to predict and validate natural frequencies of the printed parts.

- **Chapter 3: Fused Filament Fabrication under environmental vibrations**
  This chapter presents the first known study to systematically assess

the effects of real-world vibration environments, simulating vehicle, shipboard, and aircraft conditions, on both the surface quality and modal characteristics of 3D printed parts. Using an electrodynamic shaker in a laboratory-based experimental setup with equivalent (root mean square) RMS acceleration but with different frequency content, the study quantifies how different types of environmental vibrations influence surface roughness and natural frequencies. The novel contribution is the identification of vibration frequency content as a critical factor affecting both external surface finish and internal structural properties during printing.

- **Chapter 4: Active Vibration Control of a moving stage system**
  Chapter 4 investigates adaptive AVC in a moving stage linear positioning system, which serves as a simplified single-axis model commonly found in 3D printers and CNC machines. A piezoelectric stack actuator (PSA) is employed to provide control forces. Owing to low coherence between reference and error signals, conventional feedforward FxLMS provides limited attenuation. To address this limitation, a feedback affine projection LMS (FbAPLMS) algorithm is proposed and shown in simulation to outperform feedforward APLMS. Furthermore, an online switching strategy is introduced to alternate between multiple pre-identified secondary path models (SPMs) corresponding to different positions along the linear guide. This approach eliminates the need for real-time secondary path modelling while maintaining system stability during the movement of the stage. Experimental results indicate that the proposed switching method significantly enhances control performance, achieving up to a 4 dB reduction in the dominant vibration harmonic at 1.6 kHz, whereas a single fixed SPM method fails to control the vibration effectively. This chapter presents a practical and effective AVC strategy for systems with time-varying dynamics.

- **Chapter 5: Active Vibration Control of a Fused Filament Fabrication 3D printer under environmental vibrations**
  This chapter presents the first experimental implementation of AVC on an FFF 3D printer operating under externally applied environmental vibrations. The FxLMS algorithm is applied in real-time, and its per-

formance is evaluated based on both structural vibration reduction and surface roughness improvement. The novelty of this work lies in applying adaptive control methods to a practical 3D printing scenario under simulated dynamic vibration conditions. The results show that AVC can reduce the print head vibration by over 1.6 dB and improve surface quality by more than 20% under different types of external vibration. This chapter demonstrates the feasibility of applying AVC to enhance FFF printing quality in mobile or on-site manufacturing environments.

- **Chapter 6: Conclusions and future work**
  The final chapter summarises the presented work in previous chapters and provides suggestions for future work.

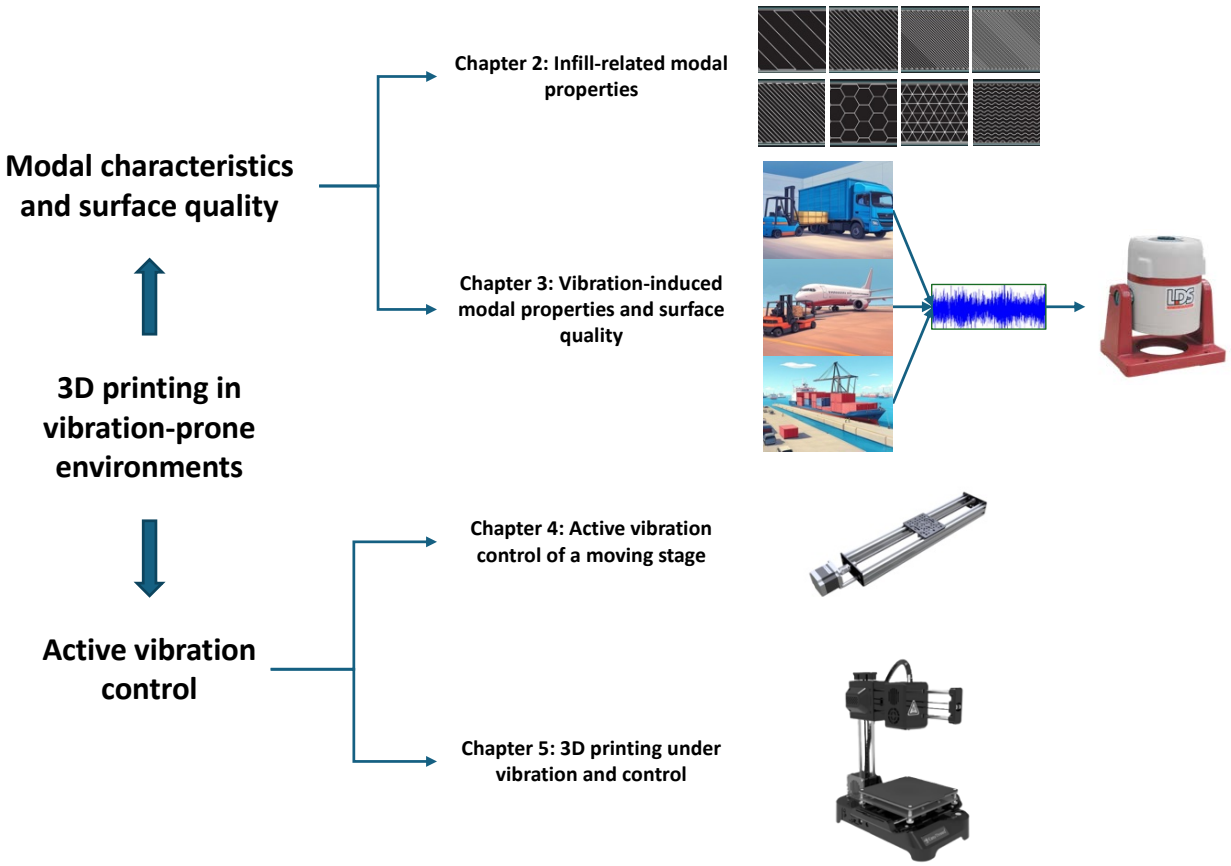

Figure 1.5: Conceptual overview of the thesis structure, illustrating the main research focus of each chapter [48].

List of papers published in the course of completing this research:

- Effects of infill parameters on the vibration characteristics of additively manufactured specimens [49] - Published in the Proceedings of the International Conference on Noise and Vibration Engineering (ISMA) 2022.
- Simulation of active vibration control of a moving stage [50] - Presented in Acoustics 2023 Sydney.
- Enhancing 3D printing quality: active vibration control for FFF in challenging environments [51]- Presented in Inter-Noise 2025.

CHAPTER 2

Modal characteristics of Fused Filament Fabrication parts

2.1 Introduction

2.1.1 Modal testing

Modal properties are among the most important characteristics in engineering structures, as they directly influence structural integrity and performance [52, 53]. Natural (modal) frequencies, modal damping ratios, and mode shapes constitute the primary modal properties of a structure. These properties characterise how structures respond to vibrational conditions and are fundamental to the field of modal analysis. Understanding modal properties enables engineers and researchers to predict structural behaviour, enhance design reliability, and mitigate issues such as resonance, noise transmission, and fatigue failure. Modal analysis involves identifying characteristics of a system in order to construct a mathematical model that describes its vibrational behaviour [54]. It can be conducted using experimental testing methods, theoretical analysis, and simulation approaches, which are often combined to ensure a comprehensive evaluation.

Modal testing is an experimental means of modal analysis. It typically involves measuring a set of frequency response functions (FRFs), either between a single excitation point and multiple response points, or conversely,

multiple excitation points and a single response location. The latter approach, often employed when using a portable impact hammer, provides flexibility and ease of testing, especially for complex or large-scale structures, where fewer transducers are required. Once the FRFs are obtained, modal parameters are extracted using curve-fitting techniques, also known as parameter estimation or modal identification methods [55]. This methodology uses the principle of reciprocity, which states that the FRF measured remains the same regardless of which point is used for excitation and response measurement, provided that the system is linear and time-invariant. This principle enables the interchange of excitation and response points, making testing more efficient. Initially, the structure must be supported in a way that approximates its intended boundary conditions, ensuring that the measured dynamic response is not significantly influenced by unintended environmental constraints. Normally, an electro-dynamic shaker or impact hammer is used to provide excitation to the test structure. The discussion here is mainly on the impact hammer, as it is easier to shift the hammer location than to reposition the accelerometer location. Additionally, the use of an impact hammer avoids the introduction of additional mass or stiffness that can occur when using a shaker and force transducer.

2.1.2 Effects of process parameters on modal properties

One of the primary challenges in FFF 3D printing is understanding how process parameters influence the modal properties of printed parts. Since the dynamic response of a structure under vibration depends on its modal properties, it is critical to understand how FFF parts behave under excitation. A number of studies have explored these characteristics using experimental modal analysis. Free vibration tests, for instance, have shown that infill density and infill orientation (raster angle) significantly affect flexural rigidity, with an optimal infill density between 10% and 20% for maximising stiffness-to-mass ratio [56]. Impact hammer tests on PLA beams revealed that natural frequency increases with higher infill percentages, while damping ratio tends to decrease as stiffness rises [57]. Other investigations on FFF beams demonstrated that layer thickness, print orientation, infill pattern, and infill percentage all affect the natural frequency. Thinner layers and flat build orientations generally led to higher natural frequencies [58].

Comparative studies on different infill patterns and densities showed that

the tri-hexagon pattern led to the highest stiffness, whereas the cross pattern yielded the best damping performance [59]. Furthermore, to quantitatively link FFF process parameters to elastic modulus, a multivariate regression model was developed using laser Doppler vibrometry [60]. Furthermore, advanced techniques such as artificial neural networks (ANN) have been employed to derive predictive models of natural frequencies by integrating experimental investigations [61], and optimisation approaches, such as the particle swarm optimisation (PSO) method [62] and the genetic algorithm (GA) method [63], have also been implemented to enhance the vibration characteristics. However, these predictive models may lack accuracy across different FFF models, as structural characteristics vary between systems. To improve the reliability of predictive models, they should account for the complex interactions between printing materials, printer architectures, and manufacturing conditions in the models [17].

Finite element analysis (FEA) has also become an important tool in AM for predicting modal properties prior to fabrication. Developing a reliable finite element model is essential for accurate vibration prediction, yet it remains challenging due to inherent print features, such as voids and imperfect layer adhesion [64]. For example, researchers have developed a parametric finite element model to simulate the impact of infill-related parameters on the natural frequency of a beam, demonstrating acceptable error compared to experimental results [64]. This model introduces a weight-frequency function, which could be extended to broader 3D printing parameters, offering a method to predict modal properties without conducting experimental validation. Similarly, comparison between carbon fibre-reinforced polyethylene terephthalate glycol (PETG) and unreinforced PETG showed a 17% increase in natural frequency due to fibre reinforcement, as verified by impact testing and FEA simulations [65].

A table summarising the reviewed studies investigating on effects of process parameters on modal properties is shown in **Table 2.1**. Furthermore, as print head and build plate vibrations depend on the specific configuration of each system, predefined predictive models often fail to identify optimal parameter combinations when applied across different FFF setups. Further research should therefore move beyond specimen-based studies and examine the modal behaviour of final FFF-printed structures under realistic operating

conditions.

Table 2.1: Summary of key studies on modal properties of FFF-printed parts

Author (Year)	Method	Processing Parameters	Modal Properties	Main Findings
Porter et al. (2019) [56]	Free vibration test	Infill density, raster angle	Natural frequency	Optimal infill 10–20% maximises stiffness-to-mass ratio; raster angle has little effect on the result.
Yadav et al. (2021) [57]; Sreedhara et al. (2015) [58]; Öteyaka et al. (2022) [59]	Impact hammer test	Infill density, infill pattern, layer thickness, build orientation	Natural frequency, damping ratio	Natural frequency increases with infill density, thinner layers, and flat build orientations. The tri-hexagon pattern yields the highest stiffness and frequency, while the Cross pattern provides superior damping performance.
Medel et al. (2021) [60]	Vibration shaker test, multivariate regression model	Build orientation, layer height, raster angle	Natural frequency	Multivariate regression model exhibited close agreement (within 11% error) with experimental natural frequencies.

Continued on next page

Author (Year)	Method	Processing Parameters	Modal Properties	Main Findings
Ali and Chowdary (2019) [61]; Chowdary and Ali (2023) [63]	Impact hammer test, ANN model, GA optimisation	Raster angle, air gap, build orientation, number of contours	Natural frequency	Lower raster angle and air gap, combined with higher build orientation and more contours, increase natural frequency. ANN model predicted natural frequencies within 5% error, while the GA further optimised parameters to achieve maximum frequencies.
Ekerer et al. (2024) [62]	Free vibration test, ANN-PSO model	Print speed, infill pattern, layer thickness	Natural frequency	Lower print speed and layer thickness with triangular infill produced the highest natural frequencies. ANN-PSO predictive model achieved an accuracy within 2.3% error.
Parpala et al. (2021) [64]	FEA, vibration shaker test, linear regression model	Infill density, infill width, number of contours	Natural frequency	Higher number of contours and higher infill density decreases natural frequencies, while infill width has little impact on modal properties.

In this chapter, the effects of infill-related process parameters, including infill density and infill pattern, on the modal properties of carbon fibre-reinforced 3D printed samples are investigated through theoretical and experimental approaches. In addition, the influence of clamping force boundary conditions on the natural frequencies of these specimens is explored, which is an aspect that has not been extensively reported in the literature. The systematic investigation procedure serves as a framework for evaluating the findings presented in the subsequent chapters.

2.2 Materials and modelling approaches

2.2.1 Specimen fabrication

In this study, the specimens under investigation were fabricated using a Markforged® X7 3D printer, which is capable of printing plastic parts by embedding continuous fibre such as carbon fibre, fibreglass, and Kevlar® within a specialist plastic matrix such as Onyx® and nylon. The Onyx and continuous carbon fibre filaments were used as the printing materials. Onyx is a thermoplastic nylon material reinforced with short, chopped micro carbon fibres, which provides high strength and toughness [66]. The specimen was designed as a cuboid beam with dimensions of $120 \times 20 \times 3$ mm. The official slicer software Eiger™ was used to configure the printing parameters in this study, which are listed in **Table 2.2**. The infill percentage and the infill pattern will be mentioned in the subsequent sections. As the raster angle of the matrix could not be adjusted in the slicer software, all the printed specimens are fabricated with the default ± 45 degrees raster angle.

2.2.2 Internal microstructure modelling

Figure 2.1a illustrates one of the carbon fibre-reinforced layers within the specimen, where the blue region represents the carbon fibre material. A cross-sectional view along section A-A is shown in **Figure 2.1b**, showing the placement of one carbon fibre layer within the structure. The roof and floor layers, located at the top and bottom of the specimen, are represented in white colour. The carbon fibre-reinforced layers, marked in blue, are located at two specific locations: layers 5-6 and layers 19-20. The infill layers, also represented in

Table 2.2: Printing parameters in Eiger^{TM}.

Printing Parameters	**Value**
Layer height (mm)	0.125
Wall thickness (mm)	0.8
Wall layer number	2
fibre fill type	Isotropic
fibre angles	0
Roof layer number	4
Floor layer number	4
Total fibre layers	4
Total infill layers	12
Total number of layers	24

white but with a square grid pattern, are located in the central portion of the structure. A rectangular infill pattern was used in this section. This infill structure consists of multiple parallel lines in one direction on each layer, followed by perpendicular lines on the subsequent layer, which is similar to the roof and floor layers in the internal structure. The external walls, shown in grey, include two layers on each side, resulting in a total thickness of 0.8 mm.

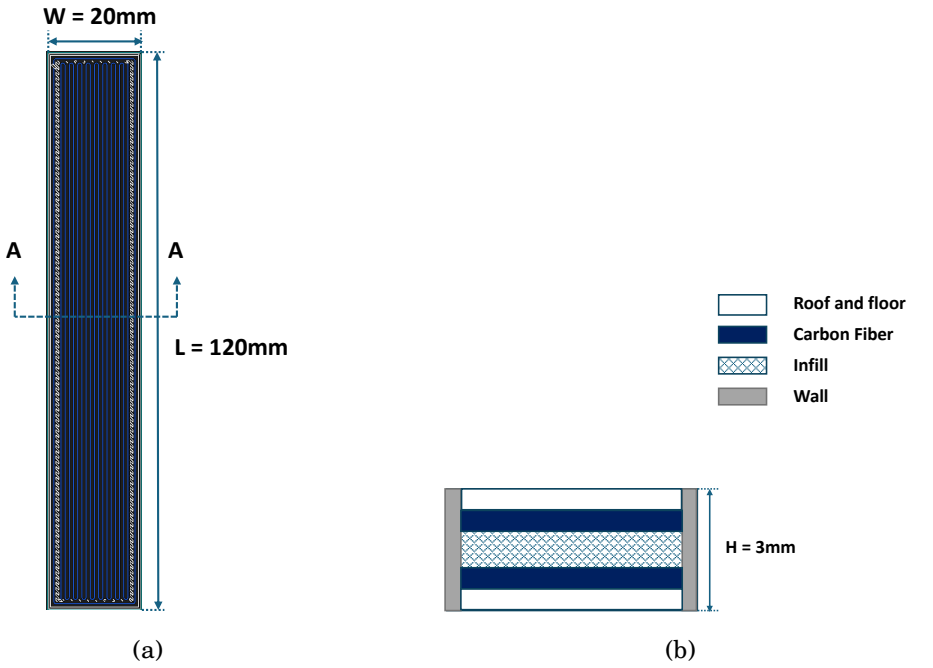

Figure 2.1: (a) Internal microstructure of one of the carbon fibre layers in the specimen. (b) Section view A-A of the specimen.

Based on the geometry, the volume of each component can be calculated with the following equations:

$$V_{infill} = h \times n_{infill} \times [W - (W_{wall} \times 2)] \times [L - (W_{wall} \times 2)] \times p \quad (2.1)$$

$$V_{roof+floor} = h \times n_{roof+floor} \times [W - (W_{wall} \times 2)] \times [L - (W_{wall} \times 2)] + V_{add} \quad (2.2)$$

$$V_{wall} = W_{wall} \times 2 \times (L + W) \times H \quad (2.3)$$

$$V_{fibre} = h \times n_{fibre} \times [W - (W_{wall} \times 2)] \times [L - (W_{wall} \times 2)] - V_{add} \quad (2.4)$$

where h is the layer thickness, n is the number of layers, W is the width of the structure, H is the height of the beam, p is the infill percentage. The term V_{add} is the additional volume of the infill, which is caused by the overlapping of infill structure in carbon fibre layers. Based on the above equations, the volume of each component for a solid specimen is listed in **Table 2.3**, where its infill percentage is 100%.

Table 2.3: Volume of each component in the solid specimen.

Components	**Volume** (mm^3)
V_{infill}	3266
$V_{roof+floor}$	2316
V_{wall}	670
V_{fibre}	948
V_{all}	7200

2.2.3 Volume average stiffness method (VAS)

The volume average stiffness (VAS) method can be used to determine the effective elastic modulus of the carbon fibre-reinforced AM samples [67, 68]. This method is particularly useful for modelling the behaviour of materials with heterogeneous microstructure. The VAS uses three main steps to predict the elastic constants. First, micromechanical models were used to determine the effective properties of each component in the 3D printed parts. Next, a coordinate system transformation was applied to the components to align their material properties with the global coordinate system of the structure. This step is essential for infill structures with different raster angles and wall structures. Lastly, the stiffness matrices were averaged based on the volume of

each component to derive the overall stiffness characteristics of the 3D printed parts.

For a transversely isotropic material as shown in **Figure 2.2**, the material properties are given by:

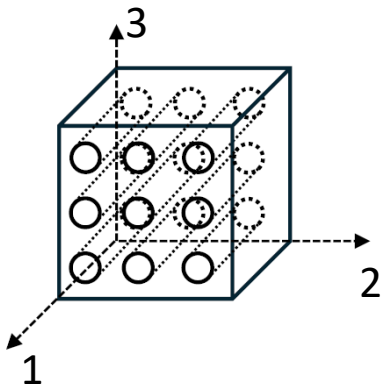

Figure 2.2: Principal material directions for 3D printed materials exhibiting transversely isotropic properties.

$$E_1 = (1-\rho_1)E \tag{2.5}$$

$$E_2 = E_3 = (1-{\rho_1}^{0.5})E \tag{2.6}$$

$$G_{12} = G_{13} = G\frac{(1-\rho_1)(1-{\rho_1}^{0.5})}{(1-\rho_1)+(1-{\rho_1}^{0.5})} \tag{2.7}$$

$$G_{23} = (1-{\rho_1}^{0.5})G \tag{2.8}$$

$$\upsilon_{12} = \upsilon_{13} = (1-\rho_1)\upsilon \tag{2.9}$$

$$\upsilon_{23} = \upsilon_{21} = \upsilon_{31} = \upsilon_{32} = (1-{\rho_1}^{0.5})\upsilon \tag{2.10}$$

where E_1, E_2, E_3 are the effective elastic moduli in directions 1, 2, and 3, E is the Young's modulus. G_{12}, G_{13}, G_{23} are the effective shear moduli in the planes 12, 13, and 23, G is the shear modulus. ρ_1 is the void density. υ_{12} is the Poisson's ratio of transverse strain in the 2-direction to axial strain in the 1-direction, and υ is the Poisson's ratio. These equations indicate that the void content has a linear effect on the longitudinal elastic modulus, while having a less pronounced effect on the transverse elastic moduli. The void content in the material has a more complex effect on the shear moduli. These relationships indicate that voids and porosities can greatly influence mechanical properties

in transversely isotropic materials such as carbon fibre-reinforced 3D printed parts.

The void density ρ_1 of the specimen is determined based on the following equation:

$$\rho_1(\%) = \frac{V_{all} - V_{th}}{V_{all}} \times 100 \tag{2.11}$$

where V_{all} is the volume of the overall designed geometry, and V_{th} is the summation of each component volume in the specimen. The volume fraction of each component and its contribution to the global stiffness matrix are calculated as:

$$[K_G] = V_i [K_i] = V_{infill} [K_{infill}] + V_{roof} [K_{roof}] + V_{floor} [K_{floor}] + V_{shell} [K_{shell}] + V_{CF} [K_{CF}] \tag{2.12}$$

where V_i is the volume fraction, and $[K_i]$ is the stiffness matrix for each component. Once the elastic properties of each component are determined, the effective elastic properties of an entire structure can be determined by inverting the global stiffness matrix [69], which is a symmetric matrix given by:

$$[S] = \begin{bmatrix} \frac{1}{E_1} & -\frac{v_{12}}{E_1} & -\frac{v_{13}}{E_1} & 0 & 0 & 0 \\ -\frac{v_{12}}{E_1} & \frac{1}{E_2} & -\frac{v_{13}}{E_1} & 0 & 0 & 0 \\ -\frac{v_{13}}{E_1} & -\frac{v_{23}}{E_2} & \frac{1}{E_3} & 0 & 0 & 0 \\ 0 & 0 & 0 & \frac{1}{G_{23}} & 0 & 0 \\ 0 & 0 & 0 & 0 & \frac{1}{G_{13}} & 0 \\ 0 & 0 & 0 & 0 & 0 & \frac{1}{G_{12}} \end{bmatrix} \tag{2.13}$$

$$S_G = [K_G]^{-1} \tag{2.14}$$

where S_G represents the effective mechanical properties of the 3D printed structures. As the raster angle of the matrix is not zero, a rotation matrix $[T]$ was introduced to align the material coordinate system with the global coordinate system of the specimen. The global stiffness matrix S_{XYZ}, representing the stiffness relative to the specimen's global coordinates, can then be obtained

as:

$$[T] = \begin{bmatrix} \cos\theta^2 & \sin\theta^2 & 0 & 0 & 0 & 2\cos\theta\sin\theta \\ \sin\theta^2 & \cos\theta^2 & 0 & 0 & 0 & -2\cos\theta\sin\theta \\ 0 & 0 & 1 & 0 & 0 & 0 \\ 0 & 0 & 0 & \cos\theta & \sin\theta & 0 \\ 0 & 0 & 0 & -\sin\theta & \cos\theta & 0 \\ -\cos\theta\sin\theta & \cos\theta\sin\theta & 0 & 0 & 0 & \cos\theta^2 - \sin\theta^2 \end{bmatrix} \tag{2.15}$$

$$S_{XYZ} = [T]^T [S'_{XYZ}][T] \tag{2.16}$$

Finally, the effective elastic modulus E_1 can be determined by inverting the top-left element in the global stiffness matrix. The material properties of Onyx and carbon fibre obtained from the manufacturer are summarised in **Table 2.4**.

Table 2.4: Material properties of Onyx and carbon fibre [66].

Material property of Onyx	**Value**	**Material property of carbon fibre**	**Value**
Elastic modulus E (GPa)	2.40	Longitudinal elastic modulus E_1 (GPa)	60.0
Shear modulus G (Pa)	0.84	In-plane shear modulus G_{12} (GPa)	2.01
Poisson's ratio υ	0.43	Poisson's ratio υ	0.10

2.2.4 Effective elastic modulus of 3D printed parts

Based on the VAS method discussed above, the effective elastic modulus of the printed specimens with different infill percentages was calculated as shown in **Table 2.5**. It is noted that specimens with rectangular infill are predicted as they are similar to normal specimens. There are four levels of infill percentage: 10%, 40%, 70%, and 100% (solid), with three specimens printed for each infill level. The higher stiffnesses for higher infill are likely due to the lower void density of these specimens, leading to tighter bonding between the carbon fibre and the Onyx matrix. The mean mass and standard deviation (SD) for three specimens of each infill percentage are measured by a scale and are also shown in **Table 2.5**.

The theoretical equivalent effective elastic modulus was calculated by dividing the theoretical effective elastic modulus by the mass of the specimen.

Table 2.5: Theoretical effective elastic modulus of specimens with different infill percentages based on the average stiffness method, with SDs shown in the brackets.

Infill density	**Effective elastic modulus (GPa)**	**Mean (SD) mass (g)**	**Equivalent effective elastic modulus (GPa/g)**
100%	8.50	7.95 (0.12)	1.07
70%	8.28	7.49 (0.17)	1.11
40%	8.20	7.04 (0.06)	1.16
10%	8.15	6.61 (0.02)	1.23

The results indicate that at 10% infill percentage, the 3D printed part demonstrates the highest equivalent effective elastic modulus of 1.23 GPa per gram. As the infill density increases to 100%, the additional infill material does not have a significant contribution to the global effective elastic modulus. This is because the carbon fibre dramatically improves the effective elastic modulus of the specimen, with a 24 times more elastic modulus compared to the Onyx material.

The theoretical natural frequencies of the specimens with the rectangular infill pattern can then be calculated using the equation of the free vibrating beam as detailed in **Appendix A.1**. The mass per unit length m and the area moment of inertia I are based on the infill percentage of the beam. The results can then be compared with the experimental frequencies, as will be shown in the subsequent section. Before the comparison, a single-sample standard tensile test following ASTM D3039 was conducted to validate the VAS method [70]. One test specimen was prepared with dimensions of $250 \times 15 \times 1.75$ mm. There are four layers of carbon fibre located in the middle of the specimen. The increased thickness tabs, including the bevels to the gauge section, are printed with steps occurring with each change in layer. The sample was tested to failure in the gauge section, ensuring the result is relevant for validation. The tensile test result indicates that the effective elastic modulus of the specimen is 16.5 GPa, while the theoretical result calculated based on the previously described VAS method is 15.6 GPa, with a difference of around 5.8%.

2.3 Modal impact test

The experimental modal analysis was implemented in this section to obtain the modal characteristics of the 3D printed specimens. A scalable automatic modal hammer (NV-TECH SAM-01) was used to excite the 3D printed specimens. The automatic impact hammer was mounted vertically on the ground, supported by multiple metal blocks to provide a stable and consistent excitation to each test specimen. A fixed-free boundary condition was applied with 20 mm of specimen length clamped by a G-clamp and two pieces of metal plate, leaving 100 mm free length for the impact test. The vibration response of the test specimen was captured by a (Polytec Portable Digital Vibrometer PDV-100) laser Doppler vibrometer (LDV). The Simcenter SCADAS Mobile data acquisition (DAQ) system was used to collect the signals during the experiment. To ensure consistent positioning during the experiment, a 3D printed slot structure was designed, as shown in **Figure 2.3a**. This structure allows precise insertion of test specimens to maintain an exact 20 mm clamp length as shown in **Figure 2.3b**, while distributing clamping force evenly across the specimen.

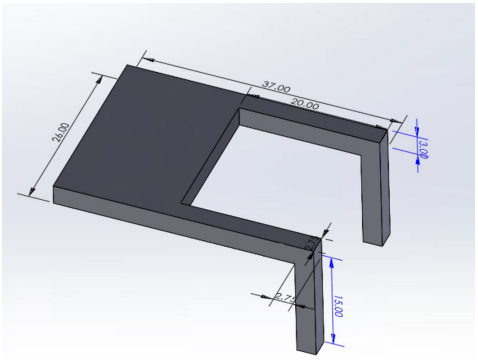

(a)

(b)

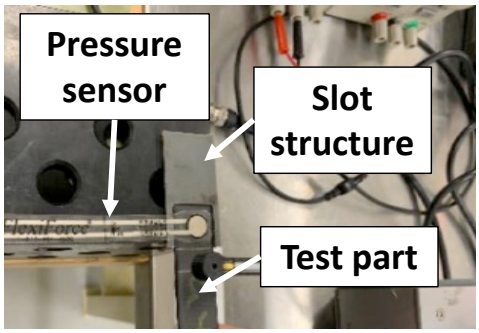

(c)

Figure 2.3: (a) Geometry of 3D printed slot structure. (b) 20 mm length slot. (c) Locations of the pressure sensor under the clamp.

Moreover, to ensure a consistent boundary condition in the experiment, a pressure-sensitive resistor (FlexiForce^{TM}) sensor was used to monitor the clamping force applied vertically to the test samples, as shown in **Figure 2.3c**. This type of sensor changes its resistance in response to applied pressure. The

sensor was powered by a power supply unit at 9 V, with the generated DC voltage measured by a multimeter. After calibration of the sensor with the potentiometer, a consistent 4 V reading was achieved for the 320 N clamping force for each specimen. The force level was determined by applying the required mass to the pressure sensor effective area to generate the same level of voltage as observed in the experiment. The complete experimental setup and a close-up view of the test specimen are demonstrated in **Figure 2.4**.

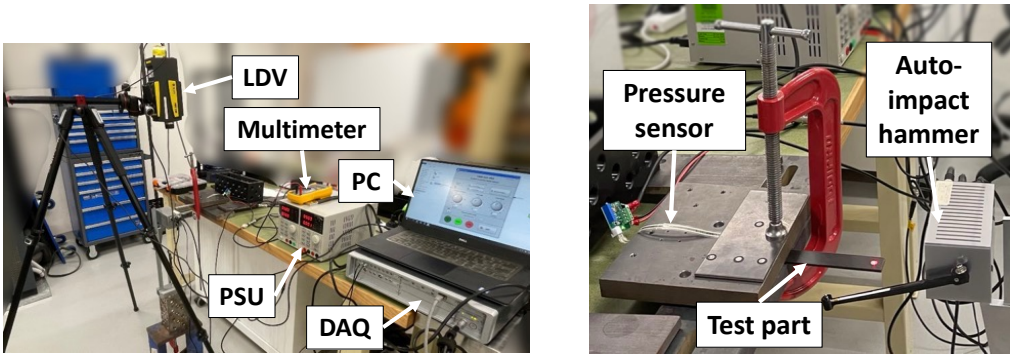

(a) (b)

Figure 2.4: (a) Overview of the experimental modal analysis setup. (b) A close-up view showing the automatic impact hammer and test specimen under the clamp.

To validate the reliability of the approximately fixed-free boundary condition in the above setup, three nominally identical aluminium specimens with a geometry equivalent to the printed specimens were prepared and tested. The differences between the experimental and theoretical frequencies determined using the equation of the free vibrating beam are within 8%. Considering that the assumptions underlying the theoretical model (e.g., material homogeneity, small deflection, and ideal boundary conditions) are not fully satisfied in the actual printed specimens and the experimental setup, the observed 8% difference between the theoretical and experimental results is considered acceptable.

The automatic impact hammer provides highly consistent, repeatable impact forces during the experiment when compared to a manual impact hammer. For each specimen, five impacts were recorded and averaged, ensuring minimal variability in the measurements. This resulted in relatively high coherence across multiple runs, an example of which is presented in **Figure 2.5**. An example of the time-domain signals from the impact hammer and the LDV is presented in **Figure 2.6**. The parameters of the automatic impact ham-

mer were configured to ensure a very short contact duration with the test specimen, which resulted in a broad excitation frequency spectrum covering the frequency range of interest. The specific settings used were as follows: excitation velocity of 1100, stop angle of 0.2°, hammer tip deceleration of 2050, pull-back acceleration of 1600, and pull-back velocity of 1000.

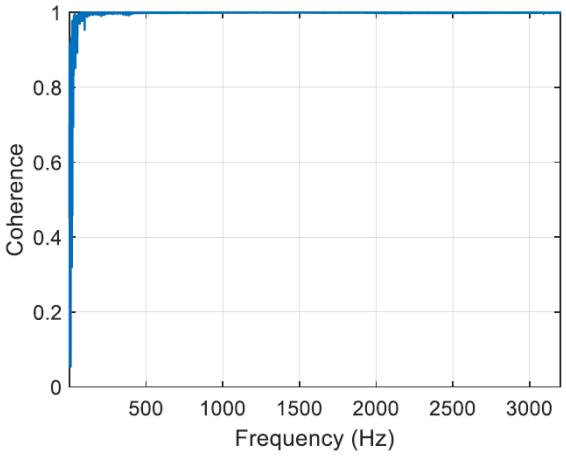

Figure 2.5: An example of the signal coherence of five runs in the impact hammer test.

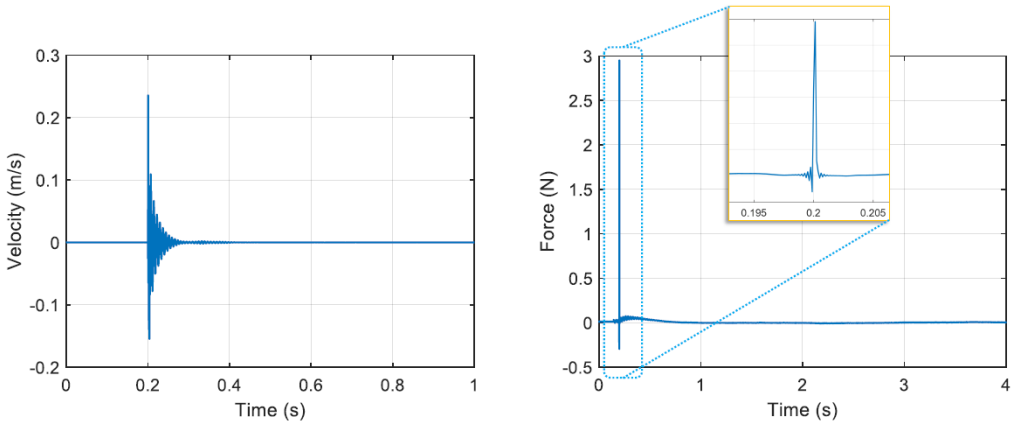

(a) (b)

Figure 2.6: Time signals of (a) LDV, and (b) automatic impact hammer during a single impact.

2.3.1 Effects of infill density on natural frequencies

In this section, the effects of different infill percentages on the natural frequencies of rectangular infill specimens are investigated. Specimens with four

levels of infill percentage were fabricated, with three copies produced for each level, as discussed in **Section 2.2.4**. The mean first three natural frequencies of three 3D printed specimens for each infill density are recorded in **Table 2.6**, with the SDs shown in the brackets.

Table 2.6: The averaged experimental natural frequencies and theoretical values for each infill density (three specimens for each infill level).

Infill density	**First natural frequency**		
	Experiment (Hz)	**Theory (Hz)**	**Difference (%)**
100%	141.7 (1.4)	134.2 (1.0)	-5.2
70%	135.8 (2.3)	134.1 (1.5)	-1.3
40%	139.8 (2.3)	135.2 (0.6)	-3.3
10%	136.8 (1.4)	136.5 (0.2)	-0.2
Infill density	**Second natural frequency**		
	Experiment (Hz)	**Theory (Hz)**	**Difference (%)**
100%	897.5 (10.1)	841.3 (6.2)	-6.3
70%	883.5 (14.6)	840.2 (9.4)	-4.9
40%	869.7 (7.5)	847.6 (3.5)	-2.5
10%	800.9 (12.3)	855.2 (1.1)	6.8
Infill density	**Third natural frequency**		
	Experiment (Hz)	**Theory (Hz)**	**Difference (%)**
100%	2438.3 (15.7)	2356.0 (17.3)	-3.4
70%	2392.0 (17.8)	2352.9 (26.3)	-1.6
40%	2193.7 (10.1)	2373.5 (9.8)	8.2
10%	1857.1 (36.2)	2395.0 (3.0)	29.0

Theoretical natural frequencies predicted from the free-vibration beam model are generally lower than experimental results across most infill densities. For the first natural frequency, the 100% infill specimen has the highest value at 141.7 Hz, while 70% infill specimen has the lowest value at 135.8 Hz. The theoretical model accurately predicts the first mode, with the differences lower than 5.2%. For the second mode, the 100% infill specimen again shows the highest value at 897.5 Hz, whereas the lowest value is found in 10% infill specimen at 800.9 Hz. Again, reasonable agreement between the experimental and theoretical natural frequencies is observed, with differences below 7%. For the third natural frequency, 100% infill specimen demonstrates the highest value at 2438.3 Hz, while 10% infill specimen has the lowest at 1857.1 Hz. A significant deviation between theoretical and experimental natural frequency occurs at 10% infill with a difference of around 29%, meaning that the theoret-

ical model has a low accuracy in predicting higher-order modes at low infill densities.

Increasing the infill density generally leads to higher natural frequencies. This observation aligns with the expectation that higher material density enhances stiffness, which outweighs the effect of additional mass and consequently increases the natural frequencies of the structure [56, 57]. Therefore, for applications requiring high structural stiffness, 100% infill is the best option. Specimens with 70% and 100% infill densities exhibit a significant increase in their third natural frequency, while the first and second frequencies remain relatively unchanged. This results in a broader frequency range, around 900 Hz to 2.3 kHz, within which no structural resonances occur. Such a bandwidth can be beneficial in applications where vibrational excitation must be avoided over a specific frequency range. For instance, components designed for environments with known excitation spectra, such as drone frames, sensor mounts, or 3D printed fixtures used in dynamic testing, could benefit from this infill-based tuning approach to avoid resonance within critical bandwidths.

Additionally, the ratio of the third natural frequency to the first for the 100% infill specimen is 17.2, compared to 13.6 for samples with 10% infill. Theoretical models predict this ratio to be around 17.6. The inconsistency in specimens suggests the current predictive model does not capture the microstructural effects at lower infill densities. The prediction model assumes perfect bonding between the fibres and matrix, whereas lower infill likely weakens layer bonding and reduces effective stiffness, lowering measured natural frequencies [71]. In addition, increased internal friction and relative movement between loosely bonded layers in low-infill structures can introduce greater damping. This added damping not only dissipates energy but also contributes to a slight reduction in the observed (damped) natural frequency compared to the theoretical (undamped) case.

The FRFs of specimens with different infill densities under impact excitation are shown in **Figure 2.7**, with shaded areas indicating SDs across multiple specimens. For low infill specimens, especially 10% infill, the phase response does not cross zero, and the magnitude response displays a smooth and broad peak at the third natural frequency. This finding suggests a lightly damped third natural frequency, as can be further confirmed by the estimated damping ratio.

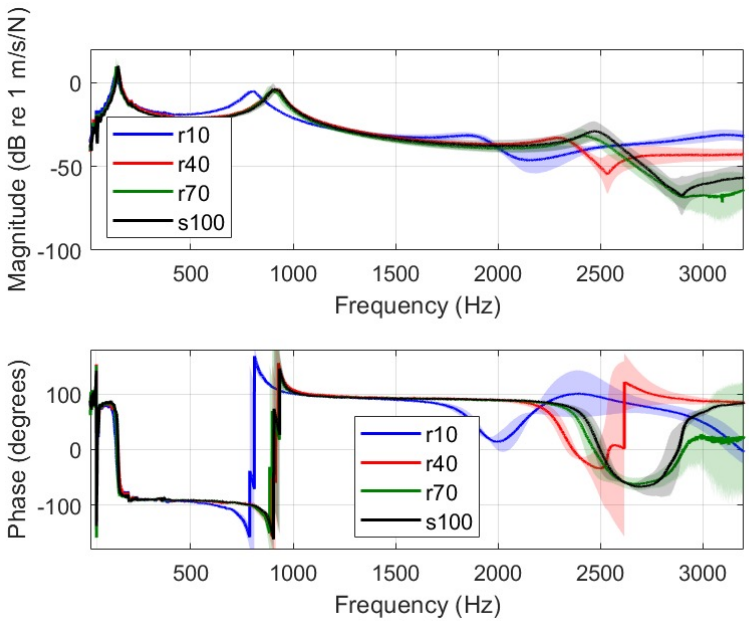

Figure 2.7: Magnitude and phase responses of different infill percentage specimens under impact test. Shaded areas represent standard deviations calculated from all specimens.

The damping properties can be estimated using the 3 dB method with the FRFs of the specimen. The damping is proportional to the width of the resonant peak, and the damping factor Q can be estimated by finding the 3 dB down from the peak of the frequency.

$$Q = \frac{f_0}{f_2 - f_1} \tag{2.17}$$

where f_0 is the resonance frequency, f_2 is the frequency value, which is 3 dB down from the resonance frequency, and higher than f_0. f_1 is the frequency value, which is 3 dB down from the resonance frequency, and lower than f_0. Then the damping ratio ζ can be calculated by:

$$\zeta = \frac{1}{2Q} \tag{2.18}$$

It should be noted that the system's structural dynamics determine the damping ratio. In this case, both the boundary condition and specimen characteristics contribute to the structural dynamics. Therefore, the damping ratios of the specimens with different infill percentages under the fixed-free boundary condition can be estimated and are presented in **Table 2.7**. The results indicate that the specimens with the lower infill percentage demonstrate a

higher damping ratio under the same boundary condition. This behaviour may be attributed to the existence of more unfilled space, which allows for energy dissipation in lower infill density specimens. It is hypothesised that the increase in damping with reduced infill percentage is due to the printed materials having more freedom to move relative to one another compared to the higher infill samples. This increased internal movement enhances energy dissipation, leading to a higher damping ratio in specimens with lower infill densities. To further validate the robustness and reliability of the observed results regarding the effects of infill density, additional experiments were conducted to examine the sensitivity of natural frequencies to variations in boundary conditions in **Appendix A.2**.

Table 2.7: The damping ratio of different infill percentages under the fixed-free boundary condition.

Infill density	**Damping ratio**		
	First mode	**Second mode**	**Third mode**
100%	0.026	0.034	0.027
70%	0.030	0.040	0.031
40%	0.044	0.038	0.048
10%	0.040	0.046	0.053

2.3.2 Effects of infill pattern on natural frequencies

In this section, the effects of different infill patterns on the natural frequencies of carbon fibre-reinforced 3D printed specimens were investigated. The similar printing parameters were used as listed in **Table 2.2**, and the experimental setup was similar to **Figure 2.4**. Four different infill patterns were examined, including rectangular, hexagonal, triangular, and gyroid infills, which are shown in **Figure 2.8**. However, different from the study in the previous section, where a broader range of infill percentages was considered, this experiment was limited to three levels of infill percentages, which were 30%, 40%, and 50%, as some infill patterns can only be fabricated within this range. Five samples were printed for each combination of the printing parameters, leading to a total of 60 samples.

The average natural frequencies of the specimens under different printing parameters are shown in **Figure 2.9**. The results indicate that the increase in

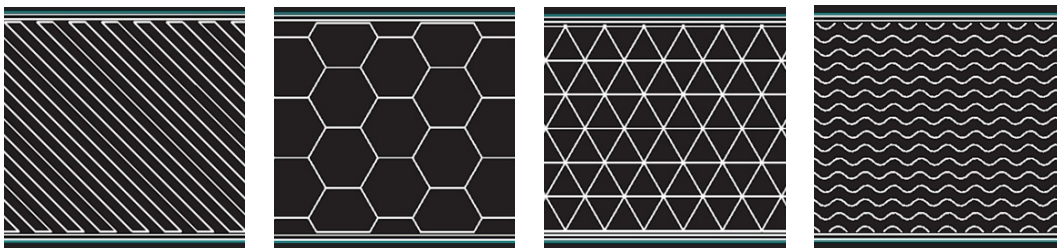

(a) (b) (c) (d)

Figure 2.8: Schematics of the four different infill patterns used in the specimen: (a) rectangular, (b) hexagonal, (c) triangular, and (d) gyroid infills.

infill density leads to an increase in all three natural frequencies in most of the specimens. This trend is because a higher infill density generally means a higher stiffness-to-mass ratio, which leads to an increase in its natural frequencies. The average natural frequencies and mass of different specimens are summarised in **Table 2.8**.

Table 2.8: Average natural frequencies and mass of different infill patterns specimens.

Infill pattern	**Infill density (%)**	**First natural frequency (Hz)**	**Second natural frequency (Hz)**	**Third natural frequency (Hz)**	**Mass (g)**
Rectangular	30	125.3	780.0	2009.3	7.26
Rectangular	40	139.8	872.1	2405.4	7.35
Rectangular	50	141.4	879.4	2432.1	7.55
Hexagonal	30	139.8	858.4	2221.9	6.82
Hexagonal	40	143.9	885.9	2446.6	6.97
Hexagonal	50	146.3	892.3	2395.7	6.59
Triangular	30	143.9	902.8	2520.2	7.07
Triangular	40	141.4	888.3	2503.2	7.41
Triangular	50	143.9	906.9	2533.9	7.14
Gyroid	30	140.6	886.7	2455.5	7.17
Gyroid	40	146.3	928.7	2575.9	7.30
Gyroid	50	140.6	893.1	2509.7	7.45

Among the four infill patterns, the rectangular infill shows the lowest natural frequencies among all infill densities. Its natural frequencies increase gradually from 30% to 50%, although the rate of increase slows as added mass offsets stiffness gains. The hexagonal infill pattern demonstrates higher

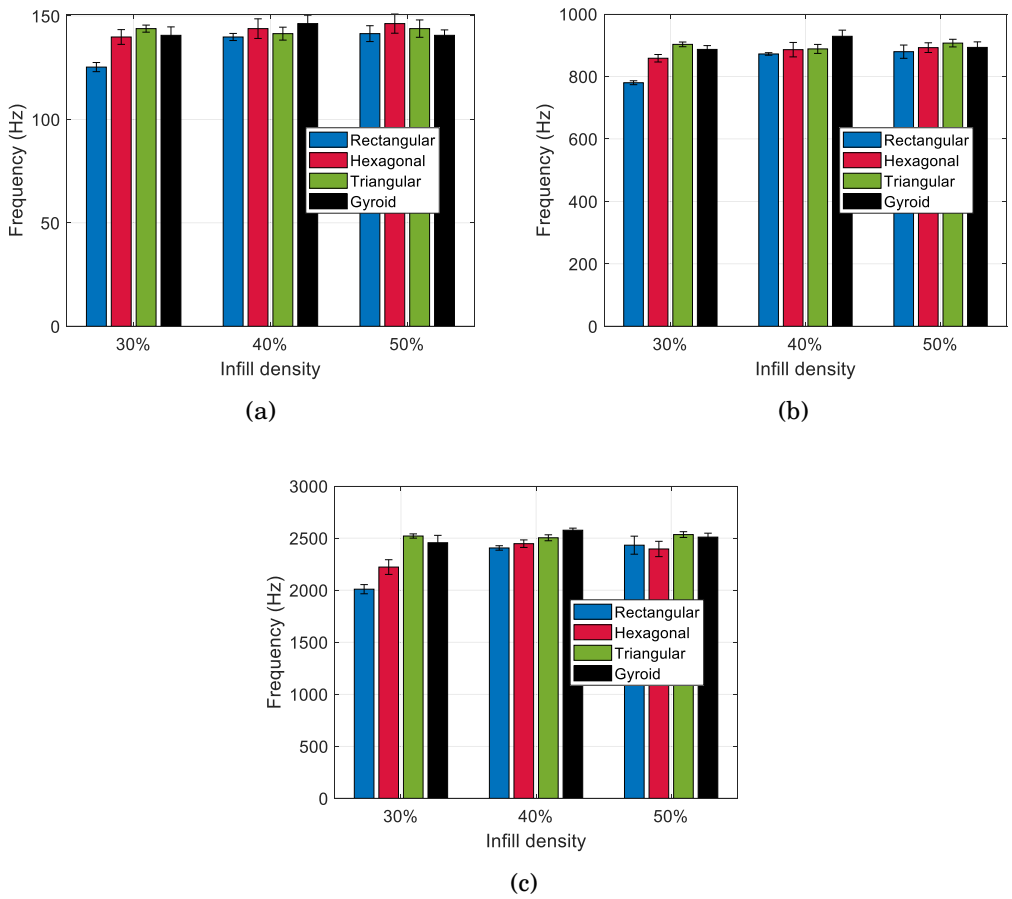

Figure 2.9: The averaged experimental (a) first, (b) second, and (c) natural frequencies of rectangular, hexagonal, triangular, and gyroid infill pattern specimens.

natural frequencies than the rectangular pattern at all infill densities, except for the third mode at 50% infill. A mass reduction is also observed when the infill density increases from 40% to 50%, which suggests a change in the internal structure at this density. Similarly, the triangular infill also shows a mass reduction when the infill density increases from 40% to 50%. This infill pattern exhibits higher second and third natural frequencies than the hexagonal pattern, but a lower first natural frequency at 40% and 50% infill. The gyroid infill achieves the highest natural frequencies at 40% infill percentage. However, the frequencies decrease when the infill percentages increase to 50% due to the reduction in stiffness-to-mass ratio.

Overall, for the first mode, gyroid at 40% infill density shows the highest first natural frequency at 146.3 Hz, and rectangular at 30% infill density

shows the lowest at 125.3 Hz. For the second mode, the gyroid at 40% infill density is the highest at 928.7 Hz, and the rectangular at 30% infill density is the lowest at 780 Hz. For the third mode, the gyroid at 40% infill density has the highest third natural frequency at 2575.9 Hz, and the rectangular at 30% infill density shows the lowest at 2009.3 Hz.

For maximum stiffness and higher modal frequencies of the specimen, gyroid at 40% infill percentage is the preferred combination. Conversely, the rectangular infill is the most flexible type of infill pattern, showing the lowest natural frequencies across all modes. On the other hand, for weight optimisation purposes, the hexagonal at 50% infill is the ideal choice as it offers the lowest mass at 6.59 g, while achieving relatively high natural frequencies. This makes it suitable for lightweight applications where vibration resistance is important.

2.4 Summary

A systematic investigation of the modal properties of carbon fibre-reinforced FFF specimens with varying infill percentages, infill patterns, and clamping forces is presented in this chapter. The results show that increasing infill density generally raises natural frequencies, which aligns with the theoretical model that higher infill density enhances the effective stiffness. However, discrepancies between experimental and theoretical natural frequencies are most evident at low infill densities, where theoretical predictions underestimate the frequency of higher-order modes. This deviation is attributed to microstructural variation and imperfect bonding, together with increased damping effects in specimens with lower infill density, all of which reduce the accuracy of the prediction of effective stiffness in the theoretical model. The damping ratio calculations further confirm that specimens with lower infill percentages exhibit higher energy dissipation. Among four different infill patterns, the gyroid infill at 40% density exhibits the highest natural frequencies, making it a suitable choice for applications requiring high structural stiffness. Conversely, the rectangular infill demonstrates the lowest natural frequencies. The hexagonal infill at 50% density offers the best balance between weight optimisation and vibration resistance.

Moreover, the influence of clamping force on natural frequencies is also

explored, demonstrating that higher clamping forces lead to increased natural frequencies, particularly in specimens with infill densities higher than 70%. The phase response analysis further indicates that low-infill specimens experience minimal change in natural frequencies under different clamping forces, especially at the third mode, which is consistent with their higher damping.

In this chapter, the Markforged® X7 3D printer was selected to manufacture the specimens used in the experimental modal analysis, as it is capable of producing continuous carbon fibre-reinforced components. This machine can ensure the precise placement of carbon fibre in Onyx® matrix, which cannot be achieved by small-scale FFF printers. Using this system also minimises the influence of structural vibration on the modal properties, which is not the primary focus of this chapter. Future work will include improving the theoretical models to account for microstructure variations at low infill densities, damping effects, and boundary conditions. More standard tensile test samples with different process parameters could be involved in verifying the theoretical model accuracy.

CHAPTER 3

Fused Filament Fabrication under environmental vibrations

3.1 Introduction

Recent advancements in AM have expanded its applications to challenging environments, while employing such methods presents significant challenges. The motions of the print head and build plate generate structural vibrations, which are transmitted through the printer's structural components, leading to significant discrepancies between the intended and actual positions of the printed part relative to the print head. These vibration-induced errors can be further amplified if the environmental vibrations coincide with the natural frequencies of the 3D printer structure. They can severely impact the quality of the final 3D printed products, resulting in a rougher surface quality and defects. Understanding the structural response of 3D printers under various environmental vibrations is crucial, especially as their applications extend into challenging environments. To date, only a limited number of studies have investigated 3D printing under realistic environmental vibrations. Consequently, establishing different types of vibration conditions for testing is essential. These conditions can be used to develop lab-based experiments that simulate real-world vibration conditions, ensuring the reliability and quality of 3D printing under such challenging environments.

In the context of vehicle environments, research on parcel delivery systems provides a practical benchmark for defining vibration conditions. Prior research has reported the RMS acceleration for parcel delivery in small and medium-sized trucks, vans, and automobiles under various road conditions [72], noting that vertical (z-axis) vibrations typically range from 0.1 to 0.2 g. This study is based on the ASTM D7386 standard, which defines performance testing criteria for parcel delivery systems to withstand the hazards of distribution environments. This standard lists the overall RMS acceleration across various bandwidths, detailed in **Table 3.1** [73]. However, a large deviation between the standard values and other real-world test data at certain bandwidths has been observed [74]. This means that modifying the vibration profiles in experimental setups to reflect real-world vehicle conditions more accurately is required. Such modification should involve vehicle types, delivery routes including speeds and road conditions, and other factors that impact the typical vibrations encountered by delivery vehicles.

Table 3.1: RMS acceleration across different bandwidths of the vertical direction for the parcel delivery system.

Frequency range (Hz)	**Vibration RMS (g)**
1-7	0.279
7-13	0.042
13-29	0.110
29-50	0.046
50-200	0.343
Total range (1-200)	0.460

While specific guidelines for evaluating vibration issues in 3D printers installed on road vehicles, marine vessels, or aeroplanes are unavailable, existing standards provide guidelines for evaluating vibration environments that materials encounter throughout their lifecycle. For example, the MIL-STD-810H standard offers guidelines for identifying potential vibration environments and recommends laboratory testing procedures to ensure material compatibility in different settings, including vehicles, ships, aeroplanes, and trains [75]. This standard can therefore serve as a reference for designing vibration testing for 3D printers. For example, it specifies a vertical vibration level of 1.08 g RMS for trucks on highway conditions. However, it should be noted that the overall vehicle structure, test object mounting structure, and object transmissibility

greatly affect the vibration [75], as demonstrated in [74]. Therefore, when conducting experimental tests on 3D printing, it is advisable to adjust the spectrum profile and vibration levels accordingly. In the literature, there is limited research on the effects of environmental vibrations on the quality of 3D printed parts. For example, researchers have found that base vibrations have a direct impact on the surface roughness of the printed parts [41]. However, there is no study on how the frequency of the vibration profile influences the print quality.

This chapter explores the impact of different types of environmental vibrations on the quality and modal characteristics of the 3D printed parts. The aim is to establish a correlation between different environmental vibration conditions and both the surface roughness and natural frequencies of the 3D printed parts.

3.2 Environmental vibration conditions

3.2.1 Vibration standard selection

This study examines various vibration conditions to simulate 3D printing in representative transportation environments. Several vibration testing standards are available for use with electrodynamic shakers, including ASTM [76], ISO, IEC, and MIL-STD. Among these, the MIL-STD-810H standard was selected as the reference for vibration testing in this study due to its comprehensive coverage of real-world environmental conditions and its widespread adoption across multiple industries [75]. Specifically, Method 514.8 of MIL-STD-810H outlines procedures for simulating mechanical vibration environments encountered during the life cycle of equipment, including transportation via ground vehicles, ships, and aircraft. This standard offers detailed vibration profiles, RMS levels, and bandwidth specifications that closely match the operational conditions investigated in this work. Compared to other available standards, MIL-STD-810H provides a broader spectrum of vibration scenarios, enabling a realistic and standardised approach to assess the effects of dynamic environments on 3D printing systems. Its application ensures that the laboratory testing conditions accurately reflect practical use cases in transportation and field deployment.

Three primary modes of transportation were considered: land vehicles, aircraft, and maritime vessels, which all have unique characteristics in both the time domain (e.g., RMS, peak-to-peak, standard deviation) and the frequency domain (e.g., frequency content, magnitude and phase response). The first condition considered was land-based transportation, specifically, the common carrier vibration profile associated with US highway truck vibration exposure was selected. This type of vibration contains a low-frequency content ranging from 5 Hz to 40 Hz with a constant amplitude, followed by an amplitude decrease from 40 Hz to 500 Hz. The second condition represents aerial transportation, and the C-5 type aircraft cargo vibration was selected. This type of vibration also exhibits low-frequency random vibration characteristics, ranging from 15 Hz to 1 kHz with a constant amplitude, and an amplitude decrease from 1 kHz to 2 kHz. The third condition is the maritime transportation, represented by a shipboard with a turbine engine. This vibration profile consists of a broadband sea vibration superimposed with multiple narrowband spikes caused by the rotation of the engine rotor. The broadband frequency is from 15 Hz to 2 kHz with a constant amplitude. The engine speed is set at 3000 revolutions per minute (RPM), which leads to the narrowband frequency to be 50, 100, 150 and 200 Hz. The spike bandwidth is ±5% of the narrowband frequency.

Despite the different frequency spectra with each vibration condition described, their overall vibration levels are normalised and adjusted to achieve a consistent RMS value in the time domain across all different scenarios. This is because the influence of frequency contents of vibrations on the print quality is the main focus of the study, rather than the effects of different vibration amplitudes on the print quality, which has been explored [25, 26]. The power spectral density (PSD) profiles of the three vibration conditions are shown in **Figure 3.1**, with the RMS level at 0.2 g. This level ensures that the 3D printer can operate without introducing significant defects in the printed parts.

3.2.2 Vibrating printer system setup

The 3D printer was subjected to three different types of environmental conditions, as previously mentioned, using an LDS V450 electrodynamic shaker in the vertical (z-axis) direction. The shaker was driven by a linear power amplifier (B&K LPA600). To mount and support the 3D printer on the shaker,

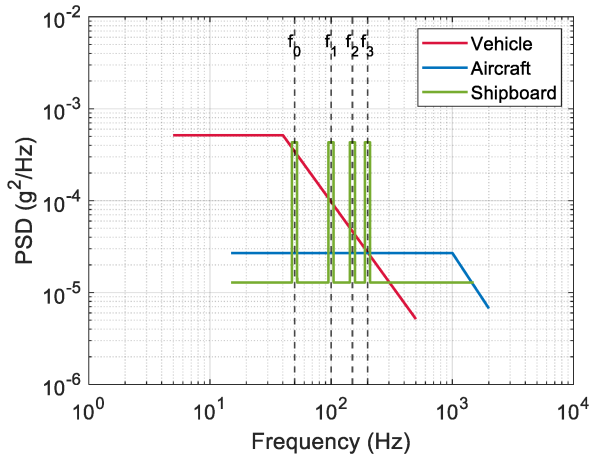

Figure 3.1: PSD of the common carrier, aircraft cargo, and shipboard random vibrations for 0.2 g RMS modified from [75].

a customised shaker fixture, also known as a head expander, was designed and manufactured in this study. Details of the customised fixture structure are provided in **Appendix A.3**. The 3D printer to be investigated in this study is an EasyThreed K7 desktop-scale FFF 3D printer, which weighs around 1.2 kg. This 3D printer model was selected due to the payload and size limitations of the shaker. According to the manufacturer's specifications, the maximum displacement peak-to-peak is 19 mm, and the axial stiffness of the armature is 17.5 $\mathrm{kN\,m^{-1}}$. Therefore, the maximum suspension force is calculated to be about 166.3 N, which corresponds to a mass limit of 16.9 kg. In this setup, the combined mass of the 3D printer, fixture, clamp, and armature is 5.7 kg. This model is one of the lightest and most compact options available on the market, making it a suitable choice for the experimental setup.

To evaluate the vibration responses of the printer at different locations, two triaxial integrated electronics piezo-electric (IEPE) accelerometers (B&K Type 4506 B) are used to measure the acceleration, one is mounted on the print head, and the other is mounted on the build plate. The entire experiment setup is shown in **Figure 3.2a**, and the locations of two accelerometers are shown in **Figure 3.2b**. An additional uniaxial accelerometer (DJB AF 100) is mounted on the surface of the customised fixture to measure the vibration level output from the shaker. This sensor is used to maintain a consistent RMS vibration level during each vibration scenario. Data acquisition and analysis are performed using a Simcenter SCADAS system alongside the Simcenter

Testlab software multiple-input and multiple-output (MIMO) FRF testing module, with a sampling frequency set at 6400 Hz for this study. During the experiment, the shaker remains operational throughout the entire printing process.

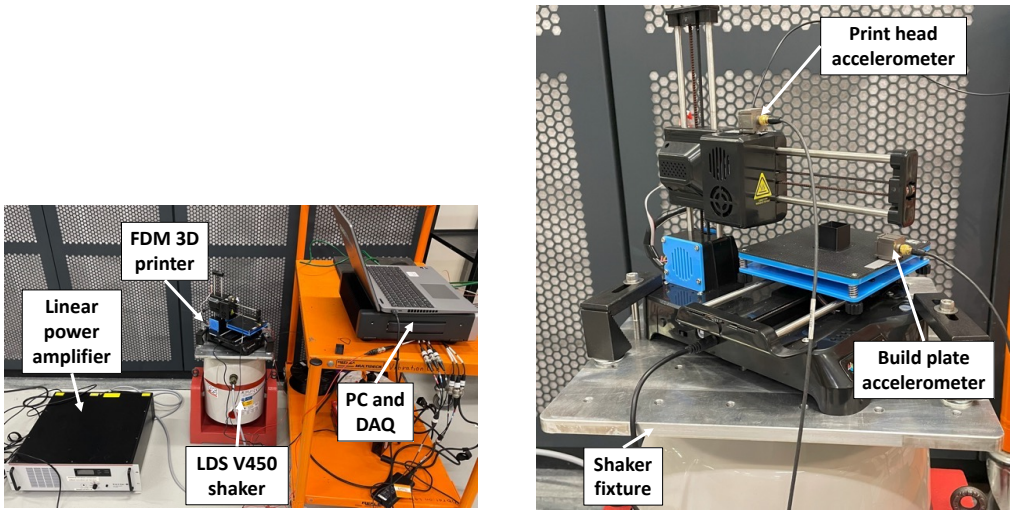

(a) (b)

Figure 3.2: (a) Entire experimental setup in this study. (b) Two accelerometer locations across the 3D printer.

The geometry of the specimen is a 20 mm cube thin-walled structure without infills and a roof on the top surface. **Figure 3.3** presents the 3D printed part visualised in UltiMaker Cura® slicer software. The same printing parameters are applied and maintained during the printing of each specimen. The yellow region at the bottom represents the floor layer, which has a 45-degree raster angle. The red region indicates the outer wall structure, and the green region represents the inner wall structure.

3.3 Printing with external shaker vibration

3.3.1 Printing without external vibration

This section examines the vibrations of the 3D printer during various operational stages without external environmental vibration, which serves as the baseline for comparison. Initially, the vibration characteristics of the 3D printer in an idle state are investigated. In this condition, the 3D printer

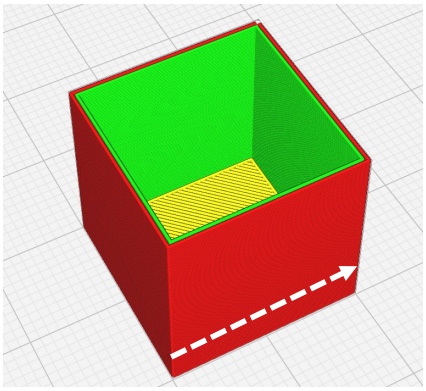

Figure 3.3: Illustration of the 3D printed object considered in this study. The white arrow indicates the surface roughness measurement direction.

was powered on but not printing, with only the motor cooling fan active. Acceleration measurements at two sensor locations indicate that the printer vibrations primarily consist of a frequency content around 230 Hz and its multiple harmonics. This vibration is attributed to the electric motor driving the cooling fan on the print head, which cools the extruder of the print head. It is important to note that, during the printing process, the print head moves along the x-axis, while the build plate moves along the y-axis.

The comparison of the vibration PSD between the print head and build plate in z-axis during different printing activities is presented in **Figure 3.4**. The PSD spectrum indicates that the print head experiences higher vibration levels compared to the build plate, especially at frequencies above 300 Hz. This is because the print head behaves as a moving mass on flexible beams, making it more prone to vibrational disturbances. Notably, the vibration at the print head is predominantly characterised by a peak at around 230 Hz, correlating with the motor of the cooling fan. In contrast, the build plate shows a dominant vibration peak at around 180 Hz, which is caused by the electric motor located at the bottom of the printer that controls the build plate movement.

Table 3.2 summarises the RMS acceleration values measured at the print head and build plate across three axes while printing on the shaker without any induced vibration. Notably, the vibration levels are higher when printing the floor layers compared to the wall structures across all three axes for both print head and build plate, which can also be observed in **Figure 3.4**. This variation is attributed to the default raster angle setup for the floor, which is 45 degrees. This angle results in larger motions compared to the wall structures,

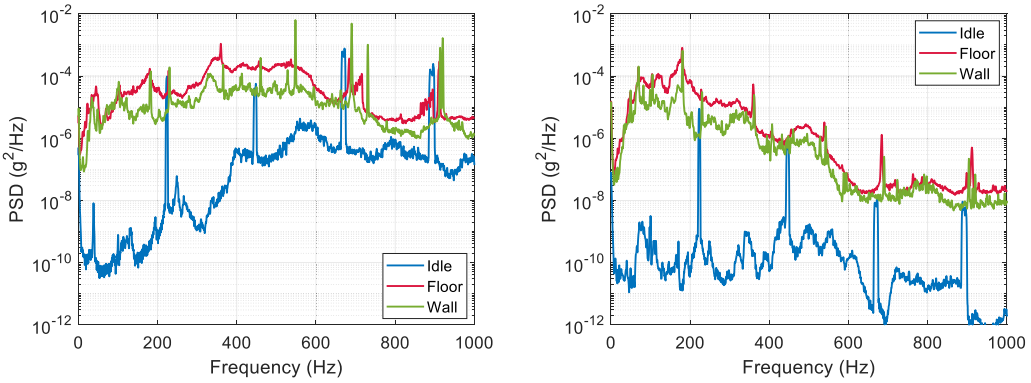

Figure 3.4: (a) PSD of the print head and (b) build plate during different printing activities in z-axis without vibration.

where printing is limited to the outer contour at 0 and 90 degrees.

Table 3.2: RMS acceleration of the print head and build plate under different printing activities without external vibration.

RMS acceleration (g)	Print head			Build plate		
	X	Y	Z	X	Y	Z
Idle	0.069	0.180	0.092	0.002	0.008	0.006
Floor	0.297	0.330	0.284	0.065	0.185	0.138
Wall	0.249	0.273	0.214	0.034	0.114	0.071

3.3.2 Common carrier condition

In this section, a 3D printing experiment was conducted under the common carrier vibration condition, and the overall RMS acceleration is 0.2 g, as detailed in **Figure 3.1**. Similar to the previous scenario, the idle state is the 3D printer powered on but not printing. However, in this case, a large level of low-frequency content below 100 Hz is observed. These are primarily due to the frequency range of the common carrier vibration, which coincides with the structural resonances of the 3D printer structure. The low-frequency resonance of the print head is around 27 Hz, while the resonance of the build plate is around 64 Hz. The comparison of the vibration PSD under common carrier vibration between the print head and build plate in z-axis during different printing activities is presented in **Figure 3.5**. Notably, the

PSD spectra indicate that the print head experiences higher vibration levels compared to the build plate at frequencies above 200 Hz.

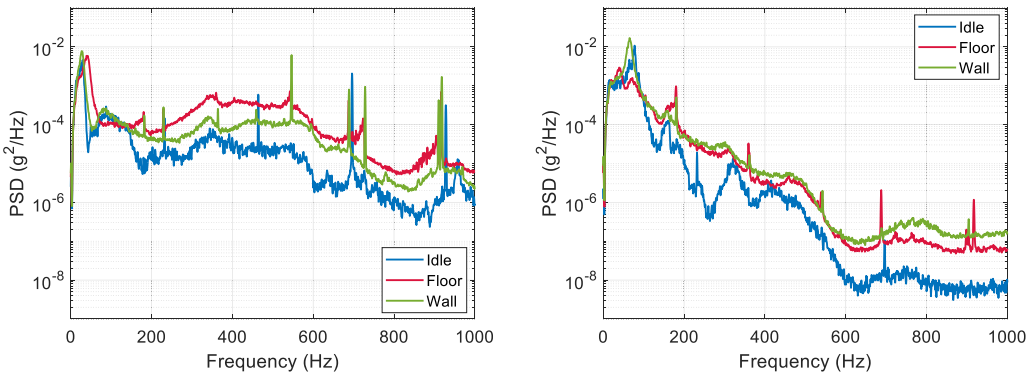

Figure 3.5: (a) PSD of the print head and (b) build plate during different printing activities in z-axis under common carrier vibrations.

Table 3.3 summarises the RMS acceleration values measured at the print head and build plate across three axes while printing different structures under the common carrier vibration condition. Notably, the build plate exhibits lower vibration levels when printing floor layers compared to the idle state, whereas the print head vibrations are largely increased compared to the idle state. However, during the printing of wall structures, both the print head and the build plate experience higher vibration levels than in the idle state. Several factors contribute to these dynamic characteristics. First, when printing the wall structure, the print head is often positioned near the midpoint of its travel range. This reduces the structural rigidity of the print head structure, making it more prone to vibrations. Second, the common carrier vibration is mainly composed of low-frequency contents, which induce a high level of displacement and lead to interaction between the build plate and print head. Third, during the printing of floor layers, vibrations from the build plate are transmitted through the printed parts to the print head, resulting in vibration coupling between the two components. This coupling effect tends to lower the build plate RMS level while increasing the print head RMS level. When printing the wall structure, the interaction time between the build plate and the print head is reduced due to the frequent layer changing process. This reduced interaction time limits the coupling effects during the printing of wall structures, which

leads to a higher build plate vibration and lower print head vibration compared to printing the floor layers.

Table 3.3: RMS acceleration of the print head and build plate under different printing activities with common carrier vibrations.

RMS acceleration (g)	Print head			Build plate		
	X	Y	Z	X	Y	Z
Idle	0.294	0.313	0.293	0.190	0.222	0.439
Floor	0.531	0.399	0.509	0.122	0.222	0.375
Wall	0.386	0.353	0.418	0.160	0.191	0.577

3.3.3 Aircraft cargo condition

In this section, a 3D printing experiment was conducted under the condition of aircraft cargo vibration, as detailed in **Figure 3.1**. Compared to the common carrier vibration condition, the low-frequency contents are reduced due to the uniform frequency profile of the aircraft cargo vibration. The overall vibration level for both the print head and build plate locations is elevated compared to the no vibration condition. The comparison of the vibration PSD between the print head and build plate in the z-axis during different printing activities is presented in **Figure 3.6**. The PSD spectrum indicates that the print head experiences higher vibration levels compared to the build plate for frequencies above 200 Hz, while the build plate shows higher low-frequency contents around 70 Hz.

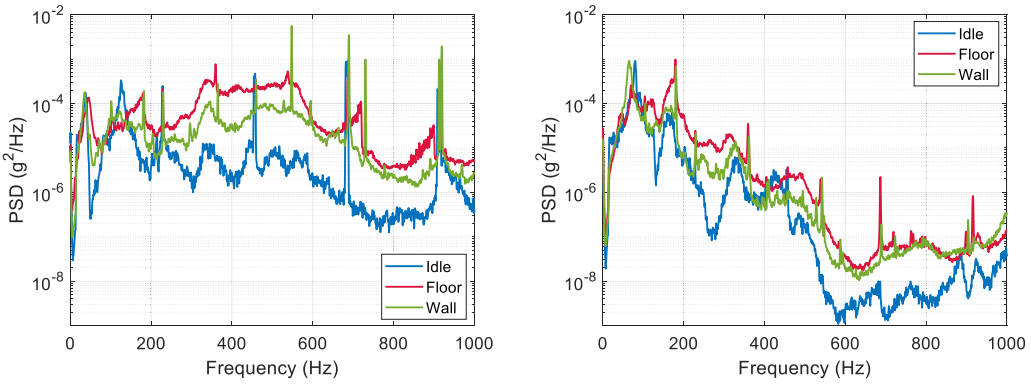

Figure 3.6: (a) PSD of the print head and (b) build plate during different printing activities in z-axis under aircraft cargo vibrations.

The RMS acceleration of the aircraft cargo vibration scenario is summarised in **Table 3.4**. Similar to the no vibration scenario, the vibration levels when printing the floor layers are higher compared to printing the wall structures. This is because a higher amount of motion is involved in printing the floor layers than the wall structures, which generally requires more extensive and continuous movement of the printer components. The reason for the difference between the aircraft cargo and the common carrier vibration scenario is that the displacement of the vibration in this condition is much lower than the common carrier vibration condition, which is low-frequency dominant, largely reducing the interaction time during the printing process.

Table 3.4: RMS acceleration of the print head and build plate under different printing activities with aircraft cargo vibrations.

RMS acceleration (g)	**Print head**			**Build plate**		
	X	**Y**	**Z**	**X**	**Y**	**Z**
Idle	0.196	0.254	0.139	0.059	0.085	0.113
Floor	0.299	0.338	0.303	0.067	0.198	0.152
Wall	0.264	0.314	0.230	0.058	0.131	0.139

3.3.4 Shipboard condition

The last scenario is printing under the shipboard vibration condition, as detailed in **Figure 3.1**. The comparison of vibration PSD between the print head and build plate in z-axis during different printing activities is displayed in **Figure 3.7**. There are multiple narrowband peaks in the spectra corresponding to low-frequency harmonics at 50, 100, 150 and 200 Hz. These frequencies are linked to the RPM of the turbine engine, which is among the most used engines in large cargo ships. **Table 3.5** details the RMS acceleration of the shipboard vibration condition. Notably, the level of vibration is lower when printing the wall layers compared to the floor structures, similar to the aircraft cargo vibration condition.

When comparing the RMS acceleration across all four conditions examined in this study, the following order of magnitude in vibration levels is observed. The common carrier vibration scenario exhibits the highest RMS values, showing the most intense vibrational environment for the 3D printer. The shipboard vibration has the second highest RMS values, followed by the aircraft cargo

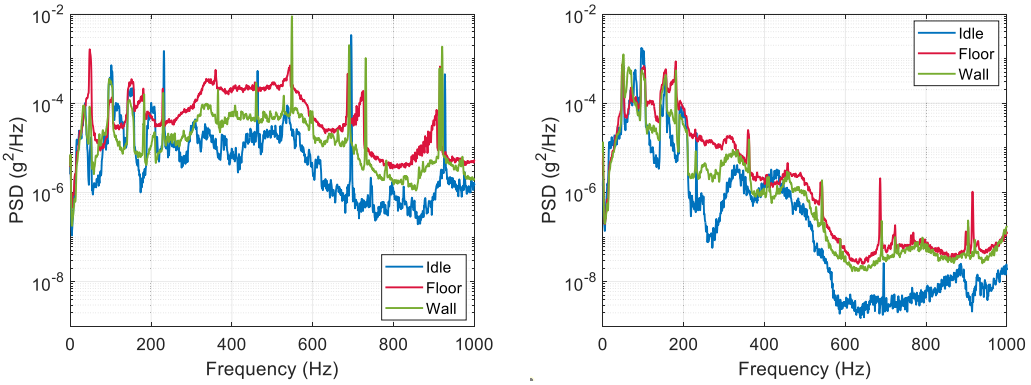

Figure 3.7: (a) PSD of the print head and (b) build plate during different printing activities in z-axis under shipboard vibrations.

Table 3.5: RMS acceleration of the print head and build plate under different printing activities with shipboard vibrations.

RMS acceleration (g)	**Print head**			**Build plate**		
	X	**Y**	**Z**	**X**	**Y**	**Z**
Idle	0.233	0.343	0.170	0.070	0.096	0.168
Floor	0.332	0.332	0.327	0.078	0.207	0.290
Wall	0.258	0.324	0.232	0.061	0.135	0.170

vibration, indicating a relatively milder but notable vibrational impact. The lowest one is printing without vibration, with RMS accelerations at the print head below 0.2 g and at the build plate below 0.01 g in the idle state. The highest level of RMS occurs during printing the floor layers under the common carrier vibration condition.

Although the RMS values of the three vibration conditions are the same, the frequency content of the vibration plays a critical role in its impact on 3D printer structural vibration. The common carrier condition, being low-frequency dominant, results in higher overall acceleration levels. These low-frequency vibrations are particularly disruptive to the 3D printing process as they introduce larger relative movements between the print head and the build plate, compromising layer alignment and surface finish. This can lead to dimensional inaccuracies and surface imperfections. In the next section, the surface roughness of the 3D printed components under four different vibration conditions is examined and discussed.

3.4 Estimating vibration levels of the 3D printer

In addition to direct experimental measurements, this section presents a method for estimating the structural vibration levels of 3D printers using finite impulse response (FIR) filters. Instead of relying on accelerometer measurements for each new vibration condition or printer configuration, this approach utilises a pre-identified FIR filter that represents the dynamic transmission path between the shaker and the printer structure. The FIR filter was modelled using the LMS algorithm, which determines the filter coefficients by minimising the mean squared error between the filter output and the desired signal. A random signal with a constant power spectral density across all frequencies is usually used as the input signal for filter modelling.

The input and output signals used for modelling were similar to the acceleration signals measured at the shaker fixture surface and the build plate, as described in the previous section. Among the three types of transportation vibrations, the vehicle vibration condition was not suitable due to its dominant low-frequency content. The shipboard vibration condition was considered acceptable, although it contains mid-frequency harmonic contents. The aircraft vibration condition was identified as the most suitable for filter modelling, as it mainly includes frequency content with a constant power spectral density across all frequencies. Therefore, input signals corresponding to both the aircraft and shipboard conditions were tested and compared. The filter length was set to 2048 samples.

This method enables the estimation of build plate vibration levels under various excitation profiles. However, it does not apply to the print head location, as there is no clearly identifiable dominant natural frequency at that location, leading to poor modelling accuracy. **Table 3.6** compares the vibration levels under different conditions using FIR filter estimation and direct measurement of the 3D printer in the z-axis when it is in idle condition. The two filter modelling types correspond to the two types of input signals used during the FIR filter identification process. The results show that both filters estimate the vibration RMS levels with less than 5% deviation from the measured values. Moreover, both modelled filters can estimate vibration levels under the vehicle vibration condition, which is dominated by low-frequency content. This

demonstrates the capability of the method to accurately estimate structural vibration levels of the 3D printer under varying excitation profiles.

Table 3.6: Comparison between the vibration RMS levels estimated using the FIR filter and through direct measurement of the 3D printer in the z-axis when it is in idle condition.

Filter modelling	**Common carrier condition**		
	Estimation (g)	**Measurement (g)**	**Difference (%)**
Aircraft	0.460	0.439	4.90
Shipboard	0.451	0.439	2.80
Filter modelling	**Aircraft cargo condition**		
	Estimation (g)	**Measurement (g)**	**Difference (%)**
Aircraft	0.111	0.113	-1.77
Shipboard	0.108	0.113	-4.95
Filter modelling	**Shipboard condition**		
	Estimation (g)	**Measurement (g)**	**Difference (%)**
Aircraft	0.170	0.168	1.13
Shipboard	0.171	0.168	1.97

To further validate the use of the identified FIR filter model method for predicting the vibration levels of different 3D printer structures, a modification was made by adding additional mass to the original 3D printer, as shown in **Figure 3.8**. Two metal blocks, each weighing approximately 117 g, were attached to the 3D printer structure. Although the combined mass of the blocks was only 0.23 kg compared to the printer mass of 1.16 kg, this addition was sufficient to introduce noticeable modifications to the 3D printer's dynamic behaviour. One block was mounted on the side of the base frame, while the other was positioned close to the z-axis motor housing. A comparison of the FRF of the FIR filters before and after the structural modification of the structure is presented in **Figure 3.9a**. Following the addition of mass to the 3D printer, the first peak in the FRF shifts to the left, indicating a reduction in the natural frequency, as expected due to the additional mass. The corresponding impulse responses of the two configurations are shown in **Figure 3.9b**. **Table 3.7** compares the vibration levels under different conditions using FIR filter estimation and direct measurement after modifying the 3D printer structure. Similarly, the results show that both filters estimate the vibration RMS levels with less than 5% deviation from the measured values, which demonstrates the capability of the method to accurately estimate structural vibration levels

of different 3D printer structures.

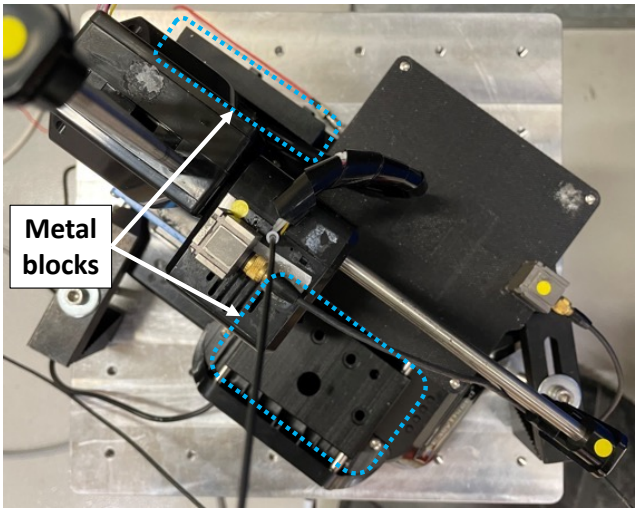

Figure 3.8: The locations of two additional metal blocks on the 3D printer.

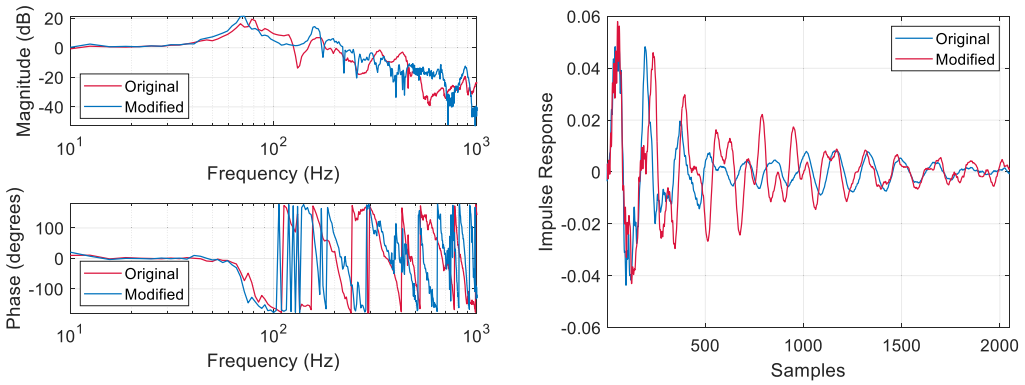

(a) (b)

Figure 3.9: (a) Frequency responses and (b) impulse responses of the original and modified FIR filters of the 3D printer modelled by the aircraft vibration condition.

Once identified, the FIR model can be reused to estimate build plate vibrations under new excitation profiles by convolving the FIR filter with a known input signal, such as the measured acceleration at the shaker surface. This enables rapid and reliable estimation of structural vibration levels without requiring repeated measurements. More importantly, the method offers generalisability across different 3D printer models. By identifying FIR filters for a representative printer geometry, it is possible to predict vibration transmission characteristics under various environmental conditions, including

Table 3.7: Comparison between the vibration RMS levels estimated using the FIR filter and through direct measurement of the modified 3D printer with additional metal blocks.

Filter modelling	**Common carrier condition**		
	Estimation (g)	**Measurement (g)**	**Difference (%)**
Aircraft	0.428	0.445	-3.93
Shipboard	0.435	0.445	-2.27
Filter modelling	**Aircraft cargo condition**		
	Estimation (g)	**Measurement (g)**	**Difference (%)**
Aircraft	0.096	0.097	-1.14
Shipboard	0.100	0.097	3.31
Filter modelling	**Shipboard condition**		
	Estimation (g)	**Measurement (g)**	**Difference (%)**
Aircraft	0.178	0.180	-0.78
Shipboard	0.184	0.180	2.67

land-based, maritime, and aerial scenarios. This FIR filter-based estimation method provides a solution for assessing printer performance in vibration-prone environments and serves as a useful tool for simulation, control design, and risk evaluation before field deployment.

3.5 Surface quality assessment

3.5.1 Surface roughness metric

FFF 3D printer builds objects by stacking layers of melted plastic, resulting in visible lines and a rougher surface compared to machining. During the cooling phase, the plastic may contract slightly, resulting in small gaps or uneven surfaces between layers. Additionally, any relative motion between the nozzle and the build plate can further exacerbate these surface imperfections. Surface roughness is a key aspect of surface finish, which quantifies deviations of a surface from its ideal form in the direction of its normal vector. Larger deviations indicate a rough surface, while smaller deviations signify a smoother surface. The parameter R_a, which is the most commonly used profile roughness parameter, is the arithmetic average value of the filtered roughness profile determined from deviations about the centre line along the evaluation line.

The formula is given by:

$$Ra = \frac{1}{l}\int_0^l |z(x)|\,dx \tag{3.1}$$

where l is the surface length along a surface profile x.

3.5.2 Surface roughness measurement

To ensure the consistency and reliability of the results, five identical copies of samples were printed under similar conditions for each test scenario and their surface roughness was measured. The value will be measured by a surface roughness gauge (Mitutoyo Surftest SJ-210) following the direction as shown in the white arrow in **Figure 3.3**. Four side surfaces of each sample are measured by the surface roughness gauge. The surface roughness of the printed parts under different vibration environments measured by the surface roughness gauge in the horizontal direction is shown in **Figure 3.10**, alongside the build plate RMS accelerations in the z-axis. The surface roughness measurement values shown are the averages of four side surfaces. The results indicate that parts printed without any vibration exhibit the lowest average surface roughness, measuring 1.72 µm. Samples subjected to aircraft cargo vibrations show an increased average surface roughness of 2.84 µm, while those exposed to shipboard vibrations have a roughness of 3.39 µm. The highest surface roughness is observed in samples printed under common carrier vibrations, with an average value of 11.29 µm.

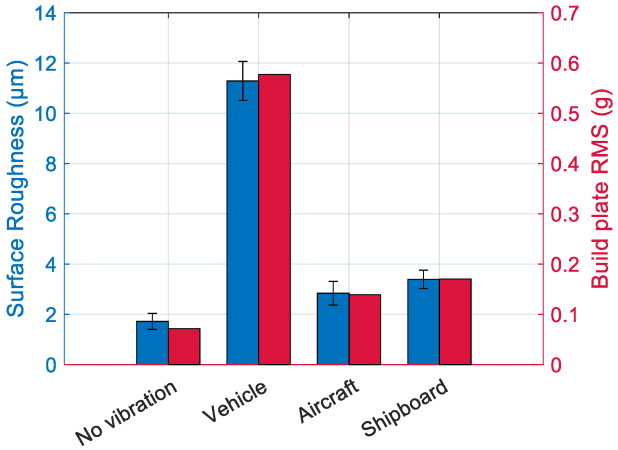

Figure 3.10: A comparison of the surface roughness measurement of printed samples and build plate acceleration RMS under different vibration conditions.

Table 3.8 shows the surface roughness measurements and build plate RMS values under external vibration conditions compared to the no vibration baseline condition. The common carrier vibration causes the largest increase in surface roughness, at 557.31% above baseline, followed by shipboard vibration at 97.44% and aircraft cargo vibration at 65.35%. Build plate acceleration RMS follows a similar trend but with a higher ratio, with common carrier vibration causing the highest increase at 708.40%, followed by shipboard vibration at 138.52% and aircraft cargo vibration at 94.96%. Overall, the build plate acceleration RMS correlates with surface roughness, and the low-frequency content of the vibration has a significant impact on print quality.

Table 3.8: Comparison of surface roughness measurements and build plate RMS acceleration under different vibration conditions relative to the no vibration scenario.

Printing conditions	**Surface roughness measurement** (μm)	**Above no vibration (%)**	**Build plate acceleration RMS (g)**	**Above no vibration (%)**
No vibration	1.72	-	0.07	-
Common carrier	11.29	557.31	0.58	708.40
Aircraft cargo	2.84	65.35	0.14	94.96
Shipboard	3.39	97.44	0.17	138.52

3.5.3 Image-based surface quality metrics

One of the drawbacks of the line-based surface measurement is that it only evaluates the surface profile across a single line, which cannot reveal the entire surface profile of the structure. To quantify the surface roughness of the 3D printed parts more accurately, an enhanced metric is developed. This metric utilises an image of the region of interest (ROI) and calculates the average surface roughness by applying the following equation across all rows of the specified area:

$$Ra_{image} = \frac{1}{N}\sum_{k=1}^{N} Ra_k \tag{3.2}$$

where N is the total number of rows in the image, and Ra_k is the arithmetic average value for the kth row. This metric uses a similar approach to the line-based surface roughness measurement but extends it by using a surface-based average to quantify the roughness of a surface.

Although the surface roughness parameter Ra_{image} can be used to assess the surface quality in the out-of-plane direction, surface imperfections in the in-plane direction of 3D printed parts require further investigation. Ideally, a printed surface consists of multiple parallel lines representing each layer. Under the influence of vibrations, these layers can shift up and down, creating wave or ripple-like patterns. Consequently, to evaluate this waviness, a new metric is introduced based on the analysis of the image ROI from the printed samples. The aim of the waviness metric is to capture the variation in pixel intensity within each row of the image. This variation is an indication of surface texture. The metric is mathematically defined as:

$$W_{row} = f(\Delta I) \tag{3.3}$$

where $\Delta I = Ii + 1 - Ii$ represents the difference in intensity between consecutive pixels in a row, and $f(\Delta I)$ represents a function applied to the absolute differences in intensity for each row. The function used in this study is the mean of (ΔI), while it can be extended to other functions, such as RMS. After computing the waviness score for each row, an overall score for the image is obtained by averaging these scores across all rows. This score represents the average peak variation in pixel intensity across the entire image, which is given by:

$$W_{image} = \frac{1}{N} \sum_{k=1}^{N} W_k \tag{3.4}$$

where N is the total number of rows in the image, and W_k is the waviness score for the kth row. The waviness score of each printed part based on different functions can be compared with the results in the previous section.

3.5.4 Image-based surface quality results

Figure 3.11 displays the original images of four 3D printed samples under different vibration conditions. The photographs were taken using a mobile phone (iPhone 12) rear camera, with a focal length of 4.2 mm, an aperture of f/1.6, an exposure time of 1/50 seconds, and an ISO sensitivity of 200. The

exposure compensation was set to 0, and no flash light was used. The images were captured in a moderately lit office environment and cropped to 600 by 600 pixels for analysis. All four samples have a similar pattern of ringing or ghosting in the highlighted regions. The sample printed under the vehicle vibration condition shows less ringing compared with the other three samples due to its higher surface roughness, which obscures the ringing effect. A consistent corner overshoot is also observed in all specimens, which is caused by imperfect system tuning. In addition, slight warping is visible at the bottom layers of each specimen. This effect is linked to inadequate print bed adhesion rather than the effect of base vibration.

The Ra_{image} values were processed and calculated using MATLAB®. First, the raw images shown in **Figure 3.11** were converted from RGB to grayscale. An ROI of 400 by 400 pixels was then selected from the centre region of each image. Next, a Laplacian filter with an alpha value of 1 was applied to enhance edge features of the image, and the Ra_k values were obtained. Finally, **Equation 3.2** was used to calculate the Ra_{image}. The calculated surface roughness scores following this procedure are presented in **Figure 3.12a**. A higher value indicates a rougher surface. Consistent with the direct measurement results, samples printed without vibration exhibit the lowest average surface roughness, measured at a score of 0.069. However, those subjected to aircraft cargo vibrations show an increased average surface roughness score of 0.080, which is higher than the 0.077 score recorded for samples exposed to shipboard vibrations. The samples printed under common carrier vibrations exhibit the highest average surface roughness at a score of 0.094.

Similarly, the average waviness score, W_k, for each image row was calculated following the same procedure described previously. The overall surface waviness, W_{image}, was then computed for a 400 by 400 pixels ROI using **Equation 3.4**, and the results are shown in **Figure 3.12b**. The samples printed under common carrier vibrations demonstrate the highest waviness score of 0.028, followed by shipboard vibrations, which is 0.017. The samples printed under aircraft cargo vibrations show a surface waviness score of 0.016. The samples printed without vibrations show the lowest waviness score value of 0.011. This metric shows a similar trend with the equivalent surface roughness score results, and an improved accuracy vs. the Ra_{image} metric, indicating its potential in predicting the surface quality of 3D printed parts.

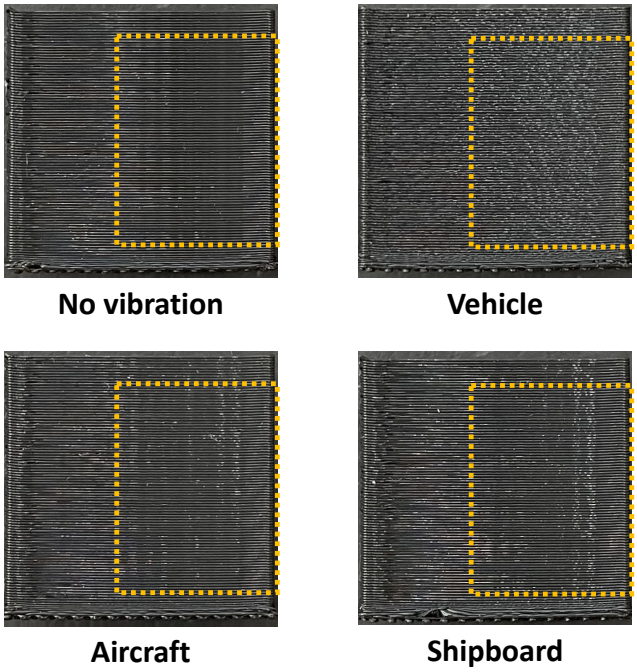

Figure 3.11: Images of one of the side surfaces of 3D printed samples printed under different conditions.

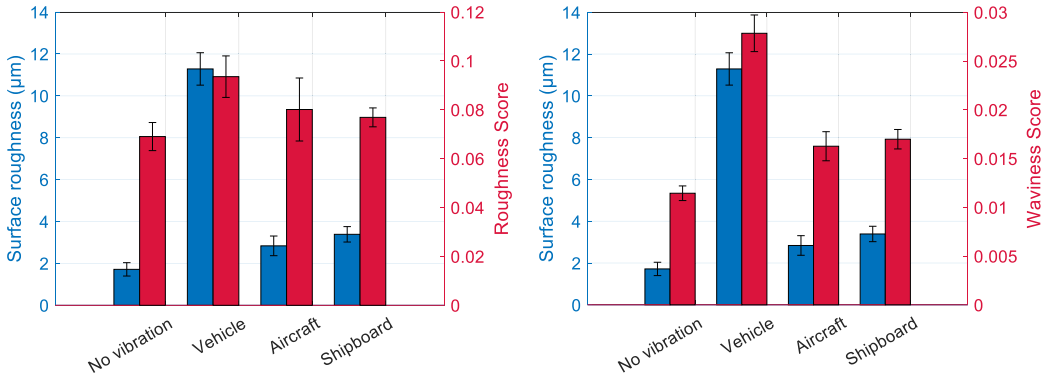

Figure 3.12: (a) Surface roughness score and (b) surface waviness score of samples under different vibration conditions.

In **Table 3.9**, the comparison of different vibration conditions based on two metrics is listed. The common carrier vibration shows the highest roughness and waviness score, indicating its significant influence on the printed parts. The results suggest that different environmental vibrations can significantly impact the surface quality of materials, and low-frequency contents in external vibration have a greater impact on surface quality, as they introduce higher displacement than high-frequency vibrations. Overall, the image-based method can be used as a practical reference technique for rapidly assessing the surface quality of 3D printed parts, particularly in situations where a surface roughness gauge is unavailable.

Table 3.9: Comparison of surface roughness and image-based roughness scores under different vibration conditions relative to the no vibration scenario.

Printing conditions	**Surface roughness measurement** (μm)	**Above no vibration (%)**	**Roughness score**	**Above no vibration (%)**	**Waviness score**	**Above no vibration (%)**
No vibration	1.72	-	0.069	-	0.011	-
Common carrier	11.29	557.31	0.094	35.54	0.028	143.43
Aircraft cargo	2.84	65.35	0.080	16.08	0.016	42.04
Shipboard	3.39	97.44	0.077	11.41	0.017	48.29

3.6 Effects of different vibration conditions on natural frequencies

To further evaluate the impact of the four vibration conditions on the natural frequencies of 3D printed parts, an impact hammer experiment was conducted following a similar setup described in **Section 2.3**. The four conditions used are those described in **Section 3.3**. However, the specimen dimensions in this case are 80 mm × 20 mm × 3 mm, due to the limited print space of the EasyThreed K7 3D printer. A 20% infill density with the line infill pattern was used and maintained throughout the printing of each specimen. The layer

thickness was 0.2 mm, and both the top and bottom have four layers. The clamp length was still 20 mm, using the 3D printed slot structure. A manual impact hammer (B&K Type 8204) was used instead of the automatic impact hammer. Each specimen was impacted five times, and the results are averaged. An example of the coherence of one of the specimens is shown in **Figure 3.13**, demonstrating high repeatability of each impact test. Five identical samples are prepared for each vibration condition to ensure the consistency and reliability of the results.

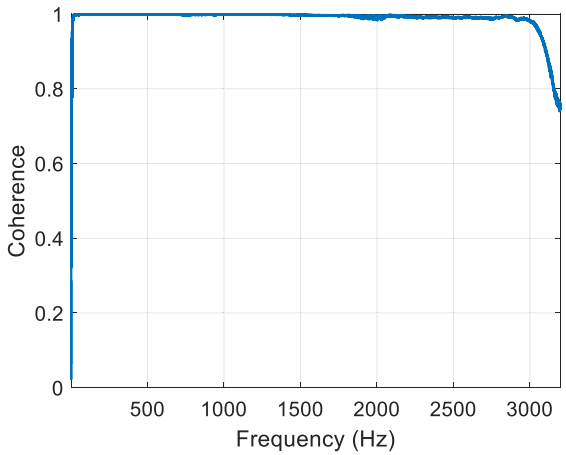

Figure 3.13: An example of a signal coherence function of one 3D printed specimen under an impact test.

The averaged FRFs of four different vibration conditions are compared and presented in **Figure 3.14**, where the shaded areas represent the SDs from five specimens. The parts printed without vibration show the highest first three natural frequencies of 139.5 Hz, 856.7 Hz, and 2302.9 Hz, respectively. The parts printed under common carrier vibration show the second highest natural frequencies, which are followed by the aircraft cargo vibration condition. The parts printed under the shipboard vibration condition demonstrate the lowest first three natural frequencies of 121.8 Hz, 743.2 Hz, and 1990.9 Hz. **Table 3.10** summarises the natural frequencies of 3D printed parts under different vibrations. Generally, the induced vibration reduces the natural frequencies of 3D printed parts due to the reduced effective stiffness in the structure caused by delamination and reduced layer bonding, while it is not simply relevant to the structural vibration level of the 3D printer. The common carrier vibration condition demonstrates the highest RMS acceleration at both

print head and build plate locations, as well as leading to the highest surface roughness. However, it shows the lowest impact on the natural frequencies of printed parts. The shipboard vibration condition with the second largest RMS acceleration and surface roughness demonstrates the highest impact on the natural frequencies of printed parts. These findings indicate that the frequency content of the vibration also has a major impact on the natural frequencies.

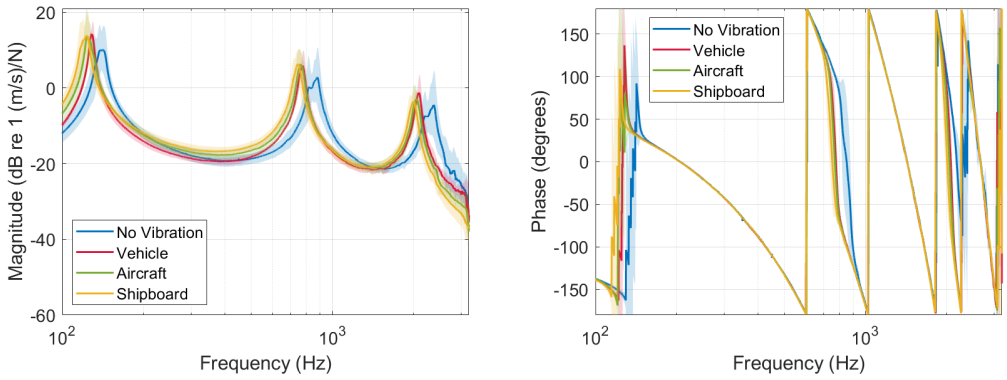

(a) (b)

Figure 3.14: (a) Magnitude and (b) phase responses of specimens printed under different vibration conditions under the impact test. Shaded areas represent standard deviations calculated from all five specimens.

Table 3.10: Natural frequencies of 3D printed parts under different vibration conditions, with SDs shown in the brackets.

Printing conditions	**Natural frequency (Hz)**		
	First	**Second**	**Third**
No vibration	139.5 (4.7)	856.7 (33.0)	2302.9 (92.8)
Common carrier	128.8 (1.4)	772.4 (11.9)	2078.4 (30.0)
Aircraft cargo	126.3 (3.6)	764.9 (15.8)	2048.6 (41.8)
Shipboard	121.8 (3.7)	743.2 (18.2)	1990.9 (44.2)

3.7 Discussions

The investigations presented in this chapter and **Chapter 5** are based on experiments conducted using the EasyThreed K7 FFF 3D printer, instead of the Markforged® X7 3D printer. The selection was made due to practical

constraints in the experimental setup. The low mass and small footprint of the K7 3D printer allow safe mounting on the electrodynamic shaker without additional support structures. The larger enclosed X7 printer could not be mounted without structural modifications. Consequently, the conclusions regarding the effects of vibration on surface roughness and modal properties are directly applicable to this printer model and to other small-scale FFF printers of similar configuration. Nevertheless, the underlying physical mechanisms, such as the amplification of structural vibrations near resonance, increased relative motion degrading surface quality, and internal structural defects reducing effective stiffness, are generalisable principles across different FFF models. While quantitative outcomes (such as specific values of surface roughness or changes in natural frequency) may vary with geometry, mass distribution, rigidity, and motion mechanism of the 3D printer, the qualitative relationships between vibration frequency content, structural response, and print quality are expected to remain consistent among FFF systems.

In this study, the vibration excitation was limited to the vertical direction due to the configuration of the available shaker system. In real-world applications, especially in transportation and mobile printing contexts, equipment is typically exposed to more complex vibration conditions, including significant in-plane and rotational excitations. These additional excitations can induce different modal interactions and increase the complexity of structural responses, potentially affecting the printing process differently from purely vertical excitations. For example, rotational vibrations may introduce additional layer misalignment or structural torsion, while in-plane vibrations might have a greater influence on dimensional accuracy. Given these considerations, the results reported here should be regarded as an initial step toward understanding how complex real-world vibration conditions influence 3D printing quality, and they provide a foundation for future research addressing multi-degree-of-freedom (multi-DoF) vibration scenarios.

3.8 Summary

This chapter presents a comprehensive experimental study of transportation environments, including common carrier, aircraft cargo, and shipboard, and their effects on the surface quality and modal properties of FFF printed parts.

These environmental conditions were simulated using the vertical shaker excitation with identical RMS acceleration levels but distinct frequency contents.

The experimental results indicate that despite all vibration conditions sharing the same time-domain RMS values, their frequency characteristics significantly influence both the surface roughness and natural frequencies of the printed parts. The common carrier vibration, dominated by low-frequency contents, produced the highest surface roughness, 11.29 µm, consistent with higher relative displacement between the print head and the build plate that disrupts layer deposition. Aircraft and shipboard conditions, which are higher-frequency dominant, caused less severe surface degradation but still exceeded the no-vibration baseline. These findings were confirmed by contact measurements and by image-based roughness and waviness metrics, which offer a practical alternative when a surface roughness gauge is unavailable.

The modal properties of the printed parts are further examined through impact hammer testing. It is observed that environmental vibrations reduce the natural frequencies of printed parts, possibly due to delamination, reduced layer bonding, and internal defects. The shipboard vibration condition, with mid-range harmonic content, produced the most significant reduction in natural frequencies, despite moderate changes in surface roughness. This effect is attributed to the induction of internal structural defects, which reduce the effective stiffness of the printed parts and consequently lower their measured natural frequencies. These findings demonstrate the significance of the vibration frequency content in determining the modal properties of FFF parts.

Furthermore, a new predictive method is introduced to estimate the vibration levels of a 3D printer using FIR filters. This method models the dynamic transfer path between the shaker surface and the build plate using pre-identified filters under different excitation conditions. Once identified, the filters can be used to estimate the printer vibration levels without additional physical tests, and can be extended to different printer models. Validation through experiments on a modified printer structure demonstrates that the estimated RMS vibration levels closely match direct measurements, with deviations remaining below 5%.

Future investigations should explore more complex vibration scenarios, including multi-degree-of-freedom excitations such as in-plane (horizontal) and rotational excitations, to comprehensively characterise their influence on

print quality and modal properties. Investigations involving alternative printer architectures, such as delta 3D printers, are also necessary to generalise the findings in this chapter. Additionally, a detailed examination of the internal microstructure of the printed parts using advanced microscopy techniques could reveal how vibration frequency content affects internal characteristics and structural integrity in FFF printing under environmental vibrations.

CHAPTER 4

Active Vibration Control of a moving stage system

4.1 Introduction

4.1.1 Stepper motor system and AVC algorithms

Stepper motors are widely used in industrial applications such as in 3D printers [77], CNC machines [78], and robotic systems [79] due to their precision and efficiency. These motors are often incorporated with lead screws, bearings, and guideways to form precision drive systems. When operating at higher speeds and accelerations, stepper motors can excite the resonant vibration modes of a system when the frequency of the motor coincides with the structural modes of the system, leading to positional inaccuracy [80]. In the context of 3D printing, such vibrations can degrade printed component geometry accuracy or surface finish [25]. It has been reported that the stepper motor operation mostly impacts the printing quality on the build plate [33]. Stepper motors generate multiple harmonic vibrations influenced by their rotational speed, which in turn controls the drive feed rate, further impacting the quality of the end products. Generally, the drive waveforms for full-step, half-step and micro-step configurations consist of square wave signals. These signals approximate sinusoidal waves by modifying the duty cycle of the pulse width modulation signal to closely replicate the ascent and descent of a sinusoidal waveform. This waveform characteristic primarily

causes stepper motors to induce resonances in systems when the waveform frequency approaches the natural frequencies of the system [81]. These forced vibrations caused by the waveform pose challenges to vibration control of systems, particularly when employing traditional passive techniques that target vibration reduction at specific, narrowband frequencies. The performance of these passive methods degrades when system vibration frequencies change due to variations in system operational speeds, or when system resonance frequencies shift due to mass reconfiguration [82, 83]. This variability complicates the task of consistently controlling vibrations across different operational conditions.

Consequently, active control methods have been widely employed for vibration control owing to their capability to dynamically track and adapt to changes within the system. The filtered-x least mean square (FxLMS) method, known for its simplicity and robustness, has been extensively studied over the past decades, becoming the most popular adaptive control algorithm [44]. The secondary path, which is the path between the controller actuator output and error sensor, has a critical influence on the control performance of the system [84]. There are two methods for identifying the secondary path in control systems, which are the online and offline secondary path modelling methods. The online secondary path modelling approach is more suitable due to its ability to adapt dynamically to changes in systems with time-varying characteristics. Conventional online modelling techniques typically rely on broadband auxiliary noise signals to ensure convergence, but this additional excitation may degrade control performance by introducing residual noise, especially in low signal-to-noise ratio or nonstationary conditions. Alternatively, online secondary path modelling without auxiliary noise signal approaches, such as those based on control signal excitation [85], theoretically overcomes this limitation. Nevertheless, they require the control signal to provide sufficient excitation of the secondary path. By contrast, for systems with slow-changing dynamics, the offline secondary path modelling method can still provide effective control performance while not requiring high computational complexity.

Alongside the FxLMS algorithm, its variants such as the normalised least mean square (NLMS) [86] and affine projection least mean square (APLMS) [87], have been developed to improve convergence rates and reduce steady-state errors. Specifically, the APLMS algorithm has found successful applica-

tions in various fields, including fault diagnosis in rotating machinery [88], active noise control [89, 90], and acoustic feedback cancellation [91]. Despite the broad applications of the APLMS algorithm in other domains, its use in AVC, particularly in systems experiencing periodic disturbances from rotating machinery, is not fully explored, indicating potential areas for further research [92].

4.1.2 AVC in complex and time-varying dynamic systems

Piezoelectric actuators are widely utilised in AVC due to their ability to generate relatively large mechanical forces at high operating frequencies, all within a compact, lightweight configuration, such as the piezoelectric stack actuator (PSA) [93]. This type of actuator is based on the inverse piezoelectric effect, where materials deform mechanically when subjected to an electric field [94]. This capability makes them particularly effective for controlling vibrations in complex systems. For controlling vibration in complex rotating systems, several studies have investigated the AVC of gear shaft vibration [95, 96], and machinery vibration [97, 98]. However, a major limitation of the AVC in complex systems is its reliance on precise reference signals, typically derived from built-in sensors such as encoders [99, 100]. In the absence of such signals, AVC systems rely on synthetic reference signals [101]. The quality of these reference signals significantly impacts the overall performance of AVC systems. This dependency imposes a common limitation of the feedforward adaptive AVC system, where the availability of a reference signal that closely correlates with the targeted vibration is crucial for effective vibration control. Therefore, when the reference signal is unavailable, a feedback adaptive system can be a viable alternative, which has already been used for AVC and ANC [102, 103, 104, 105]. However, feedback systems have their own limitations, including a narrow bandwidth of attenuation, potential system instability, and the waterbed effect, which amplifies noise outside of the desired operational frequency band [103]. Moreover, hybrid AVC systems combining feedforward and feedback structures have been explored to address the limitations inherent in both types of systems [106, 107]. One such system effectively controlled vehicle road noise using a sub-band FxLMS algorithm, which reduces the computational complexity associated with the traditional FxLMS. This was complemented by a feedback mechanism that helped to reduce residual noise

[108]. Another study introduced a hybrid feedback PID (Proportional Integral Derivative)-FxLMS algorithm, which improved convergence, stability, and ease of parameter tuning in controlling harmonic vibrations in a piezoelectric cantilever beam [47].

Research has primarily focused on the AVC of systems with dynamics that remain constant over time. However, applications of AVC to systems with time-varying dynamic characteristics remain underexplored in existing literature. For example, the linear interpolation method has been proposed to model time-varying secondary paths [98]. The researchers achieved AVC for rotating machinery by measuring secondary paths at multiple points during a single revolution and linearly interpolating secondary path models between these points. This approach utilises pre-identified offline secondary paths at different angular positions to model time-varying secondary paths and effectively control structure-borne vibration in rotating machinery. The findings indicate that control performance stabilises and remains consistent when the number of interpolations exceeds four. Furthermore, the vibration caused by the motor during system operation has yet to be effectively controlled [109]. In the context of 3D printing, stepper motors drive not only stationary components such as the extruder of the printer head, but also the positioning of the printer head and the build plate itself during the printing process. This configuration results in a moving vibration source, which introduces a time-varying secondary path and dynamic system characteristics that change rapidly and continuously. This mobility further complicates the vibration control of such systems, emphasising the need for alternative AVC strategies to accommodate these dynamic environments.

This chapter explores AVC in a stepper motor-driven linear positioning system, where the dynamic characteristics of the moving stage vary along the linear guide. Initially, sensor locations for the AVC system are strategically selected based on the coherence function between the reference and error signals. The study begins with simulation analyses of the moving stage system, where the actuator is placed on the moving stage, which does not lead to time-varying secondary paths. Both feedforward and feedback-based LMS and APLMS algorithms are formulated, and their performance, evaluated in terms of harmonic suppression and overall vibration reduction, is compared while considering computational complexity. Subsequently, the actuator is

moved to a location close to the vibration source, which leads to a time-varying secondary path system. The secondary path models (SPM) at five distinct locations along the linear guide are collected and modelled offline. The study then presents experimental investigations, beginning with the implementation of the FxLMS algorithm using each of the five single SPMs. This is followed by the introduction of the proposed online switching SPM method applied to the moving stage system setup. Finally, a comparative analysis of the vibration control performance and system stability between using a single SPM and the online switching of SPMs method is presented.

4.2 AVC system and control algorithms

4.2.1 Moving stage linear positioning system setup

The moving stage system examined in this study is widely utilised in projects such as RepRap (replicating rapid prototyper) 3D printers and CNC machines. The linear guide was assembled from two V-slot aluminium extrusions, each with dimensions of $1000 \times 20 \times 40$ mm. The moving plate was made of aluminium alloy with dimensions of $100 \times 88 \times 3$ mm. The stepper motor, controlled by an Arduino Uno microcontroller, rotates a threaded lead screw to move the plate along the linear guide. The motor speed was set to 30 RPM with no microstepping.

The primary vibration source in the moving stage system originates from the stepper motor that drives the lead screw. To monitor these vibrations, two IEPE accelerometers were employed, with one (B&K Type 4397) placed near the stepper motor as the reference sensor and the other (B&K Type 4533-B) mounted on the moving plate as the error sensor. Both sensor signals were conditioned and captured on an NI-9234 C series input module, which digitises the inputs for subsequent processing by the control system. To actively attenuate the plate vibration, a cylindrical-shaped preloaded linear piezoelectric stack actuator (PSA) model PSt VS12, with 12 mm in diameter and 28 mm in length, was mounted on the moving plate through a customised bracket.

Actuator placement is a critical factor that directly influences control effectiveness and system stability. Optimal placement strategies aim to position actuators at locations with high modal strain energy, ensuring effective ex-

citation of dominant vibration modes. In this section, the actuator was first placed near the error sensor for several reasons. First, this placement allows an effective actuator output as it leads to a higher secondary output with a lower transmission distance. Second, this configuration does not lead to a time-varying secondary path. In the context of AVC for plate structures, where displacement is primarily due to bending vibrations, a customised mounting structure was designed and manufactured by structural steel. This structure transforms the axial forces from the PSA into actuating bending moments, effectively cancelling the primary mode of vibration of the plate. This PSA was driven by a PiezoDrive PD200X4 four-channel power amplifier, which provides a high voltage output with a gain of 20. This system operated at a sampling frequency of 6.4 kHz and utilises NI LabVIEW software for data acquisition, signal processing and control execution.

This study examines two distinct system configurations: the static and the moving system. In the static system setup, the lead screw is disconnected from the nut block at the back of the plate bracket, ensuring that the plate remains stationary during stepper motor operation. Conversely, in the moving system setup, the lead screw was connected to the plate bracket, allowing the plate to move along the linear guide as the stepper motor drives the lead screw rotation. In both configurations, the plate was initially positioned at the midpoint of the guide, 500 mm from each end, ensuring a consistent starting point for all experiments. The overview of the moving stage linear positioning system is shown in **Figure 4.1**.

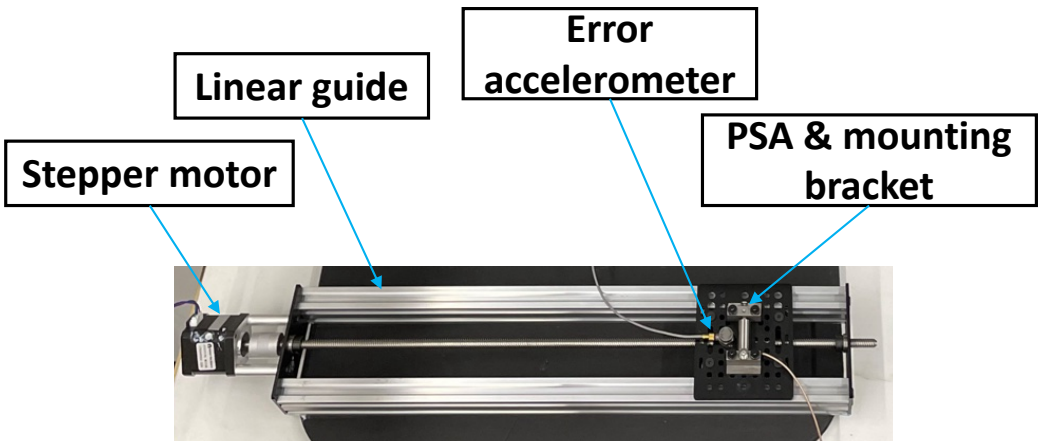

Figure 4.1: An overview of the moving stage linear positioning system.

4.2.2 Two system configurations

This study examines two distinct system configurations under a similar experimental setup: the static and the moving system. In the static system setup, the lead screw was disconnected from the nut block at the back of the plate bracket, ensuring that the plate remains stationary during stepper motor operation. This configuration leads to a stationary stage and a constant primary path model. Conversely, in the moving system setup, the lead screw was connected to the plate bracket, allowing the plate to move along the linear guide as the stepper motor drives the lead screw rotation. This leads to a time-varying primary path of the system. In both configurations, the plate was initially positioned at the midpoint of the guide, 500 mm from each end, to ensure a consistent starting point for all experiments.

Both feedforward and feedback control strategies are explored to reduce plate vibration of the above two systems, as illustrated by different configurations demonstrated in **Figure 4.2**. The feedforward system requires an additional reference sensor, and it is well recognised that the coherence between the reference and error signals determines the maximum achievable vibration reduction [110]. Therefore, two alternative reference sensor locations are explored to evaluate the coherence function, as depicted in **Figure 4.2a** and **4.2b**, respectively. The coherence of two signals c_{re} can be calculated based on the equation below [111]:

$$c_{re} = \frac{|\Phi_{re}|^2}{\Phi_{rr}\Phi_{ee}} \tag{4.1}$$

where Φ_{re} is the cross-power spectral density of the reference and error signals, Φ_{rr} and Φ_{ee} are the PSDs of the reference and error signals, respectively. The first location was on the top surface of the stepper motor, while the second was at the edge of the linear guide, as detailed in **Figure 4.3b** and **4.3c**, respectively. To actively reduce the vibration of the plate, a PSA was installed on the plate to generate a control signal that counteracts the vibration induced by the stepper motor. An error sensor was mounted next to the PSA on the plate to monitor the residual vibrations, as shown in **Figure 4.3a**.

Figure 4.4a presents the estimated Welch's PSD of the vibration signal measured on the plate for the static system. The PSD is estimated by dividing the measured signal into segments of 6400 samples, with a 50% overlap between segments, and the number of FFT points is 25600. It can be observed

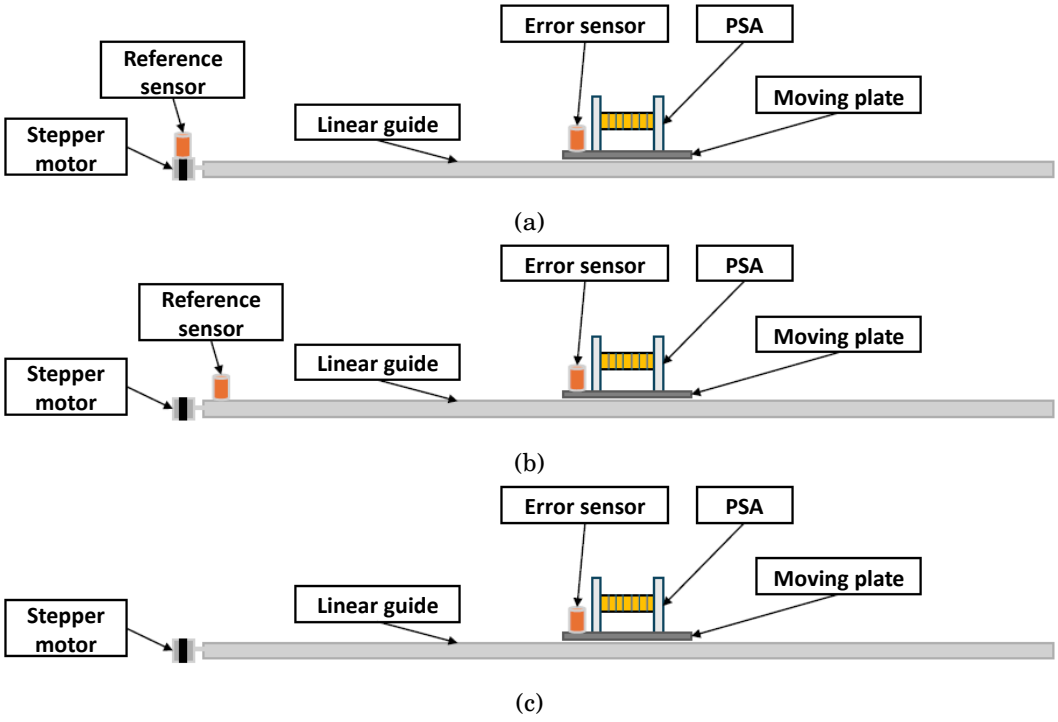

Figure 4.2: Schematics of the three configurations (a) feedforward system with reference sensor on motor surface, (b) feedforward system with reference sensor on the edge of the linear guide, and (c) feedback system with no reference sensor.

that the vibration signal spectrum consists of multiple harmonics of the fundamental frequency, set at 100 Hz. The fundamental frequency is directly related to the step frequency of 100 Hz, which is the rate at which the digital pulses are applied. These harmonics are caused by various factors. First, the operation of the stepper motor, which involves taking discrete steps driven by electrical pulses, results in sudden changes in motion and produces a broad range of frequency contents. Second, the nature of the square wave of the electric pulse signal to drive the stepper motor, with its sharp on and off transitions, inherently contains the fundamental frequency and its harmonics. Additionally, the physical structure of the motor may resonate at certain frequencies, thus amplifying these harmonics and leading to mechanical resonances within the system.

Figure 4.4b compares the coherence between the two reference signals and the error signal. The results show that positioning the reference sensor at the edge of the linear guide enhances signal coherence for frequencies above

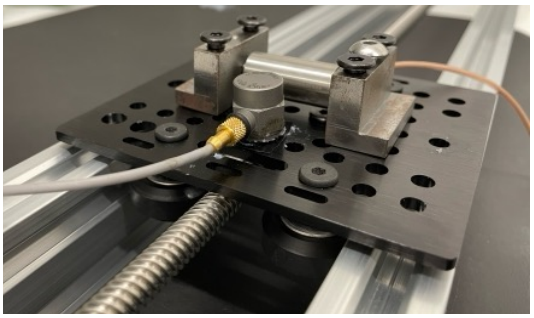

(a)

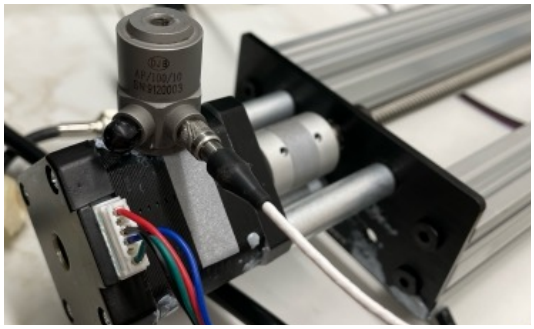

(b)

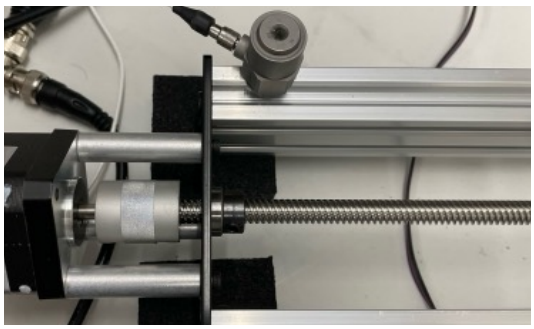

(c)

Figure 4.3: (a) The actuator and the error sensor on the moving plate. Reference sensor at the (b) motor surface and (c) linear guide edge, respectively.

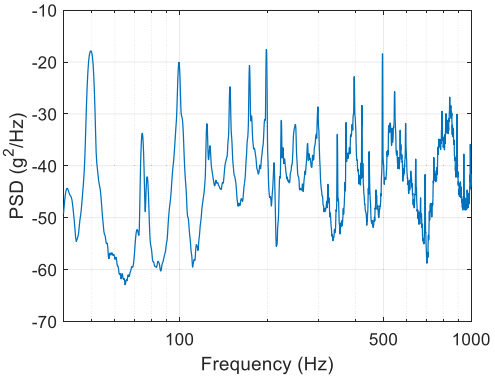

(a)

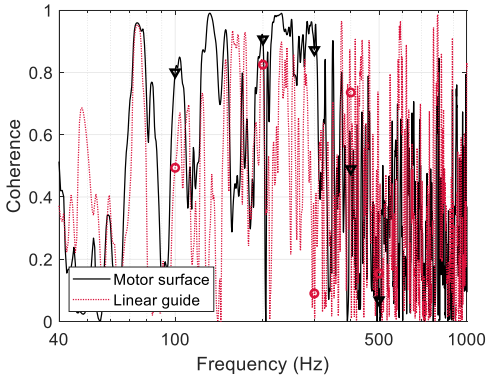

(b)

Figure 4.4: (a) Vibration signal PSD measured from the moving plate before control for the static system. (b) Signal coherence comparison of the reference signal and error signal for each of the two reference sensor locations.

300 Hz. In contrast, the motor surface position demonstrates high coherence for frequencies below 300 Hz. The coherence of the first five resonances of the static system is denoted by the black triangles and red circles in the figure for the two reference sensor locations, respectively. These variations in signal coherence are due to the different structural dynamics at each sensor location. Based on these observations, the reference sensor for the static system is placed on the motor surface, while for the moving system, it is positioned at the edge of the linear guide. This selection of the reference sensor location is critical for adapting the system to effectively manage the specific vibrational characteristics of each setup, ensuring optimal control performance. It is noted that both reference sensor locations display limited signal coherence at the peak frequencies of the PSD in **Figure 4.4a**, especially at frequencies below 100 Hz. This lack of coherence compromises the effectiveness of the feedforward control system, as will be demonstrated in the following section.

In all scenarios investigated in this study, the error accelerometer remains fixed despite the movement of the stage, allowing the secondary path filter to be considered as stationary. The secondary path response was experimentally modelled using a broadband random noise signal up to 6.4 kHz input for a duration of 10 seconds, with the response measured by the error sensor. The secondary path was modelled as an FIR filter with a length of 1024. However, to improve the clarity in the initial response, the impulse responses of these secondary path filters are presented truncated, showing only the first 256 samples. This truncation indicates that shorter filter lengths might be feasible without detrimentally influencing system performance. The impulse responses and frequency responses of these filters are illustrated in **Figure 4.5**. For the impulse responses, the static system shows higher amplitudes in the initial samples, while the moving system responses become more pronounced in later samples. In terms of frequency responses, the static system exhibits multiple peaks around 550 Hz and 850 Hz, whereas the moving system shows a notable peak at around 750 Hz. Below 500 Hz, both systems display similar response magnitudes. Overall, both systems exhibit significantly higher responses in the high-frequency range (above 1 kHz) compared to the low-frequency range (below 1 kHz), with differences exceeding approximately 30 dB, as illustrated in **Figure 4.5b**. These observations indicate the distinct dynamic characteristics of the static and moving systems.

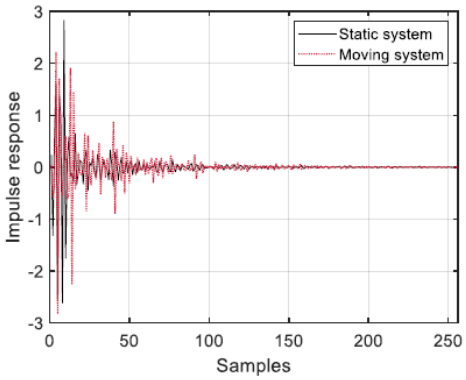

(a)

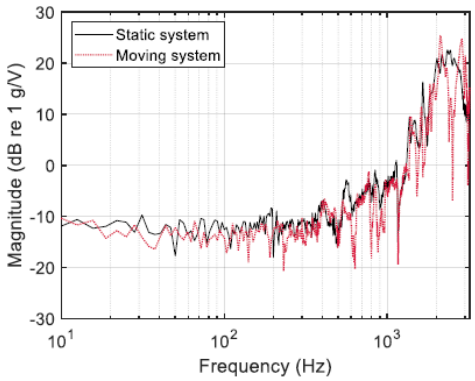

(b)

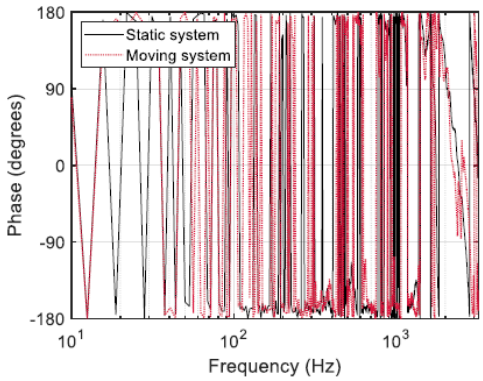

(c)

Figure 4.5: Comparison of the responses of the moving and static system; (a) impulse response, (b) magnitude- and (c) phase-frequency responses.

4.2.3 Feedforward control with FxLMS algorithm

In the FxLMS algorithm, the reference signal is first filtered through a model of the secondary path before it is used in the LMS update algorithm. This step allows for correct alignment of the phase and magnitude of the reference signal, enhancing the algorithm stability for systems with complex secondary paths [86]. In the AVC system, the residual vibration signal $e(n)$ at the time instant n is the superposition of primary vibration $d(n)$ induced by the stepper motor and the secondary path control signal $y(n)$ applied by the PSA, given by:

$$e(n) = d(n) + y(n) \tag{4.2}$$

Then, the output from the secondary path $y(n)$ is:

$$y(n) = \sum_{i=0}^{L-1} x_s(n-i)w_i(n) = \mathbf{w}^T(n)\mathbf{x_s}(n) \tag{4.3}$$

where $w_i(n)$ is the ith component of the controller weight vector $\mathbf{w}(n) = [w_0(n),...,w_{L-1}(n)]^T$ of length L, $x_s(n) = \sum_{i=0}^{L_s-1} x(n-i)s_i(n)$ is the element of the filtered reference signal $\mathbf{x}_s(n)$, and $s_i(n)$ is the ith component of the secondary path vector of length L_s. It is noted that the slow adaptation assumption has been used to derive the above equation. The filtered signal $\mathbf{x}_s(n)$ is obtained by passing the reference signal through the estimated secondary path $\hat{S}(z)$. Then, the reference signal filtered by the estimated secondary path $\mathbf{x}_{\hat{s}}(n)$ can be calculated by:

$$\mathbf{x}_{\hat{s}}(n) = \hat{s}(n) * \mathbf{x}(n) \tag{4.4}$$

where $\mathbf{x}(n)$ is the reference signal vector measured at the reference accelerometer, and $\hat{s}(n)$ is the inverse z-transform of the modelled secondary path filter $\hat{S}(z)$. Hence, the controller weight can be updated by minimising the mean squared error signal $E\left[e^2(n)\right]$ as follows:

$$\mathbf{w}(n+1) = \mathbf{w}(n) - \mu e(n)\mathbf{x}_{\hat{s}}(n) \tag{4.5}$$

where μ is the step size. The controller aims to reduce the unwanted vibration by minimising the squared error acceleration $e(n)$ measured at the error accelerometer. The block diagram representation of the feedforward system is presented in **Figure 4.6a**.

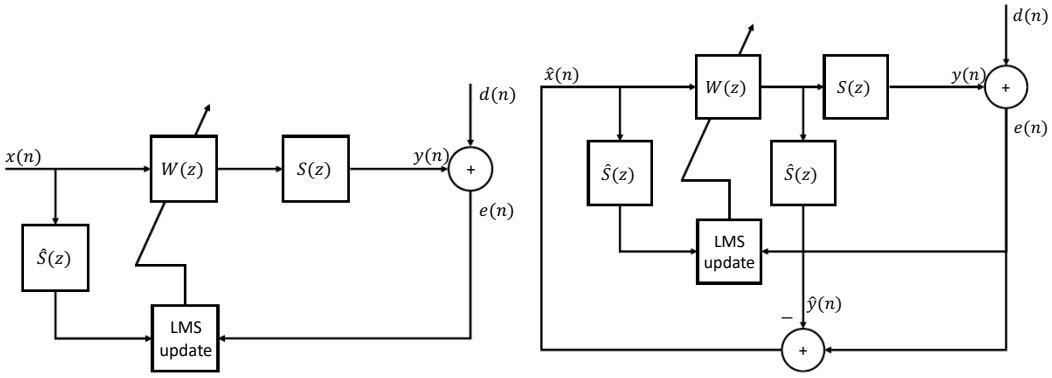

Figure 4.6: Block diagrams of the (a) feedforward and (b) feedback AVC system.

4.2.4 Feedback control with FxLMS algorithm

The primary distinction between the feedforward FxLMS and the feedback LMS (FbLMS) is that in FbLMS algorithm, there is no reference sensor to

collect the reference signal. Instead, the reference signal is synthesised using the error signal and the controller output filtered by the estimation of the secondary path. The synthesised reference signal $\hat{\mathbf{x}}(n)$, combined with the vibration residue e(n), is used to update the controller weight, allowing the algorithm to adjust based on real-time system dynamics. The reference signal is calculated as follows:

$$\hat{\mathbf{x}}(n) = e(n) - \hat{y}(n) \tag{4.6}$$

the estimated output from the secondary path $\hat{y}(n)$ is:

$$\hat{y}(n) = \mathbf{w}^T(n)\hat{\mathbf{x}}_{\hat{s}}(n) \tag{4.7}$$

where $\hat{\mathbf{x}}_{\hat{s}}(n)$ is the filtered synthesised reference signal $\hat{\mathbf{x}}(n)$ through the estimated secondary path filter $\hat{S}(z)$. Substituting **Equation 4.7** into **Equation 4.6** yields the equation of $e(n)$. Then, the controller weight can be updated following **Equation 4.5** by replacing $\mathbf{x}_{\hat{s}}(n)$ with $\hat{\mathbf{x}}_{\hat{s}}(n)$. The schematic of the feedback AVC system is shown in **Figure 4.6b**.

4.2.5 Proposed FbAPLMS algorithm

To enhance the adaptation speed and performance of traditional feedforward and feedback LMS algorithms, researchers have extensively investigated more advanced algorithms such as the affine projection algorithm for active control systems [89, 90]. This algorithm enhances the convergence rate by simultaneously processing M input vectors and updating the filter coefficients through projection onto an affine subspace spanned by these vectors [86]. This method significantly speeds up the convergence rate compared to conventional LMS techniques, providing a robust framework for integrating advanced processing capabilities into active vibration control systems.

Given the set of input vectors $x(n),\ x(n-1),\ \cdots,\ x(n-k)$, desired output $d(n),\ d(n-1),\ \cdots,\ d(n-k)$, where $k = 0,\ 1,\ \cdots,\ M-1$, the filter weights vector $\mathbf{w}(n+1)$ is updated to minimise the squared Euclidean norm of the difference $\eta(n) = \mathbf{w}(n+1) - \mathbf{w}(n)$ [86]. This update is subject to the constraints that the output matches the desired signal at M previous instances as follows:

$$\mathbf{w}^T(n+1)x(n-k) = d(n-k), k = 0,\ 1,\ \cdots,\ M-1 \tag{4.8}$$

Then, the constraints can be assembled into a matrix form where $\mathbf{X}(n)$ is an $N \times M$ matrix:

$$\mathbf{X}^T(n)\mathbf{w}(n+1) = d(n) \tag{4.9}$$

Next, constructing the Lagrangian $\mathscr{L}$, by adding each element λ_k from the column vector of Lagrange multipliers λ, to the objective function for each constraint [86]. This leads to the following expression:

$$\mathscr{L} = \|\eta(n)\|^2 + \sum_{k=0}^{M-1} \lambda_k \left(\mathbf{w}^T(n+1)\mathbf{x}(n-k) - d(n-k)\right) \tag{4.10}$$

Differentiating $\mathscr{L}$ with respect to $w(n+1)$ and setting to zero:

$$\frac{\partial \mathscr{L}}{\partial w(n+1)} = 2(\mathbf{w}(n+1) - \mathbf{w}(n)) + \sum_{k=0}^{M-1} \lambda_k x(n-k) \tag{4.11}$$

Rearranging this equation to obtain:

$$\mathbf{w}(n+1) = \mathbf{w}(n) - \frac{1}{2}\sum_{k=0}^{M-1} \lambda_k x(n-k) \tag{4.12}$$

$$\mathbf{w}(n+1) = \mathbf{w}(n) - \frac{1}{2}\mathbf{X}(n)\lambda \tag{4.13}$$

Next, substituting **Equation 4.13** back to **Equation 4.9** to establish the constraint in matrix form, allows the error term $e(n)$ to be defined as:

$$e(n) \;=\; d(n) - \mathbf{X}^T(n)\mathbf{w}(n) \tag{4.14}$$

Rearranging and solve for λ:

$$\lambda = -2(\mathbf{X}^T(n)\mathbf{X}(n))^{-1} e(n) \tag{4.15}$$

Finally, substituting λ back to **Equation 4.13** to find the updated filter weight $\mathbf{w}(n+1)$:

$$\mathbf{w}(n+1) \;=\; \mathbf{w}(n) + \mathbf{X}(n)(\mathbf{X}^T(n)\mathbf{X}(n))^{-1} e(n) \tag{4.16}$$

In practice, **Equation 4.16** is often replaced with the following:

$$\mathbf{w}(n+1) \;=\; \mathbf{w}(n) + \mu\mathbf{X}(n)(\mathbf{X}^T(n)\mathbf{X}(n) + \psi\mathbf{I})^{-1} e(n) \tag{4.17}$$

where μ is the step size, $\mathbf{I}$ is an M-sized identity matrix, and ψ is a small positive constant. The reason for the introduction of the constant ψ is to prevent the inversion of the small value when the squared Euclidean norm $\mathbf{X}^T(n)\mathbf{X}(n)$ is small [86], which could lead to instability of the algorithm.

4.2.6 Computational complexity analysis

This study utilised a single-channel AVC system with one reference sensor, one error sensor, and one actuator. The length of the FIR control filter in the AVC system L, was 2048 samples, while the length of the FIR filter in the secondary path model L_s, was 1024 samples. Based on these specifications, the computational complexity of both feedforward and feedback algorithms was analysed and presented in **Table 4.1**. The computational complexity increases significantly with the use of the APLMS algorithm, particularly as the projection order M is increased. At a projection order of 4, the total number of multiplication operations performed during the iterative process is listed. It is important to note that when the affine projection order M is reduced to 1, the APLMS becomes the NLMS algorithm. As can be observed, the computational complexity of the APLMS is substantially higher when compared with that of the corresponding standard LMS algorithm. This can be attributed to the weight update step in the APLMS algorithm, where the computation of the matrix product requires $2*M^2*n_{con}$ additional multiplications, greatly increasing the overall computational burden. When comparing these algorithms in both feedforward and feedback configurations, incorporating the step of estimating the reference signal in the feedback configuration increases the computational complexity. This rise in complexity leads to longer computation times and places a greater burden on the processor. This shows the trade-off between improving algorithm performance and increasing computational cost. **Figure 4.7** illustrates the total number of multiplications per iteration for the APLMS-based algorithms, with a projection order ranging from 1 to 10. It also includes data for two standard feedforward and feedback algorithms.

Table 4.1: Summary of the computational complexity.

Algorithms	**Number of multiplications**	**Total number of multiplications** ($M=4$)
FxLMS	$2*n_{con}+n+1$	5.12×10^3
FxAPLMS	$2*M^2*n_{con}+2*M*n_{con}+n_{con}+n$	8.50×10^4
FbLMS	$2*n_{con}+2*n+1$	6.15×10^3
FbAPLMS	$2*M^2*n_{con}+2*M*n_{con}+n_{con}+n+2*M*n$	9.32×10^4

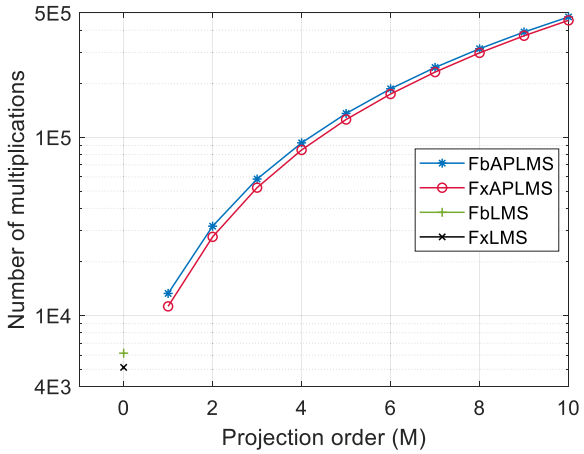

Figure 4.7: Number of multiplications per iteration of different algorithms in this study.

4.3 The AVC simulation analysis

4.3.1 AVC of the static system

Initially, the reference sensor was placed at the motor surface of the static system for the feedforward algorithms. This location was selected due to the predominance of low-frequency contents, including 50 Hz, 100 Hz and their harmonics up to 500 Hz, in the error signal. At this location, the reference sensor signal demonstrated improved coherence over these low-frequency contents, demonstrating its effectiveness in capturing the relevant vibrations. The PSD estimates of the static system, both before and after control using feedforward and feedback algorithms, are presented in **Figure 4.8**. The effects of different control algorithms on PSD difference are illustrated in **Figure 4.9**, where the projection order M was set at 4 to emphasise the differences in AVC performance between the LMS and APLMS algorithms. Notably, subharmonic frequencies, such as 75 Hz, 125 Hz, and 150 Hz, are observed between the primary harmonics but at significantly lower amplitudes. This occurrence is likely attributed to the square wave signals that drive the motor, inherently containing multiple harmonic components, which leads to the complex dynamics of the system.

When comparing feedforward and feedback algorithms, feedback algorithms are observed to offer enhanced performance, particularly at multiple resonances. Among the feedforward algorithms tested, the FxAPLMS algo-

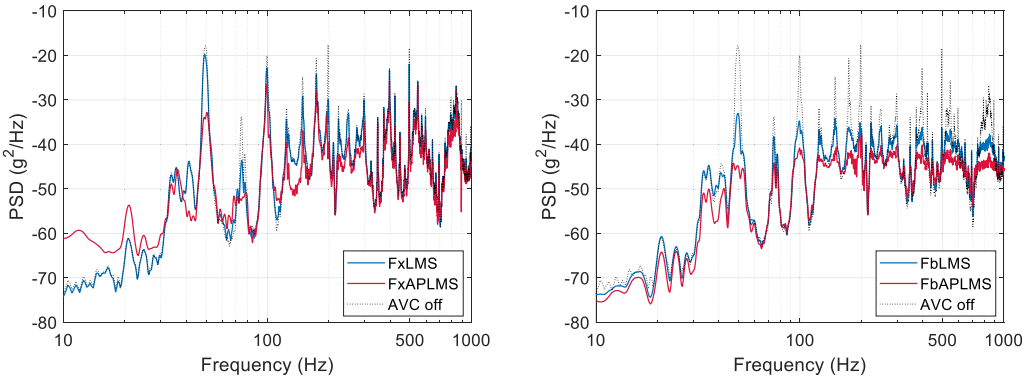

(a) (b)

Figure 4.8: PSD before and after control in the static system using: (a) feedforward, and (b) feedback algorithms. Projection order M is 4.

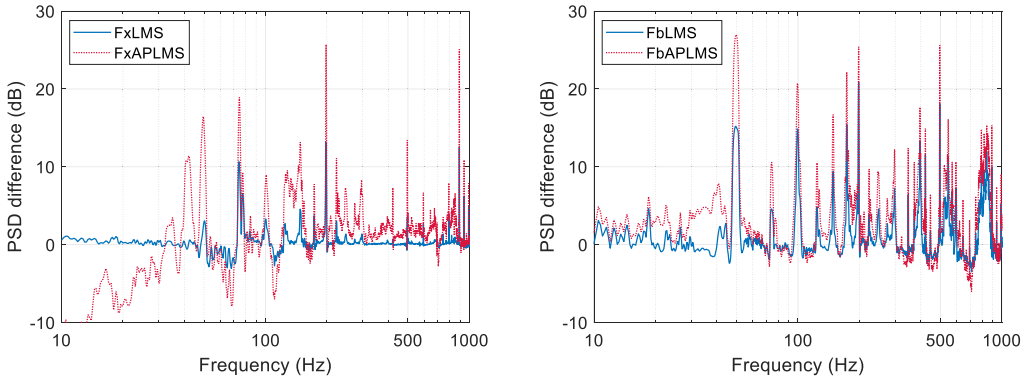

(a) (b)

Figure 4.9: PSD difference after control in the static system using: (a) feedforward, and (b) feedback algorithms. Projection order M is 4.

rithm demonstrates higher vibration reduction across multiple harmonics compared to FxLMS. However, it introduces low-frequency noise below 40 Hz due to poor correlation between the error signal and reference signal in these frequency ranges, as illustrated in **Figure 4.4a**. This issue leads to degraded performance of the FxAPLMS algorithm. In contrast, the feedback algorithms explored, particularly the FbAPLMS, achieve substantial vibration reduction across the entire spectrum, effectively removing the low-frequency noise observed in FxAPLMS. Nonetheless, both feedback algorithms still amplify high-frequency noise around 700 Hz. This amplification of unwanted noise at some frequencies is a common drawback of these algorithms [55].

Table 4.2 summarises the vibration reduction achieved at the first five

harmonics for each algorithm, f is 100 Hz. Notably, the FbLMS algorithm achieves 5 dB reduction across the spectrum, while utilising nearly 15 times less computational effort than FbAPLMS. Overall, the FbLMS is the most computationally cost-effective algorithm, offering the highest ratio of overall reduction to the total number of multiplications among all algorithms in the static system. Additionally, FbLMS exhibits a 3.5 dB improvement in overall reduction compared to FxLMS and achieves a 0.6 dB greater reduction than FxAPLMS with approximately 13 times less computational effort. At a projection of 4, FbAPLMS provides 2.2 dB more reduction than FxAPLMS while requiring an additional 8200 multiplications. This enhanced performance of the feedback algorithms indicates their suitability for such static systems where the reference signal at the motor surface poorly correlates with the error signal at the dominant frequencies. This makes the feedback approach more advantageous for effective vibration control in such setups.

Table 4.2: Summary of the vibration reduction (dB) of the static system.

Algorithms	**Reduction at** f	**Reduction at** $2f$	**Reduction at** $3f$	**Reduction at** $4f$	**Reduction at** $5f$	**Overall reduction**
FxLMS	2.14	12.39	1.37	0.48	3.55	1.48
FxAPLMS ($M = 4$)	5.46	25.01	6.36	2.95	12.98	4.44
FbLMS	13.79	20.88	7.26	13.35	18.08	5.01
FbAPLMS ($M = 4$)	20.08	25.42	12.21	17.57	25.60	6.60

To further investigate the impact of the projection order on the AVC performance of FbAPLMS algorithm, a comparison is presented in **Figure 4.10**. As the projection order increases, there is a noticeable decrease in frequency attenuation below 50 Hz. Nonetheless, the overall vibration reduction is significantly improved. This improvement is particularly notable at the first, second and fifth harmonics, which are among the most significant peaks in the error signal. The detailed AVC performance for different projection orders of FbAPLMS is shown in **Table 4.3**. Although FbAPLMS, with a projection order of 8, provides an overall reduction that is 2 dB greater than FbNLMS, it requires over 25 times more multiplications, as compared in **Figure 4.7**. Therefore, FbNLMS is the most cost-effective algorithm, achieving a 5.3 dB of

reduction with 1.2×10^4 multiplications. Overall, FbAPLMS with varying projection orders achieves more than 10 dB reduction in the first five harmonics, except for the third harmonic, which shows a 9 dB reduction. This analysis demonstrates the balance between computational complexity and vibration control performance within the system.

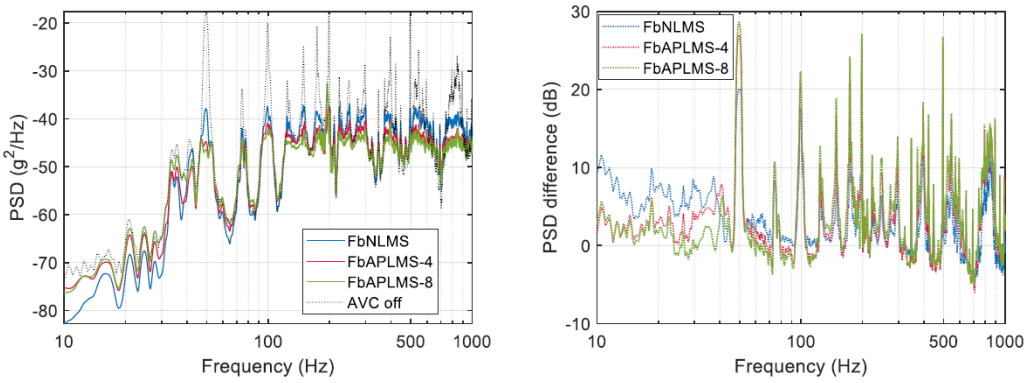

(a) (b)

Figure 4.10: (a) PSD before and after control of different projection orders of FbAPLMS in the static system. (b) PSD difference from 10 Hz to 1 kHz.

Table 4.3: Summary of the AVC performance (dB) of different projection orders of FbAPLMS.

Projection order (M)	**Reduction at f**	**Reduction at $2f$**	**Reduction at $3f$**	**Reduction at $4f$**	**Reduction at $5f$**	**Overall reduction**
1	16.47	22.06	9.30	16.42	19.81	5.26
4	20.08	25.42	12.21	17.57	25.60	6.60
8	21.80	27.11	13.91	18.35	26.73	7.26

4.3.2 AVC of the moving system

For the moving system, the reference sensor was placed at the edge of the linear guide to optimise the feedforward algorithms. This location was selected because it demonstrated better coherence with these specific mid-frequency error signals, optimising the effectiveness in capturing the predominant vibrations to be controlled. A comparison between the vibration signal PSD of two systems before control is shown in **Figure 4.11**. In contrast to the static system, where the spectrum of the error signal is dominated by frequency

contents including 50 Hz, 100 Hz, and its multiple harmonics up to 500 Hz, the spectrum of the error signal in the moving system before control primarily features harmonics of 100 Hz, ranging from 300 to 600 Hz. This difference suggests that the motor movement may contribute to mechanical resonances within the structure, as indicated by the notably higher amplitude of subharmonics in the moving system compared to the static system. Given that the moving stage wheels are engaged with the linear guide, these subharmonics are likely induced by mechanical resonances within the system structure.

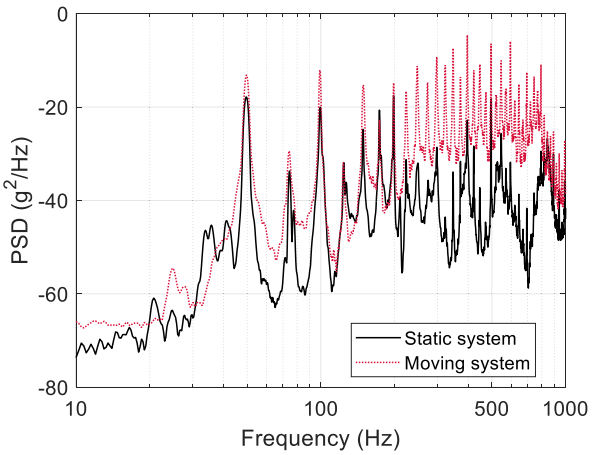

Figure 4.11: Vibration signal PSD measured from moving plate before control for static and moving system.

The PSD of the moving system, both before and after control using feedforward and feedback control algorithms, are presented in **Figure 4.12**. The effects of different control algorithms on PSD difference are illustrated in **Figure 4.13**. Similar to the analysis for the static system, the projection order M was set at 4. When comparing feedforward and feedback algorithms, it is observed that feedback algorithms provide enhanced performance at multiple resonances above 300 Hz than feedforward algorithms, significantly improving the overall performance of the system.

Among the feedforward algorithms, FxAPLMS significantly outperforms the standard FxLMS, achieving higher AVC at multiple harmonics across the spectrum. However, it introduces low-frequency noise below 40Hz and amplifies noise around 120 Hz, with values exceeding 5 dB. In contrast, FxLMS maintains a degraded performance across the spectrum, with reductions at the first and second harmonics approaching 10 dB, but without introducing

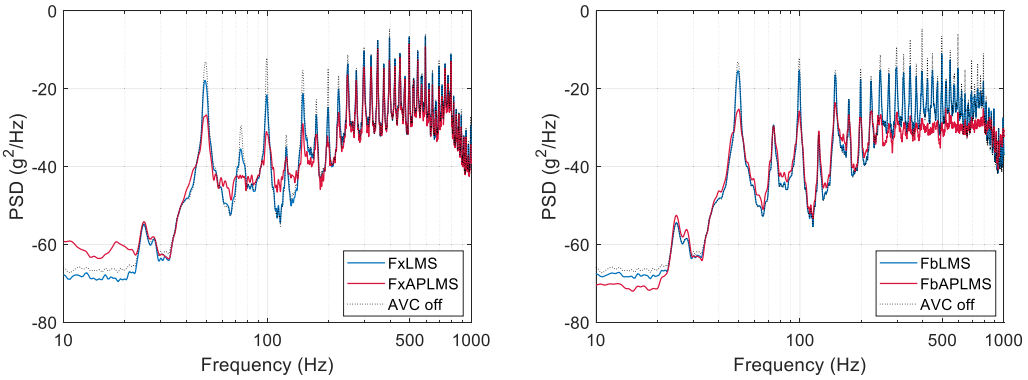

(a) (b)

Figure 4.12: PSD before and after control in the moving system using: (a) feedforward, and (b) feedback algorithms. Projection order M is 4.

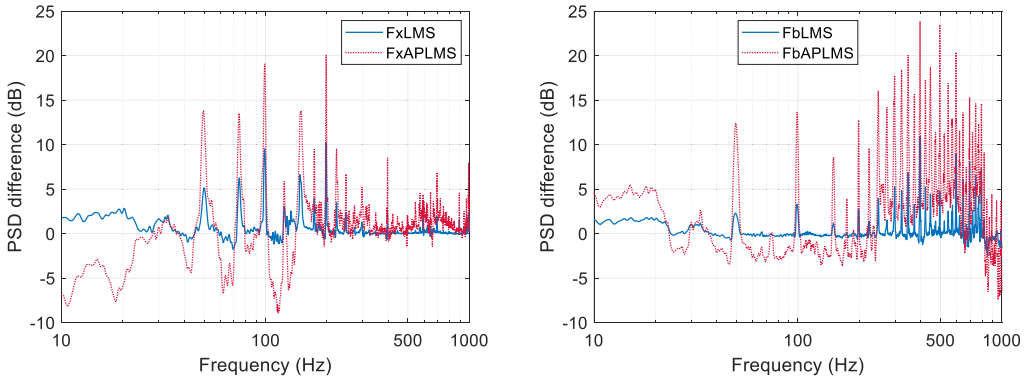

(a) (b)

Figure 4.13: PSD difference after control in the moving system using: (a) feedforward, and (b) feedback algorithms. Projection order M is 4.

significant noise. Among the feedback algorithms, FbAPLMS achieves considerable reduction across the entire spectrum, effectively eliminating the low-frequency noise evident in FxAPLMS. Nevertheless, FbAPLMS exhibits increased high-frequency noise above 800 Hz due to the waterbed effect. FbLMS in this case, while producing minimal high-frequency noise, shows lower vibration reduction at the first two harmonics compared to both FxLMS and FxAPLMS.

Table 4.4 summarises the AVC performance at the first five harmonics for each algorithm. Notably, FbLMS, which incorporates an additional step of estimating the reference signal, achieves a 1.7 dB improvement in overall reduction compared to FxLMS and closely matches the AVC performance of

FxAPLMS, but with significantly lower computational cost, about 13 times less. In contrast to the static system, FxAPLMS demonstrates higher reduction at the first two harmonics than FbAPLMS in the moving system compared to FbAPLMS. Overall, FbLMS is the most cost-effective algorithm, considering its highest ratio of overall reduction to total number of multiplications among all algorithms in the static system. This superior performance of the feedback algorithms, especially in scenarios where the reference signal from the linear guide poorly correlates with the error signal at specific frequencies, demonstrates their potential for more effective vibration control in dynamically complex environments.

Table 4.4: Summary of the vibration reduction (dB) of the moving system.

Algorithms	**Reduction at** f	**Reduction at** $2f$	**Reduction at** $3f$	**Reduction at** $4f$	**Reduction at** $5f$	**Overall reduction**
FxLMS	9.52	9.96	1.14	2.29	0.21	0.58
FxAPLMS ($M = 4$)	18.82	20.07	5.23	8.42	2.02	2.29
FbLMS	3.27	2.73	5.14	10.93	4.73	2.30
FbAPLMS ($M = 4$)	13.66	12.66	17.59	23.87	23.48	5.24

Figure 4.14 presents a comparison of the AVC performance of the FbAPLMS algorithm across different projection orders. With an increase in the projection order (from 1 to 8), the overall vibration reduction is significantly enhanced. This improvement is particularly pronounced at the third, fifth and higher order harmonics, where the most significant peaks in the error signal are observed. The detailed AVC performances of different orders of FbAPLMS are shown in **Table 4.5**, indicating that increasing the projection order from 1 to 4 enhances the overall reduction by 0.7 dB, while requiring more than seven times the computational effort. When the projection order reaches 4 or higher, the reduction across all the first five harmonics exceeds 10 dB, demonstrating the trade-off between increased computational demands and improved vibration control efficiency at higher projection orders.

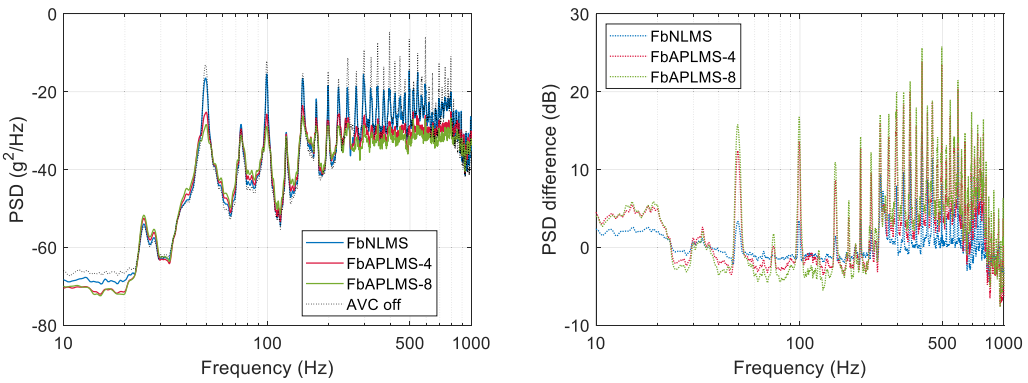

(a) (b)

Figure 4.14: (a) PSD before and after control of different projection orders of FbAPLMS in the moving system. (b) PSD difference from 10 Hz to 1 kHz.

Table 4.5: Summary of the AVC performance (dB) of different projection orders of FbAPLMS.

Projection order (M)	**Reduction at f**	**Reduction at $2f$**	**Reduction at $3f$**	**Reduction at $4f$**	**Reduction at $5f$**	**Overall reduction**
1	3.39	3.55	7.68	14.63	8.23	3.18
4	13.66	12.66	17.59	23.87	23.48	3.84
8	16.73	14.03	19.84	25.64	25.80	4.93

4.3.3 Discussions

The simulation analysis above demonstrates that reference sensor placement is critical to feedforward AVC algorithms. The distance between the reference sensor and the error sensor must be sufficient for feedforward algorithms so that the vibration propagation time exceeds the controller signal update time interval. This, in turn, requires a sufficiently high sampling rate of the system. This constraint does not pose a limitation for the simulation scenario studied here. Another challenge identified relates to the FRF of the actuator, which is influenced by both its structural design and installation location. When the PSA was mounted on the moving stage, its frequency response was dominated by high-frequency contents, as shown in **Figure 4.5b**. Improvement could potentially be achieved by enhancing the rigidity of the mounting structure of PSA, thus reducing variations in performance across different frequencies. Moreover, the inherent modal characteristics of the moving stage, primarily determined by its material properties and

geometry, cause the PSA to behave as a high-pass filter. This actuator response significantly limits control effectiveness in low-frequency scenarios, which are commonly encountered in stepper motor-induced vibrations.

These findings motivated changes to the experimental approach. A feedforward control strategy was adopted instead of a feedback method in the subsequent study. When the PSA was mounted on the moving plate, the high-pass behaviour restricted the low-frequency vibrations, and the strongly time-varying dynamics introduced stability problems in preliminary tests.. This significantly constrained the feasible step size in feedback algorithms and resulted in limited vibration attenuation. Unlike in simulation, these stability issues could not be easily mitigated in the physical setup, making feedforward control the more practical alternative for the experimental validation.

Among the three main structural components (two aluminium rails and one lead screw), the lead screw was the major path of vibration transmission from the stepper motor to the moving stage. In the subsequent experimental study, the PSA was therefore relocated and directly mounted on the lead screw bearing housing to provide the control force with lower frequency characteristics. Although the secondary and primary paths still vary with position, this configuration is expected to enhance actuator performance in vibration control, which is suited to suppressing the dominant motor-induced vibrations. For stability and performance, the final experimental setup used feedforward control with the PSA fixed at the bearing housing.

4.4 The AVC experiment validation

4.4.1 Actuator and sensor locations

In this section, the AVC of a similar moving stage system is investigated through the experiment. Most of the experimental setup remained the same as the study in the previous section. However, the moving plate was made of aluminium alloy with dimensions of $200 \times 100 \times 2$ mm, and the PSA was not mounted on the moving plate, different from the simulation study. The PSA was mounted on the plate through a customised bracket located at the base of the lead screw, as illustrated in **Figure 4.15a**. In this way, the tip of the preloaded PSA was attached to the bearing outer race to provide the vertical force to

the lead screw. This configuration enables the PSA to exert vertical forces against the motor-induced vibrations by interacting directly with a bearing on the lead screw. The motor speed was set to 64 RPM. Different from the study in the previous section, the stepper motor employs 1/8 microstepping to refine the motor movement to enhance smoothness in this section. Additionally, the control signals were adapted in an NI cRIO-9040 CompactRIO controller and output through an NI-9264 C series voltage output module. To minimise external influences, the entire moving stage was secured on a passive vibration control table at both ends. An overview of the moving stage system setup under investigation is shown in **Figure 4.15b**.

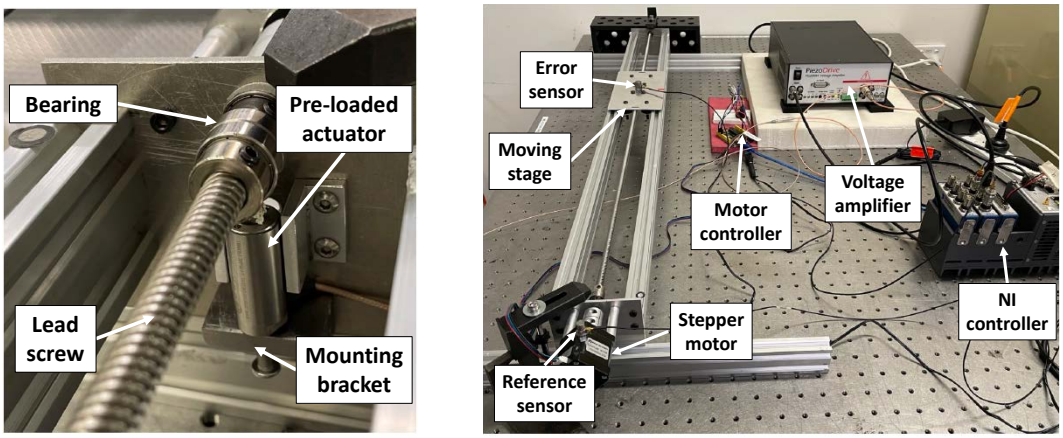

(a) (b)

Figure 4.15: (a) The customised mounting bracket for the PSA. (b) An overview of the moving stage system setup.

This study also utilised a single-channel feedforward AVC system with one reference sensor, one error sensor, and one actuator. The initial focus was on evaluating the placement of the reference sensor and its coherence with the error signal to achieve effective vibration attenuation. The error sensor, located on the plate surface, monitored residual vibrations, as shown in **Figure 4.16a**. Two alternative reference sensor locations were explored, with the coherence function for each determined. The first location is on the top surface of the stepper motor, while the second is at the edge of the linear guide, as detailed in **Figure 4.16b** from top to bottom, respectively.

Figure 4.17 shows the estimated Welch's PSD of the vibration signal from the plate before control. The PSD is calculated by dividing the measured signal into segments of 6400 samples, with a 50% overlap between segments, and

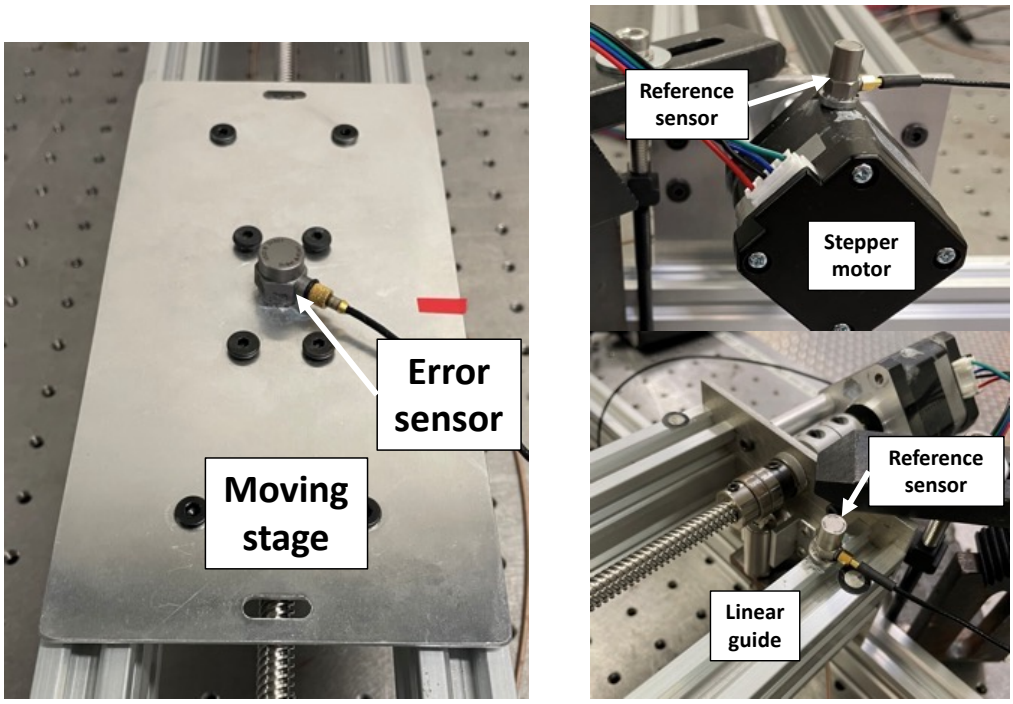

(a) (b)

Figure 4.16: (a) The error sensor on the moving plate. (b) Reference sensor on the motor surface (top) and linear guide edge (bottom), respectively.

the number of spectral lines is 25600. It can be observed that the vibration signal spectrum consists of multiple harmonics of the fundamental frequency at 104 Hz, corresponding to the rotation speed of the stepper motor. Although the 104 Hz fundamental frequency shows a high amplitude in the PSD, the sixteenth harmonic at 1664 Hz was selected as the primary control target in this study due to its proximity to a structural natural frequency identified at 1680 Hz. Modal analysis conducted prior to the control experiments identified natural frequencies of the system at approximately 770 Hz, 1290 Hz, 1680 Hz, etc. Among these, the 1680 Hz mode demonstrated the most significant amplification when excited by the motor harmonics, leading to significant plate vibration. This makes attenuation of the 1664 Hz content critical for effective vibration control. Moreover, due to its physical dimensions, the selected PSA is more effective at higher frequencies, limiting its efficiency in controlling low-frequency content such as 104 Hz. This limitation will be discussed in the subsequent section. Consequently, the AVC system was specifically designed to target vibrations around the 1664 Hz harmonic to address resonance-driven

amplification and maintain system stability. The presence of harmonics can be attributed to the stepper motor's electrical pulse signal, which generates a wide range of frequency components as it takes discrete steps in response to square wave pulses containing both fundamental frequencies and their harmonics.

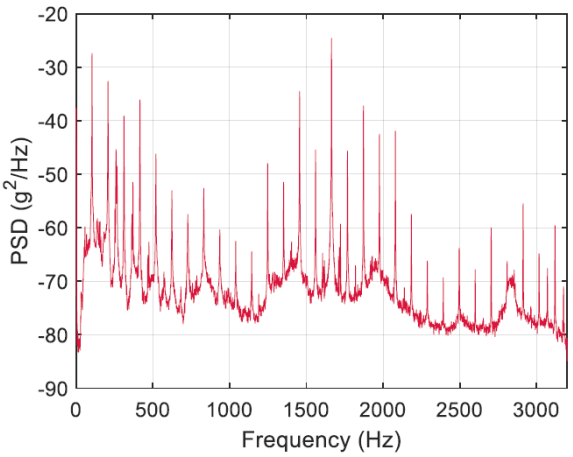

Figure 4.17: PSD of the error signal measured from the moving stage before control.

Figure 4.18a compares the signal coherence of two signals between two reference locations, measured over a complete run of the system. The coherence for the reference sensor location at the motor surface is consistently higher than that at the linear guide across most of the frequency range. However, both reference sensor locations exhibit poor coherence at the peak frequencies of the PSD as shown in **Figure 4.17**, especially at peak harmonics. This issue arises from the constantly varying distance between the reference and error sensors, which results in a weak or inconsistent linear relationship between the signals collected along the linear guide. The motor surface exhibits a coherence function value of 0.49, while the linear guide location yields only 0.04 at 1664 Hz. These variations in signal coherence are due to the distinct structural dynamics at each sensor location, which in turn affect the performance of the feedforward control system. Based on the coherence function c_{re} at the motor surface, the maximum theoretical vibration reduction level (VRL) can be estimated using the following equation [110]:

$$VRL = -10 \times log_{10}(1 - c_{re}) \tag{4.18}$$

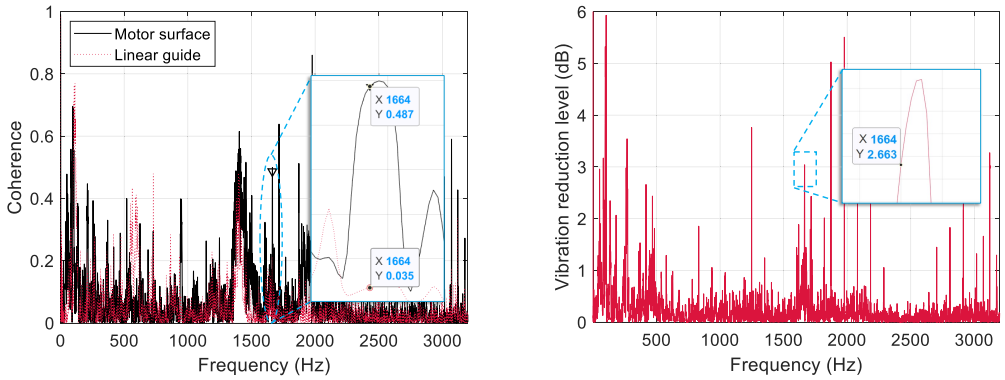

(a) (b)

Figure 4.18: (a) Signal coherence comparison of the reference signal and error signal for each of the two reference sensor locations. (b) Theoretical vibration reduction level around 1664 Hz harmonic.

The theoretical VRL with the reference sensor located at the motor surface is plotted in **Figure 4.18b**. The calculation predicts around 2.7 dB of reduction at the highest peak frequency of 1664 Hz. The predicted VRL is obtained without considering the secondary path in the AVC system. Therefore, to achieve an experimental VRL close to the maximum theoretical VRL, the SPM should exhibit a high-level frequency response at the target frequency. The next section will discuss the secondary path modelling for the system.

4.4.2 Multiple secondary path models of the moving stage

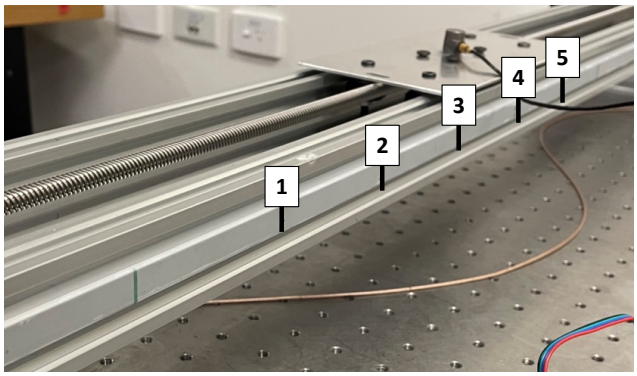

Figure 4.19: Locations of the error accelerometer for the five secondary path models along the linear guide.

The secondary path, defined as the transfer path from the PSA to the error accelerometer, varies continuously as the stage moves from one side to the other. This results in a time-varying secondary path due to changes in distance. Similarly, the primary path, which represents the transfer path from the vibration source to the error accelerometer, also varies throughout the operation. These two time-varying paths indicate the complexity of the system dynamics. To more accurately model the system dynamics and approximate variations between different locations, the segment of the moving stage is divided into five separate regions, marked on the side of the linear guide as shown in **Figure 4.19**. This segmentation represents a practical compromise between modelling accuracy and control system complexity. The five regions correspond to the five SPMs obtained at five error sensor locations (from Location 1 to Location 5), labelled as Model 1 through Model 5. Therefore, the plate is placed at the middle of each region, and the corresponding SPM for each location is modelled by feeding a broadband random noise signal up to 6.4 kHz to the actuator for 10 seconds. The responses, captured by the error accelerometer, are used to produce a FIR filter for each stage location. The impulse responses of these secondary path filters are presented in **Figure 4.20a**, showing only the first 512 samples to enhance clarity in the initial response. This truncation indicates that shorter filter lengths might be feasible without negatively influencing system performance, as long as the phase difference between the estimated model and the system remains within 90 degrees [112]. **Figure 4.20b** illustrates the frequency response functions at the five locations, indicating that frequencies above 1 kHz are significantly higher than those below 1 kHz. This observation suggests that the moving stage system may function similarly to a high-pass filter, which allows higher frequencies to pass through while attenuating lower frequencies. However, the SPMs clearly show better low-frequency response, with less than 20 dB difference in magnitude, when the actuator is located at the current location than in the moving stage location, as shown in **Figure 4.5**.

A detailed view of the frequency responses of the FIR filter at each stage location, shown in magnitude and phase from 1.5 kHz to 1.8 kHz, is presented in **Figure 4.21**. The black dashed line indicates the 1664 Hz frequency. The magnitude responses at 1664 Hz are approximately aligned, with Model 1 and Model 5 showing the lowest responses and Model 4 showing the highest, as

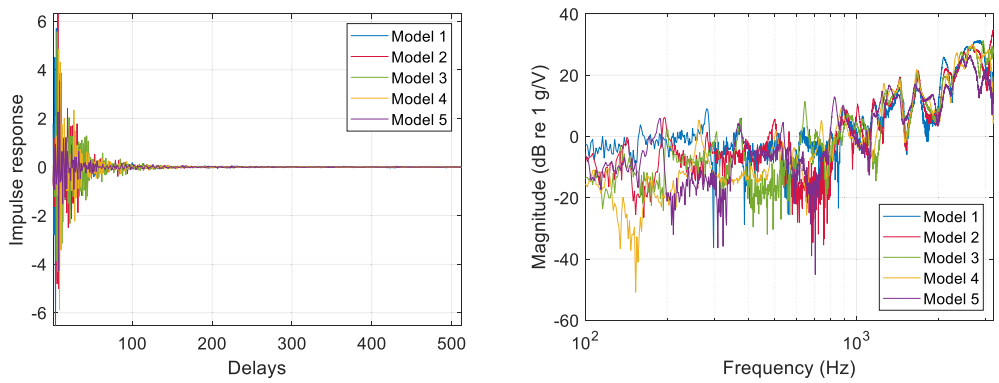

(a) (b)

Figure 4.20: (a) Impulse responses and (b) frequency responses of the five secondary path models.

depicted in **Figure 4.21a**. **Figure 4.21b** illustrates that the phase responses of Model 2 and Model 4 at 1664 Hz are closely aligned, with a phase difference of less than 40 degrees, indicating close system dynamic characteristics for these locations. Similarly, Model 1 and Model 3 also demonstrate closely matched phase responses at 1664 Hz, with the phase difference between the two models remaining within 60 degrees. However, models for any two adjacent locations display phase differences exceeding 90 degrees, confirming the complexity of the system. The length of the FIR control filter in the AVC system L, is 2048 samples, while the length of the FIR filter in the SPM L_s, is 1024 samples. The block diagram representation of the proposed online switching of the SPMs method is demonstrated in **Figure 4.22**.

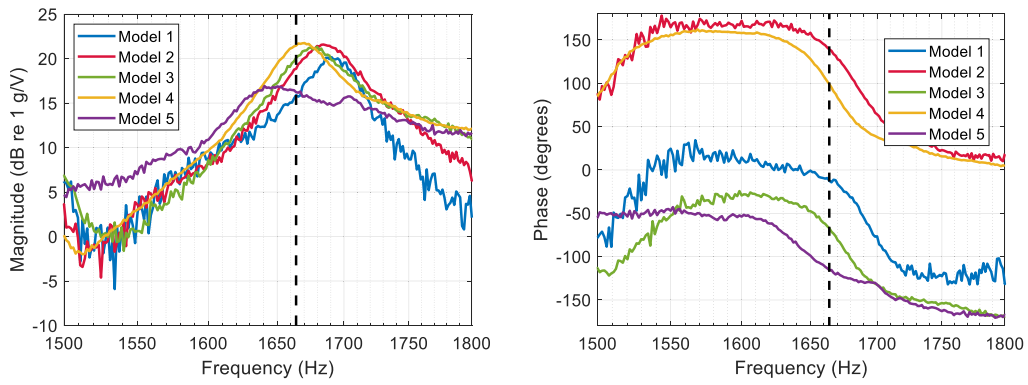

(a) (b)

Figure 4.21: Detailed view of (a) magnitude and (b) phase responses of the five secondary path models.

Unlike the standard FxLMS algorithm, where a single SPM is used throughout the operation, this approach incorporates a location-based switching mechanism to select among multiple pre-identified SPMs. This strategy enables dynamic adaptation to spatial variations in system dynamics without requiring real-time re-identification of the SPMs. It is particularly suitable for repeated back-and-forth movements of the stage, maintaining consistent control performance across cycles. In this diagram, five secondary path models are included, and the selection of the appropriate model is determined based on the specific experimental scenario and the position of the moving stage.

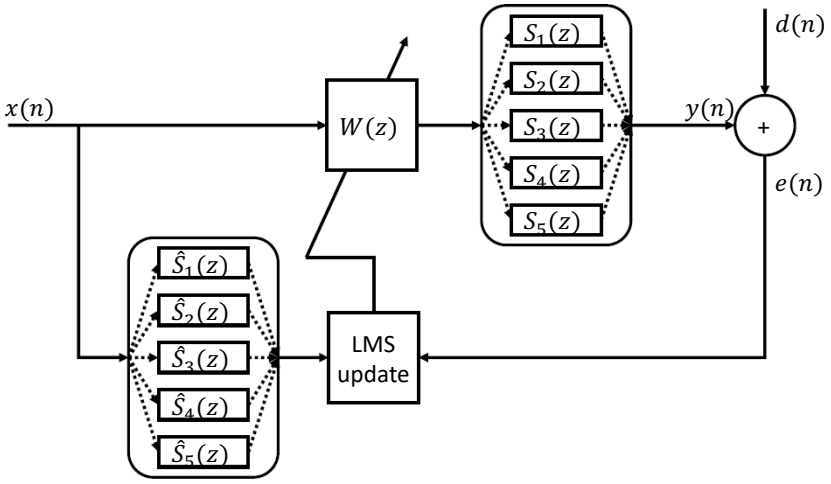

Figure 4.22: Block diagram of the online switching of the SPMs method using five secondary path models.

4.4.3 AVC with single SPM

In this study, five single SPMs were utilised initially in the control system. The motor operated at a speed of 64 rpm, and the length of the movement in the test was 0.32 meters, resulting in a complete operational cycle of around 39 seconds. The vibration level (VL) for each model during the entire motion is calculated using the formula:

$$VL\,(dB) \;=\; 10log_{10}\left(\frac{E_{on}}{E_{off}}\right) \tag{4.19}$$

where E_{on} and E_{off} represent the power of the error signal after and before the AVC system is activated, respectively. These powers are determined by

squaring the error signal. To enhance the readability of the signal, a two-second window is applied to smooth the curves, and the signal is processed by subtracting each initial offset. The vibration level of each model is displayed in **Figure 4.23a**.

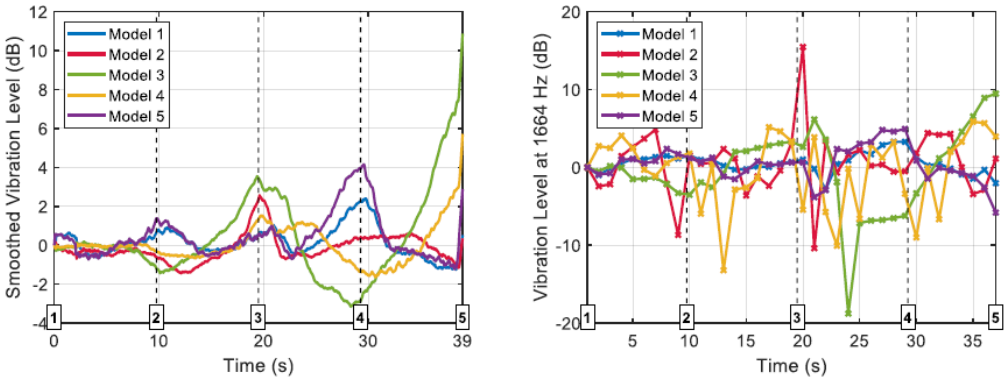

(a) (b)

Figure 4.23: The vibration level of each SPM during operation; (a) smoothed overall and (b) at 1664 Hz. The five numbers along the x-axis correspond to the locations of the five SPMs along the linear guide.

In this figure, a positive value indicates an increase in vibration level, suggesting that the vibration control is ineffective. All five models exhibit fluctuations in vibration level, occurring at different periods during the tests. A consistent step size μ, 3×10^{-7} was used for each SPM. Notably, Model 2 exhibits a temporary reduction in vibration at around 12 to 13 seconds, followed by an increase at around 20 seconds. This fluctuation is attributed to the different phase responses between Model 2 and Model 3, leading to system instability. Similarly, Model 4 shows a reduction in vibration at about 30 seconds but demonstrates an increase at around 20 seconds and after 35 seconds of operation. Models 1, 3 and 5 show significant vibration enhancements and fluctuations during the operation, with Model 3 exhibiting the most pronounced fluctuations, particularly diverging towards the end of the operation. This result indicates that for systems with time-varying secondary paths, the SPM should be updated in real-time to adapt to dynamic system changes.

In **Figure 4.23b**, the vibration level of each SPM at 1664 Hz is compared. The frequency spectra before and after control were calculated using Welch's PSD estimate with a two-second window and 50% overlap. The number of spectral lines was 25600. The vibration level at 1664 Hz is plotted in this

graph once per second. Notably, Model 3 achieves a significant reduction in vibration at around 25 seconds, although it diverges after 30 seconds. Model 4 also demonstrates a fluctuating response throughout the operation time, while it manages to consistently reduce the 1664 Hz harmonics for most of the operation. Conversely, the other models generally increase the vibration level at this frequency or display significant divergence, for example, Model 2, which shows notable instability around 20 seconds.

These observations suggest that the single SPM method is insufficient for effectively suppressing the vibration in the moving stage linear positioning system due to its time-varying system dynamics. The subsequent section presents an experimental evaluation of AVC using an online switching SPM approach.

4.4.4 AVC with online switching SPM using two models

For the online switching SPM method, transitions between different SPMs are based on the operation timeline. Initially, two models were selectively applied among three SPMs (Model 2, Model 3, and Model 4), resulting in three switching combinations: Models 23, 24 and 34. Models 1 and 5 were excluded from this test because their positions at the two sides of the linear guide, as shown in **Figure 4.19**, have been observed to induce instability during transitions between different SPMs. The total movement duration was approximately 39 seconds, with switching implemented at the midpoint (18.5 seconds), thereby dividing the operation into two equal segments. The first SPM was applied during the initial half of the operation, while the second SPM was used for the remainder. The step size μ was 3×10^{-7} , which was similar to the single SPM test and remained constant throughout the operation.

The vibration levels for three different combinations of the two SPMs are compared in **Figure 4.24a**. In all three cases, the second model is switched in after the system passes the location corresponding to Model 3, which is located at the midpoint of the x-axis. Among these cases, Model 23 demonstrates effective vibration reduction around 10 seconds (corresponding to the Model 2 location) and achieves a notable reduction of more than 1.3 dB around 20 seconds (at the Model 3 location). However, around 25 seconds, Model 23 becomes ineffective, with an observed increase in vibration level of approximately 0.5 dB. The result is expected, as continuing to use Model 3 after 25

seconds introduces a phase error relative to the actual secondary path, which is more accurately represented by Model 4. Model 34 exhibits an increase in vibration from 5 to 15 seconds, reaching a peak increase of approximately 1 dB at 10 seconds (at the Model 2 location). After 15 seconds, as the stage moves towards the midpoint, the model begins to show a reduction in vibration, achieving around 1 dB of reduction at 20 seconds (at the Model 3 location). Following a slight fluctuation, Model 34 becomes increasingly effective after around 33 seconds, once the system passes the Model 4 location, and achieves a maximum reduction of around 2 dB throughout the process. Among the three models, Model 24 provides the most consistent vibration reduction throughout the operation, showing a notable vibration reduction after 25 seconds, with an overall reduction exceeding 1.9 dB around 30 seconds (at the Model 4 location). Additionally, it achieves 0.8 dB of reduction around 10 seconds (at the Model 2 location). However, a slight fluctuation is observed after around 20 seconds (at the Model 3 location), indicating that Model 24 may not accurately represent the secondary path at that position. The limited reduction observed in this system can be attributed to its time-varying primary and secondary paths, which tend to make the algorithm prone to divergence when the phase error between the actual secondary path and the modelled secondary path exceeds 90 degrees. As a result, increasing the step size may cause instability, while decreasing it constrains the achievable control performance during operation.

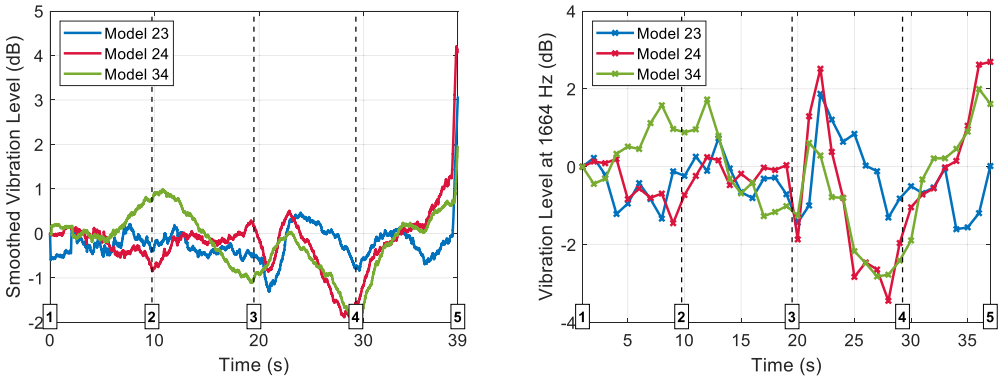

(a) (b)

Figure 4.24: The vibration level of each online switching SPM using two models during operation; (a) smoothed overall and (b) at 1664 Hz. The five numbers along the x-axis correspond to the locations of the five SPMs along the linear guide.

Figure 4.24b displays the vibration level at 1664 Hz for the three online switching SPMs. Similarly, the frequency spectra before and after control were calculated using Welch's PSD estimate with a two-second window and 50% overlap, and the number of FFT points was 25600. The data are plotted for each second to provide a detailed view of the changes in vibration level over time. During the first half of the operation, both Model 23 and Model 24 effectively suppress the sixteenth harmonic content. By contrast, Model 34 exhibits an increase in harmonic content as the stage approaches the Model 2 location. During the second half of the operation, all three models initially show an increase in harmonic content, followed by a reduction in vibration levels. Among the three combinations, Model 24 and Model 34, both employing Model 4 during the latter half, demonstrate significant vibration attenuation. Specifically, Model 34 achieves a reduction of 2.8 dB around 28 seconds, while Model 24 achieves a reduction of more than 3.4 dB. In contrast, Model 23 exhibits limited attenuation during this period, with a maximum reduction of 1.6 dB. As shown in **Figure 4.24b**, all three models diverge towards the end of the plate movement. This divergence occurs as the plate approaches the far end of the linear guide, indicating that the application of only two SPMs throughout the entire operation is insufficient to accurately represent the system dynamic behaviour.

4.4.5 AVC with online switching SPM using three models

To further enhance performance and stability, an additional SPM was incorporated into the online switching method. In this configuration, Models 2, 3 and 4 were applied sequentially, with each model covering one-third of the total operation time. Specifically, Model 2 was used from the beginning of the operation until 13 seconds, followed by Model 3 from 13 to 26 seconds, and Model 4 was applied for the remaining duration of the operation.

The Model 234 configuration effectively controls vibration throughout the operation, and its performance is evaluated against the two-SPM method as shown in **Figure 4.25a**. Model 234 demonstrates effective vibration attenuation throughout the entire operation and outperforms the two-SPM configurations at various time periods. At the Model 2 location, Model 234 achieves the highest vibration reduction, approaching 1 dB. Around the Model 3 location, it maintains a similar level of performance, also around 1 dB. At

the Model 4 location, it shows the highest reduction, reaching approximately 2.1 dB. Furthermore, the maximum increase in vibration observed is limited to only 0.2 dB, indicating the stability of the three-model method. The sixteenth harmonic content at 1664 Hz is also significantly reduced using this configuration, as shown in **Figure 4.25b**. At the Model 2 location, a reduction of 2 dB is achieved, followed by 1.9 dB at the Model 3 location, and 4 dB at Model 4. The complete comparison of the overall vibration reduction level of Model 234 with two-model SPMs is listed in **Table 4.6**. The reduction of the sixteenth harmonic is summarised in **Table 4.7**. Model 234 demonstrates consistently better performance across different locations, especially in attenuating harmonic content. These results demonstrate that the online switching method using three SPMs provides not only higher vibration reduction but also enhanced stability across the entire operational period, outperforming all other online switching configurations evaluated in this study.

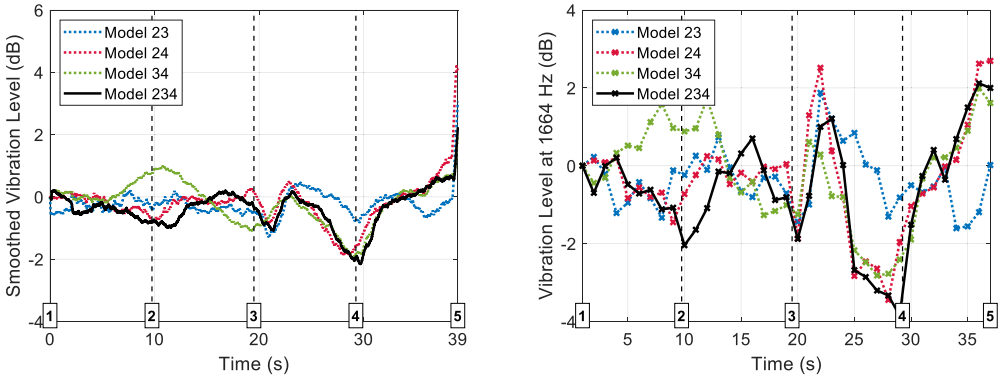

(a) (b)

Figure 4.25: Comparison between using three SPMs (Model 234) with using two SPMs regarding vibration level during operation; (a) smoothed overall and (b) at 1664 Hz. The five numbers along the x-axis correspond to the locations of the five SPMs along the linear guide.

Figure 4.26a compares the PSD of the system obtained from simulation, experiment, and uncontrolled case over the period from 25 to 31 seconds, with a special focus on the sixteenth harmonic content at 1664 Hz. The simulation was conducted in MATLAB® using parameters consistent with the experimental setup. A slight difference is observed between the simulated and experimental results for Model 234, with the experiment showing a reduction of approximately 2.7 dB, 0.3 dB smaller than the simulation case. This discrep-

Table 4.6: Overall vibration reduction level of each online switching SPMs at three locations along the linear guide.

Overall vibration reduction level (dB)	**Location 2**	**Location 3**	**Location 4**
Model 23	0.35	0.48	0.78
Model 24	0.82	-0.16	1.56
Model 34	-0.77	1.01	1.84
Model 234	0.80	0.35	1.93

Table 4.7: Vibration reduction level at 1664 Hz for each online switching SPMs at three locations along the linear.

1664 Hz vibration reduction level (dB)	**Location 2**	**Location 3**	**Location 4**
Model 23	0.24	0.71	0.82
Model 24	0.73	-0.04	1.96
Model 34	-0.88	1.01	2.41
Model 234	2.04	0.81	3.86

ancy may be attributed to several factors. First, there is an estimation error between the modelled and actual SPM. Secondly, instability from switching between SPM while the PSA output has not fully decayed due to the system's low damping characteristics could also affect the results. Additionally, the possible nonlinearities in the system also contribute to the inaccuracy between the results.

Figure 4.26b compares the vibration signals measured by the error sensor when the control system is turned on and off during the period from 25 to 31 seconds. The signal contains multiple harmonics, as previously shown in **Figure 4.17**. The amplitudes of these harmonics vary over time throughout the operation, as observed in the time-domain signal. This variation requires the use of a relatively small step size to prevent system divergence. By applying the online switching of SPM method with Model 234, the overall vibration level is reduced by around 2 dB at Location 4, with a peak reduction of 4 dB at 1664 Hz harmonic. This level of performance could not be achieved using a single SPM. These results demonstrate the stability and effectiveness of using

a multiple-SPM switching configuration for vibration control in time-varying systems.

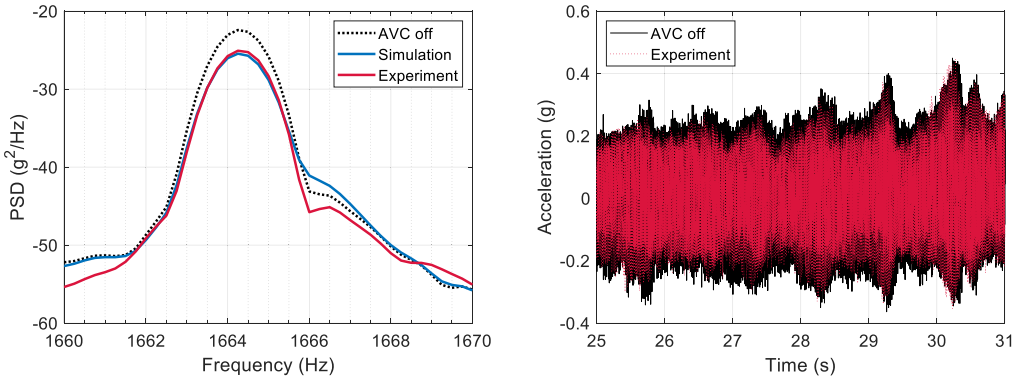

(a) (b)

Figure 4.26: (a) PSD comparison of Model 24 for experiment and simulation during 25 to 31 seconds. (b) Vibration comparison in time domain between AVC off and on.

4.4.6 Discussions

While five discrete SPMs allow the AVC system to account for spatial variation along the linear guide, the present implementation uses an abrupt switching technique between models. This method assumes instantaneous transitions and does not capture gradual changes in system dynamics between measurement points. In **Figure 4.20b**, phase differences between adjacent SPMs at 1664 Hz often exceed 90 degrees, which can cause phase mismatch and degraded control performance during switching. Experimental results show that switching between different SPMs produces abrupt shifts in the secondary path output, especially when the internal state of the adaptive filter is not aligned with the newly selected model. This behaviour appears as fluctuating performance and short divergence periods in the two-SPM configurations reported in **Section 4.4.3**.

There is a trade-off in the selecting the number of SPMs used in the system. A smaller number of SPMs simplifies implementation but compromises modelling accuracy, while a larger number of SPMs increases the likelihood of instability and can degrade overall control performance. This study used five SPMs to balance accuracy and stability. Although the three-SPM configuration

(Model 234) demonstrated improved vibration attenuation and system stability, further refinements may be achieved through interpolated or adaptive switching methods that better reflect the continuous variation in the secondary path. Linear interpolation between neighbouring SPMs is one practical option to smooth transitions and mitigate the adverse effects of abrupt switching, as reported elsewhere [98].

Although the control system targeted the sixteenth harmonic at 1664 Hz effectively, the time-domain overall vibration attenuation in **Figure 4.26b** is modest, especially at low frequencies. Three main factors contribute to this result. First, limited coherence between the reference and error sensors inherently constrained the maximum achievable reduction, as indicated in **Figure 4.18b**. Second, the complex and time-varying dynamics of the moving stage system required a relatively small step size to prevent system divergence and thus constrained the adaptation rate. Third, the performance of the selected PSA was limited at lower frequencies due to its compact geometry, which was constrained by the need to fit within the structure. As a result, significantly more energy is required for the actuator to operate effectively in this frequency range. Consequently, differences between the AVC-on and AVC-off signals in the time domain are small. Nevertheless, the experimental reduction closely aligns with the simulation results shown in **Figure 4.26a**, suggesting that the AVC system operated near its theoretical performance limit under the given constraints. Further improvements in sensor coherence and optimisation of the PSA design will be critical to further enhance vibration suppression capabilities.

4.5 Summary

This chapter investigates the AVC of a stepper motor-driven moving stage linear positioning system with time-varying primary vibration sources. In the first part, a PSA is customised and mounted on the moving stage. Feedforward and feedback-based APLMS algorithms are evaluated through simulations. Two candidate reference sensor locations were first assessed by their coherence for feedforward algorithms. To address scenarios where the reference signal exhibits low correlation with the target vibration, a feedback variant FbAPLMS was proposed. In the moving system scenario, FbAPLMS achieved a

5.2 dB reduction, exceeding FxAPLMS by 3 dB, with only about 10% additional computational cost. Unlike feedforward approaches, FbLMS and FbAPLMS maintained performance under poor coherence between the reference and error signals, which is important for time-varying dynamics where optimal coherence is difficult to maintain. Additionally, the feedback algorithms in both system configurations effectively attenuate low-frequency noise below 40 Hz, contributing to system stability by preventing amplification of low-frequency disturbances. However, a practical limitation observed during experimental implementation is the instability when higher step sizes are used in feedback algorithms, which in turn restricts the achievable control performance.

The second part focuses on how varying SPMs affect AVC performance in experiments on the same moving stage linear positioning system. Different from the previous study, the PSA was mounted on the linear guide, introducing time-varying secondary paths. Two candidate reference sensor locations were again evaluated via coherence. The predicted theoretical vibration reduction level reached 2.7 dB at the sixteenth harmonic of the motor at 1664 Hz. This harmonic, the most prominent in the frequency spectrum of the error signal, arises from stepper motor microstepping and lies close to one of the structural modes near 1680 Hz, which amplifies that harmonic. Five error sensor locations were placed evenly along the linear guide to define five distinct SPMs. Experimental results show that using a single SPM provided limited control performance and was prone to instability due to the mismatch between the modelled and actual secondary path. An online switching of SPMs scheme was therefore implemented. The experimental results demonstrated that switching among three SPMs improved the control performance, and reduced approximately 2 dB at Location 4 and up to 4 dB at 1664 Hz. These results indicate that the model switching method can enhance the smoothness and stability in linear positioning systems.

Future research should improve the coherence of reference and error signals to address the current performance limitation for feedforward control. Increasing the number of SPMs in the online switching SPM method may further improve system stability and performance. Additionally, implementing interpolation between SPMs provides smoother transitions and reduces instability associated with abrupt model switching. Furthermore, the performance of the PSA could be optimised by improving the structural rigidity of

its mounting structure. This would help enhance actuator performance across a wider frequency range. Finally, to address the limitations of low coherence in feedforward control and step size constraints in feedback control, a hybrid approach that integrates both strategies should be explored in future work.

CHAPTER 5

Active Vibration Control of a Fused Filament Fabrication 3D printer under environmental vibrations

5.1 Introduction

Studies have shown that fused filament fabrication (FFF) frequently suffers from poor surface finish due to inherent mechanical vibrations from the print head and build plate motion [25], and surface waviness, also known as ringing or ghosting due to the stepper motor skipping counts [33]. When printing in vibration-prone environments, the frequency of the environmental vibration may coincide with the structural natural frequencies of the 3D printer, which leads to increased geometric inaccuracies and defects. In maritime environments, vibration characteristics include low-frequency hull vibrations induced by ocean waves and higher-frequency forced vibrations generated by the engine and propeller [113, 114]. Gyro-stabilised platforms, used for decades, can stabilise these motions. For instance, Phillips et al. employed a gyro-stabilised platform to operate a stereolithography 3D printer, successfully printing an underwater pressure shell in a dynamic ship environment with results comparable to those printed in a land-based environment [37]. Previous research has demonstrated that base vibrations significantly affect surface roughness, leading to a degradation in part quality [41]. In order to mitigate

these base vibrations, a passive vibration control method was used, which improved the surface roughness of the printed parts by 16%. However, traditional passive techniques target vibration reduction at specific, narrowband frequencies. Their performance degrades when base vibration frequencies and amplitudes fluctuate, as is common in shipboard and vehicular environments where engine speeds and operational conditions vary continually.

Active control methods provide a dynamic approach to vibration control as they can track and adapt to system changes in real time. Due to the complexity and high dynamic properties of the 3D printer system, especially when the printing speeds vary, applying model-based active control algorithms is challenging. The FxLMS algorithm is a suitable algorithm which does not require detailed knowledge of the system model. In multi-axis (or multi-degree-of-freedom) systems such as 3D printers, robotic arms [115], and machine tools [116], dynamic behaviour between axes is coupled because axes often share structural components such as frames, motors, and belts. As a result, vibrations in one axis can transfer to adjacent axes through these shared elements, meaning that vibrations in one axis of the 3D printer can induce vibrations in other axes. In the context of 3D printing, the FxLMS algorithm faces unique challenges, such as maintaining stability during abrupt print head speed changes and mitigating cross-coupling effects between multi-axis vibrations. While the FxLMS algorithm has been mostly validated in single-axis systems, its suitability for multi-axis 3D printer systems remains under-explored.

This chapter, therefore, investigates the application of a feedforward FxLMS-based active vibration control system to a desktop-scale FFF printer. The focus is on analysing the vibration transmission paths, and evaluating the control system's ability to suppress structural vibrations under single- and multi-frequency base excitations. Experimental and simulation results are used to validate the effectiveness, adaptability, and stability of the algorithm. The resulting improvements in printed surface quality are used as a secondary indicator of system performance, demonstrating the broader applicability of the proposed approach to other vibration-sensitive dynamic positioning systems in vibration-prone environments.

5.2 3D printer AVC system

In this study, the printing performance of an EasyThreed K7 FFF 3D printer was investigated under dynamic and challenging conditions. To replicate real-world environments in a laboratory setting, the external vibration, referred to as the primary vibration, was introduced using an electrodynamic shaker with an integrated amplifier (The Modal Shop K2004E01), which acts as the disturbance shaker. The primary vibration signal was provided by the Instek multi-channel function generator (MGF-2260MFA). A second electrodynamic shaker (B&K LDS V201), driven by a linear power amplifier (B&K LDS LPA100), served as the control shaker. To monitor these vibrations, several IEPE accelerometers were used. A uniaxial impedance head (DJB AF/100/10), which integrates an IEPE accelerometer and a force transducer, was used to monitor the input vibration acceleration and force signals applied to the 3D printer; the accelerometer served as the reference sensor. Additionally, a triaxial accelerometer (B&K Type 4506 B) was used as the error sensor, while another similar triaxial accelerometer (B&K Type 4506 B) monitored the print head vibration during printing. All sensor signals were conditioned and captured on an NI-9234 C series input module, which digitised the inputs for subsequent analysis and processing by the NI LabVIEW-based control system. The control signals were generated by an NI cRIO-9040 CompactRIO controller and output via an NI-9264 C series voltage output module to the control shaker. This system operated at a sampling frequency of 6.4 kHz and utilised NI LabVIEW software for data acquisition, signal processing and control execution. The schematic of the entire system is shown in **Figure 5.1**.

5.3 Dynamic characteristics of the system

5.3.1 3D printer structure

The FFF 3D printer under investigation consists of several primary structural components: a base frame (housing for 3D printer electronics and the cooling system), a build plate (print bed), a print head (extruder assembly), an x-axis gantry, an x-axis motor, a z-axis gantry, and a z-axis motor housing as shown in **Figure 5.2**. During the printing process, the print head moves along the x-axis, while the build plate moves along the y-axis. Vibrational disturbances caused

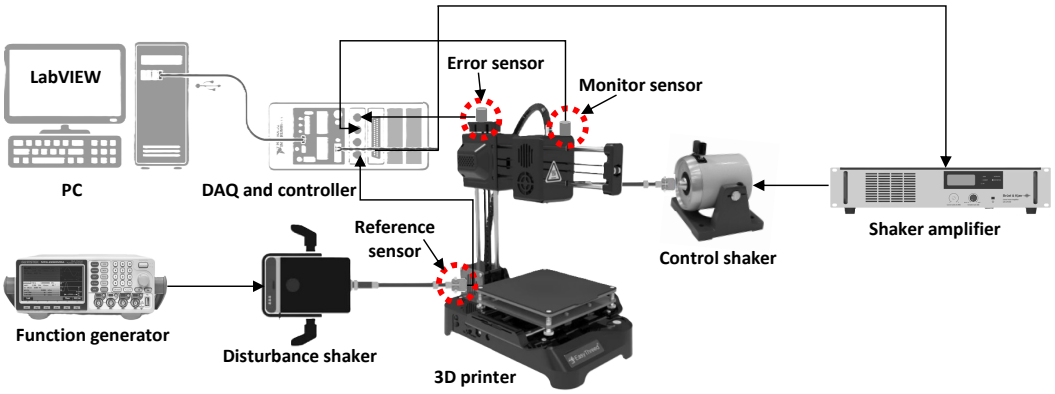

Figure 5.1: The schematic of the 3D printer AVC system. Three main accelerometers are highlighted in red circles.

by the print head and build plate motion can induce positional inaccuracies, leading to dimensional deviations in printed components. The print head, mounted on the x-axis gantry, behaves as a moving mass along a cantilevered beam-like structure. As the print head travels from the x-axis motor housing toward the free end of the x-axis gantry, the increase of the effective mass leads to greater deflection and a lower effective stiffness-to-mass ratio. This mass redistribution alters the system dynamic characteristics, reducing its natural frequency and amplifying vibrational amplitudes, thereby increasing the complexity of direct AVC of the print head.

5.3.2 Primary path modelling

As vibrations along all three axes contribute to the dimensional deviations in printed components, external disturbances are applied in different directions at the edges of the base frame to maximise their effect on the 3D printer, as shown in **Figure 5.3**. After initial experimental investigations, it was found that when the external vibration was applied along the y-axis (as shown on the left), the highest acceleration amplitudes were observed across different locations of the 3D printer. Consequently, in this study, external vibrations were all applied along the y-axis.

Next, the placement of the error sensor is carefully considered. During the printing process, the motion of the print head induces time-varying dynamic characteristics. If the error sensor is located on the print head, both the primary path and the secondary path exhibit time-varying behaviour. A

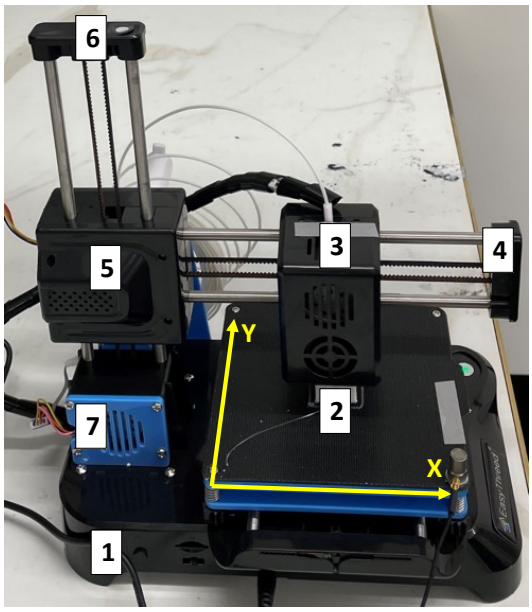

Figure 5.2: Primary components of an EasyThreed K7 3D printer: 1. Base frame. 2. Build plate. 3. Print head. 4. x-axis gantry. 5. x-axis motor housing. 6. z-axis gantry. 7. z-axis motor housing.

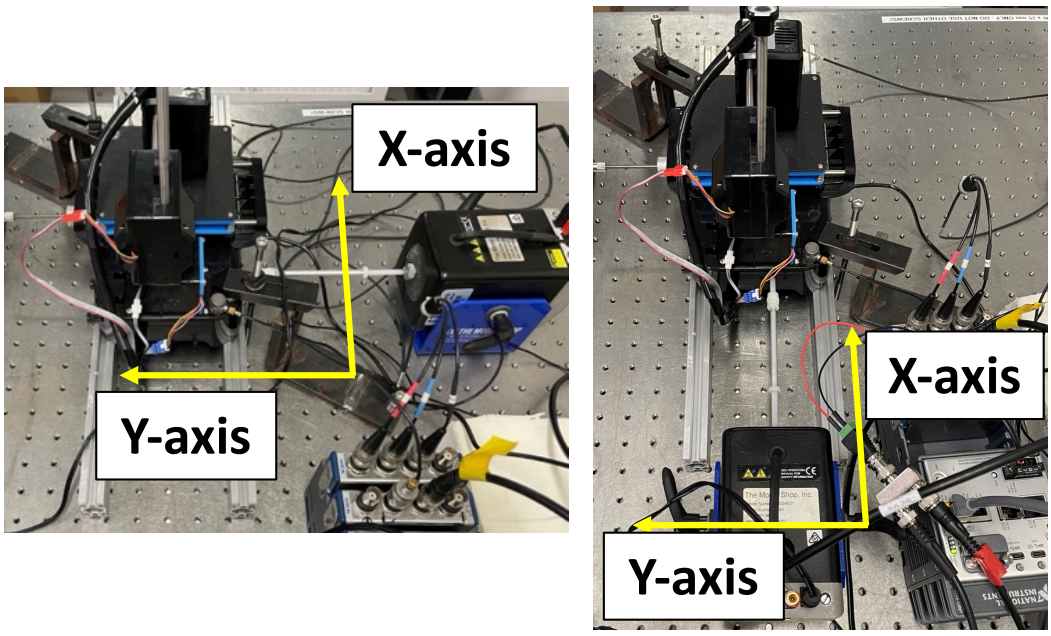

Figure 5.3: Two different external disturbance directions. Y-axis external vibration (left), and x-axis external vibration (right).

continuous online modelling of the secondary path is required for the control system to maintain an accurate model. Moreover, the vibration propagation through the primary path is highly dynamic due to the varying length of the primary path as the print head moves, which greatly complicates the control process. The detailed analysis of the print head dynamic characteristics will be discussed in **Section 5.3.3**. To address these challenges, the error accelerometer is strategically placed at the x-axis motor housing for several reasons. First, during the printing process, all vibrations from the base frame propagate from the motor housing to the print head, making this location ideal for capturing the dominant vibration components transmitted through the structure. Additionally, since the motor housing moves only after the completion of each layer of material deposition, the secondary path model remains almost unchanged, eliminating the need for continuous online modelling.

Locations of the disturbance shaker and the error accelerometer in this study are shown in **Figure 5.4a**. The disturbance shaker was mounted horizontally on the bench and connected via a nylon stinger. An aluminium shaft sleeve was attached to one end of the stinger to enhance rigidity and prevent off-axis force output to the z-axis motor housing. At the interface between the stinger and the housing, a reference impedance head was installed. This sensor, which integrates both an accelerometer and a force transducer, was used to measure both the input acceleration and force delivered by the disturbance shaker. The primary path was modelled by exciting the disturbance shaker with a broadband random noise signal to 6.4 kHz for 10 seconds. The response, captured by the error accelerometer, was used to generate a finite impulse response FIR filter for a length of 1024 samples.

The structural displacement amplitude influences the dimensional deviations of printed components. Therefore, to better assess the impact of vibrations on print quality in the frequency domain, the measured acceleration signals are double-integrated to obtain displacement signals for comparative analysis.

For a given acceleration signal in the form of a sine wave:

$$a(t) = A_a sin(2\pi f t + \phi) \tag{5.1}$$

where A_a is the acceleration amplitude in m/s^2, f is the frequency in Hz, t is time, and ϕ is the phase in radians. Velocity is obtained by integrating

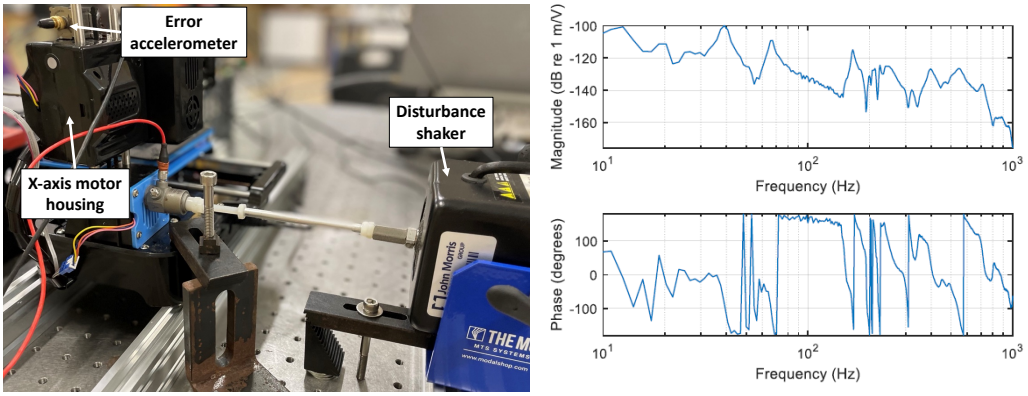

(a) (b)

Figure 5.4: (a) Locations of the error sensor and the disturbance shaker. (b) Modelled frequency response function of the primary path FIR filter in displacement.

acceleration:

$$v(t) = \int a(t)dt = -\frac{A_a}{2\pi f}cos(2\pi f t + \phi) + C_1 \tag{5.2}$$

where C_1 is the constant of integration representing the initial velocity. Next, integrate velocity to get displacement:

$$x(t) = \int v(t)dt = -\frac{A_a}{(2\pi f)^2}sin(2\pi f t + \phi) + C_1 t + C_2 \tag{5.3}$$

where C_2 represents an initial displacement, and the term $C_1 t$ is a linear drift if there is an initial velocity. In our case, there is no initial velocity or displacement, and the negative sign means the direction of the displacement and can be removed. The simplified equation of the displacement for a sinusoidal acceleration signal is:

$$x(t) = -\frac{A_a}{(2\pi f)^2}sin(2\pi f t + \phi) \tag{5.4}$$

The peak displacement of a given sine wave acceleration signal is $\frac{A_a}{(2\pi f)^2}$. The modelled acceleration FIR filter is subsequently integrated into displacement form, as described in **Equation 5.1 - 5.4**. The FRF of the primary path is presented in **Figure 5.4b**. The first peak in the FRF plot, occurring around 40 Hz, corresponds to the first natural frequency of the system and exhibits the highest displacement amplitude. Additionally, a second peak appears at approximately 65 Hz, close to the first. These two peaks indicate a strong low-frequency response of the primary path, confirming the suitability of the disturbance shaker location for inducing high levels of displacement excitation.

5.3.3 Secondary path modelling

The control shaker was mounted horizontally on the bench and connected to a stinger, which was attached to the x-axis motor housing to provide y-axis control force. The location of the control shaker is shown in **Figure 5.5a**. Similarly, the secondary path was modelled by exciting the control shaker with a broadband random noise signal up to 6.4 kHz for 10 seconds, to generate an FIR filter. The FRF of the secondary path model in displacement form is shown in **Figure 5.5b**. The FRF of the filter indicates that the highest peak occurs around 50 Hz. This model shows an outstanding low-frequency response, which ensures the effectiveness of the control shaker at target frequencies. To further compare print head dynamics at different locations along the x-axis gantry, a detailed discussion of print head dynamics at different locations is presented.

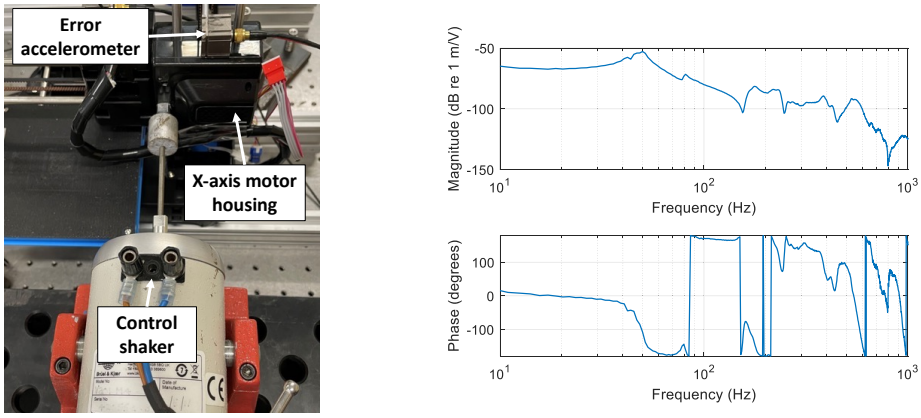

(a) (b)

Figure 5.5: (a) Location of the control shaker. (b) Modelled frequency response function of the secondary path FIR filter in displacement.

As discussed in **Section 5.3.2**, direct vibration control of the print head is challenging due to its time-varying dynamic characteristics. To validate the print head dynamics at different positions along the x-axis gantry, four transfer paths between the control shaker and print head responses are modelled at the four corners of the print plane. **Figure 5.6a** illustrates four farthest positions the print head can be moved on the build plate. Locations 1 and 4 share the same print head location on the x-axis gantry, and locations 2 and 3 share the same print head location on the x-axis gantry. The control shaker setup remains consistent with the secondary path modelling, while the error accelerometer in this case moves to the print head. Four transfer paths

can then be modelled and the impulse responses of the four FIR filters are presented in **Figure 5.6b**. The original acceleration signals are used without converting to displacement. Although the amplitude responses of the four models are similar, their frequency responses differ. The frequency responses of the four filters in magnitude and phase are presented in **Figure 5.7**. Notably, model 1 and model 4 exhibit similar magnitude responses, while their phase responses diverge significantly in the low-frequency range below 100 Hz, with phase differences exceeding 90 degrees. This large phase difference could negatively influence AVC performance if only a single secondary path model is employed for all the print head locations [112]. In contrast, Model 2 and Model 3 differ in both magnitude and phase in the low-frequency range, indicating the location-dependent nature of the print head dynamics. The time-varying dynamic characteristics of the print head confirm the necessity of relocating the error accelerometer to the x-axis motor housing to enable practical and stable vibration control. Continuously updating multiple secondary path models in real time based on the print head position becomes significantly more complicated, particularly when printing geometries with frequent directional changes and position shifts.

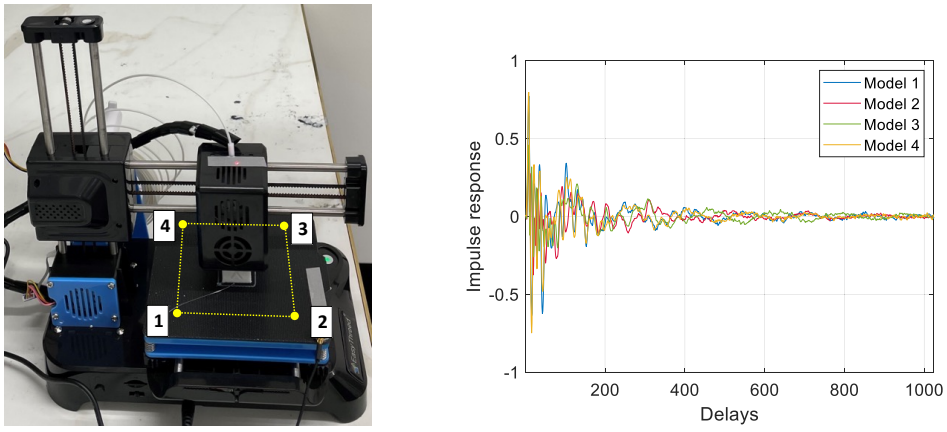

(a) (b)

Figure 5.6: (a) Four modelling locations of the print head on the build plate. (b) Corresponding impulse responses of the four modelled transfer paths.

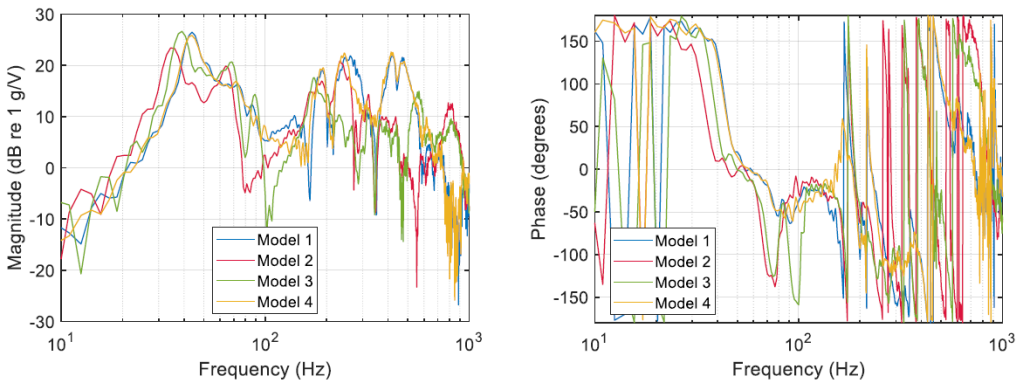

(a) (b)

Figure 5.7: (a) Magnitude and (b) phase responses of the four models.

5.4 AVC simulation of 3D printer

The geometry of the printed sample was a $50 \times 50 \times 10$ mm cuboid thin-walled structure with no infills, roof, and floor layers, as illustrated in **Figure 5.8**. PLA filament was used as the printing material in this study. The printing parameters of the 3D printer are listed in **Table 5.1**. The printed part consists of two wall layers: the outer wall structure (red region) and the inner wall structure (green region). The entire sample takes approximately 16.3 minutes to complete, with each layer requiring around 20 seconds to print two walls.

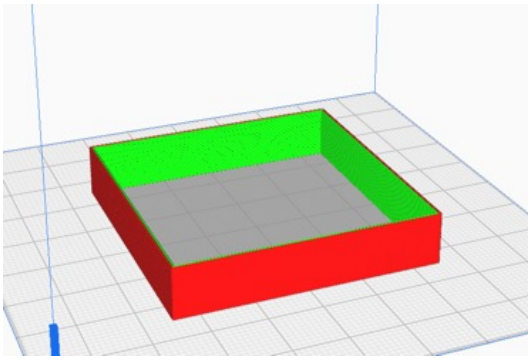

Figure 5.8: The illustration of the cuboid structure in this study.

Table 5.1: 3D printer printing parameters in this study.

Printing parameters	Value
Print speed (mm/s)	30
Layer height (mm)	0.2
Number of layers	50
Wall thickness (mm)	0.8
Number of walls	2

5.4.1 3D printing under single-frequency and amplitude excitation

To evaluate the suitability of the feedforward FxLMS algorithm for vibration control in a 3D printer application, a simulation of the AVC system was performed. The first simulation scenario involves AVC implementation under single-frequency and amplitude sinusoidal excitation. The disturbance shaker was driven with a 52 Hz sinusoidal signal with an amplitude of 0.15 V. This is a frequency close to the first and the second natural frequencies of the 3D printer system. To accommodate the high dynamic variation of vibration signals during printing, the step size of the algorithm was set to 5×10^{-9} , with both the secondary path filter and the controller configured to a length of 1024 samples. This filter length is selected to balance computational cost and control performance, as increasing the filter length to 2048 samples offers limited performance improvement while nearly doubling the computational cost after comparison. Reference signals and error signals used for the simulation are recorded throughout the entire printing process, with external vibrations induced by the disturbance shaker.

A time-domain comparison of error signals with and without AVC for the first 50 seconds is presented in **Figure 5.9a**, showing a high reduction in error signal acceleration after 8 seconds of controller activation. The control voltage output, depicted in **Figure 5.9b**, demonstrates rapid convergence, achieving stabilisation within approximately 6 seconds after activation of AVC. However, persistent fluctuations in output voltage are observed throughout the entire printing process. The period of these fluctuations corresponds to the time required for the deposition of each layer of material. These fluctuations are attributed to dynamic variations during x-axis motion of the print head from one side to another, which leads to fluctuations of vibration amplitude

during layer deposition. Simulation results show that the PSD of the error signal is reduced by 6.63 dB over the full printing duration, and the 52 Hz peak is attenuated by 8.65 dB compared to the scenario without AVC.

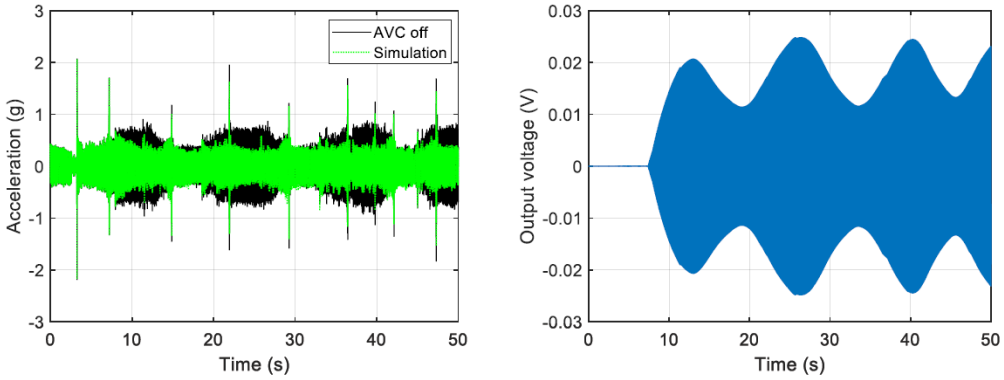

(a) (b)

Figure 5.9: (a) Comparison between simulation and no AVC of the error signals in the time domain, and (b) controller output voltage under single-frequency excitation.

5.4.2 3D printing under variable-frequency excitation

AVC under variable-frequency sinusoidal excitation was simulated to further evaluate the adaptability of the feedforward FxLMS for vibration control under variations of operation conditions, causing a frequency shift in the vibration source. The disturbance shaker was initially driven by a 60 Hz sinusoidal signal with an amplitude of 0.15 V, which is close to the second mode of the system. At the midpoint of the printing process, the excitation frequency was switched to 50 Hz with the same amplitude and maintained until the completion of the process. The step size of the algorithm remains fixed at 5×10^{-9}, with all other controller parameters unchanged. Following the frequency change, the uncontrolled error signal is largely reduced, as shown in **Figure 5.10a**. The reduction occurs because the frequency response of the primary path is lower at 50 Hz than at 60 Hz. However, after the external vibration frequency shifts, a transient increase in the error signal is observed, which is attributed to the finite decay time of the structural response. Meanwhile, the controller output voltage decreases significantly after the frequency shift, as shown in **Figure 5.10b**. This is because the higher

frequency response of the secondary path at 50 Hz requires a lower control output before the shift. Simulation results show that the AVC implementation reduces the PSD of the error signal by 7.70 dB over the 16-minute printing duration. Specifically, the 50 Hz peak decreases by 8.15 dB, and the 60 Hz peak decreases by 9.91 dB compared to the scenario without AVC.

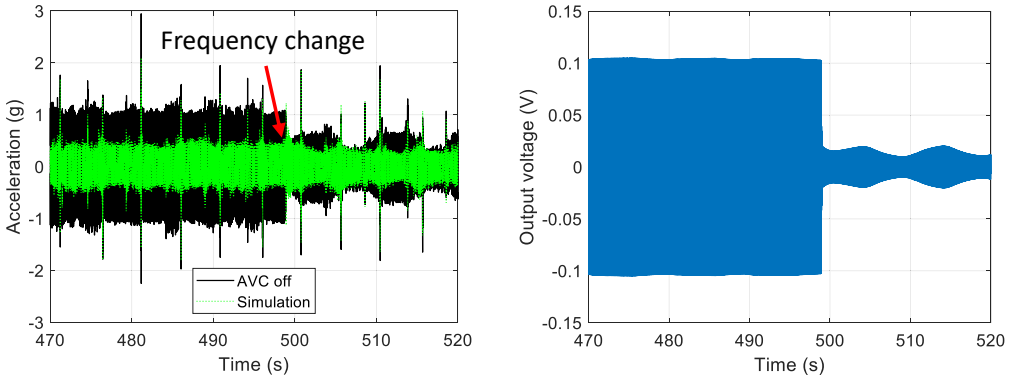

(a) (b)

Figure 5.10: (a) Comparison between simulation and no AVC of the error signals in time domain, and (b) controller output voltage under variable-frequency excitation.

5.4.3 3D printing under variable-amplitude excitation

Subsequently, a simulation of AVC under variable amplitude sinusoidal excitation was performed. Initially, the disturbance shaker was driven by a 60 Hz sinusoidal signal with an amplitude of 0.15 V. At the midpoint of the printing process, the amplitude of the signal was reduced to 0.1 V and maintained until the process completion. All the parameters of the controller remain the same. **Figure 5.11a** compares the time-domain error signals between the simulation and the AVC-off case. Following the reduction in external vibration amplitude, a transient increase in error signal magnitude is observed in simulations. However, after the control system adapts its output voltage to compensate for the modified vibration conditions, as shown in **Figure 5.11b**, the acceleration amplitude progressively decreases, demonstrating the controller's adaptive capability under time-varying disturbances. Simulation results show that the PSD of the error signal is reduced by 7.81 dB over the full printing duration,

and the 60 Hz peak is attenuated by 9.59 dB compared to the scenario without AVC.

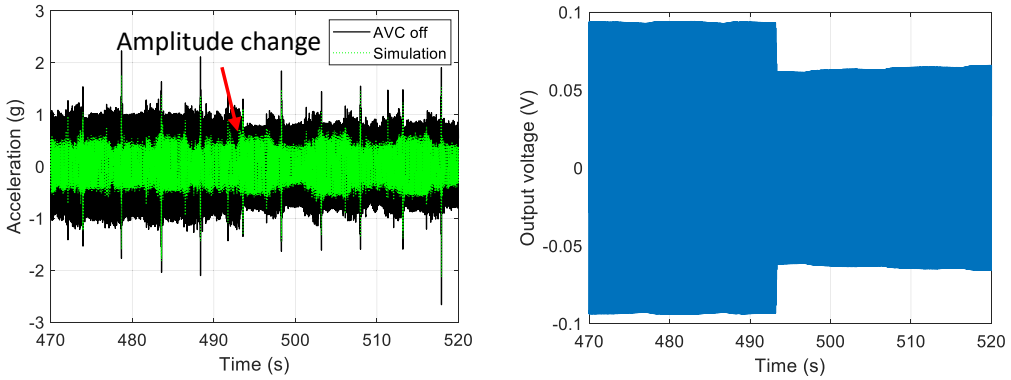

(a) (b)

Figure 5.11: (a) Comparison between simulation and no AVC of the error signals in time domain, and (b) controller output voltage under variable-amplitude excitation.

5.5 Experimental validation

This section verifies the performance of the feedforward FxLMS algorithm through similar experiments conducted in simulation. An overview of the 3D printer system setup under external vibration conditions is shown in **Figure 5.12**. To minimise external influences, the entire 3D printer was mounted on two aluminium extrusions, which are secured to a passive vibration isolation table. The disturbance shaker was mounted vertically on the vibration isolation table through an aluminium extrusion, while the control shaker was elevated using a metal block, which was also fixed to the isolation table. The reference accelerometer was located at the end of the disturbance shaker stinger. The error accelerometer was mounted at the top surface of the x-axis motor housing, while the monitor accelerometer was mounted on the top surface of the print head.

There are three AVC experiment scenarios, including single-frequency excitation, variable-frequency excitation, and variable amplitude excitation. For each test scenario, three groups of components are printed, including the benchmark (printing without external vibrations and control), AVC-off (printing with external vibrations but AVC is switched off), and AVC-on (printing

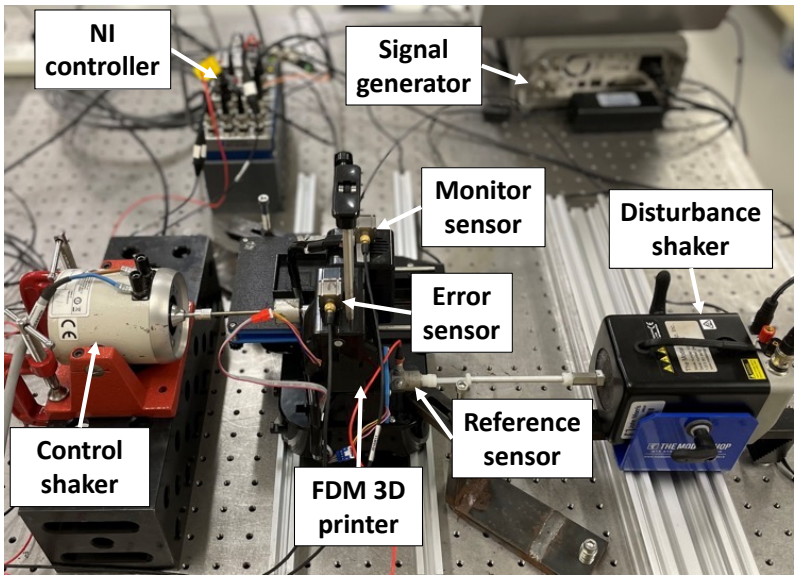

Figure 5.12: An overview of the 3D printer system experiment setup in this study.

with external vibrations and AVC is switched on), with three runs for each group. This leads to a total of 27 3D printed components in the AVC experiment. While the simulation focuses solely on y-axis error signal analysis due to the time-varying dynamic characteristics of the print head, the experimental study incorporates both error and monitor accelerometer signals to evaluate vibration levels in both the y and z-axis. These two axes exhibit strong coupling at the print head location due to the structural dynamics of the system.

5.5.1 AVC under single-frequency and amplitude excitation

In the first scenario, an AVC experiment was conducted under conditions similar to those in **Section 5.4.1**. Unlike the simulation case, the 52 Hz sinusoidal external vibration was applied during the filament preheating stage. The AVC system was activated beforehand, allowing the algorithm to converge prior to the start of the 3D printing process. The external force amplitude of the 52 Hz signal was measured around 0.34 N, while the external acceleration amplitude was around 3.38 g, both measured by the reference sensor.

A comparison of the PSD spectra for the error and monitor sensors in y

and z-axis is presented in **Figure 5.13**. Results indicate that better control performance is achieved at the error sensor location compared to the monitor sensor location, especially in y-axis. This aligns with our preliminary analysis in **Section 5.3.2**, as the print head exhibits time-varying characteristics during the printing process. Additionally, a peak is observed around 230 Hz in all four frequency spectra. This peak is attributed to vibrations generated by the cooling fan installed within the print head housing alongside the extruder, which cannot be controlled as the reference signal does not include this frequency component. Both axes achieve more than 10 dB reduction at 52 Hz peak, except for the y-axis of the monitor sensor, which achieves around 3 dB reduction at 52 Hz. The control performance of the AVC system, in terms of PSD reduction for the error and monitor sensors in all three axes is summarised in **Table 5.2**, with y- and z-axis achieving more than 1 dB overall PSD reduction. Although the overall PSD reduction in x-axis is lower than 1 dB at both sensor locations, the 52 Hz peak reduction is more than 10 dB. All the positive reduction values demonstrate the effectiveness of the algorithm. Compared to the simulation results, the experimental results demonstrate improved overall PSD reduction and greater attenuation at the 52 Hz peak.

Table 5.2: AVC performance of error and monitor sensor in three axes under single-frequency excitation.

Sensor type	Axis	Overall PSD reduction (dB)	52 Hz peak reduction (dB)
Error accelerometer	X-axis	0.84	11.88
	Y-axis	8.70	11.76
	Z-axis	1.79	11.08
Monitor accelerometer	X-axis	0.38	2.86
	Y-axis	1.62	3.01
	Z-axis	1.35	10.10

A time-domain comparison of the error signals of AVC-on in y-axis with benchmark and AVC-off results is shown in **Figure 5.14a**. A significant reduction in acceleration is achieved immediately after the start of printing. Only a short period of oscillation is observed around 10 seconds after the printing process begins. Notably, the experimental controller output voltage, depicted in **Figure 5.14b**, exhibits a higher amplitude compared to the simulation case, as shown in **Figure 5.9b**. This difference is likely due to the inaccuracy of

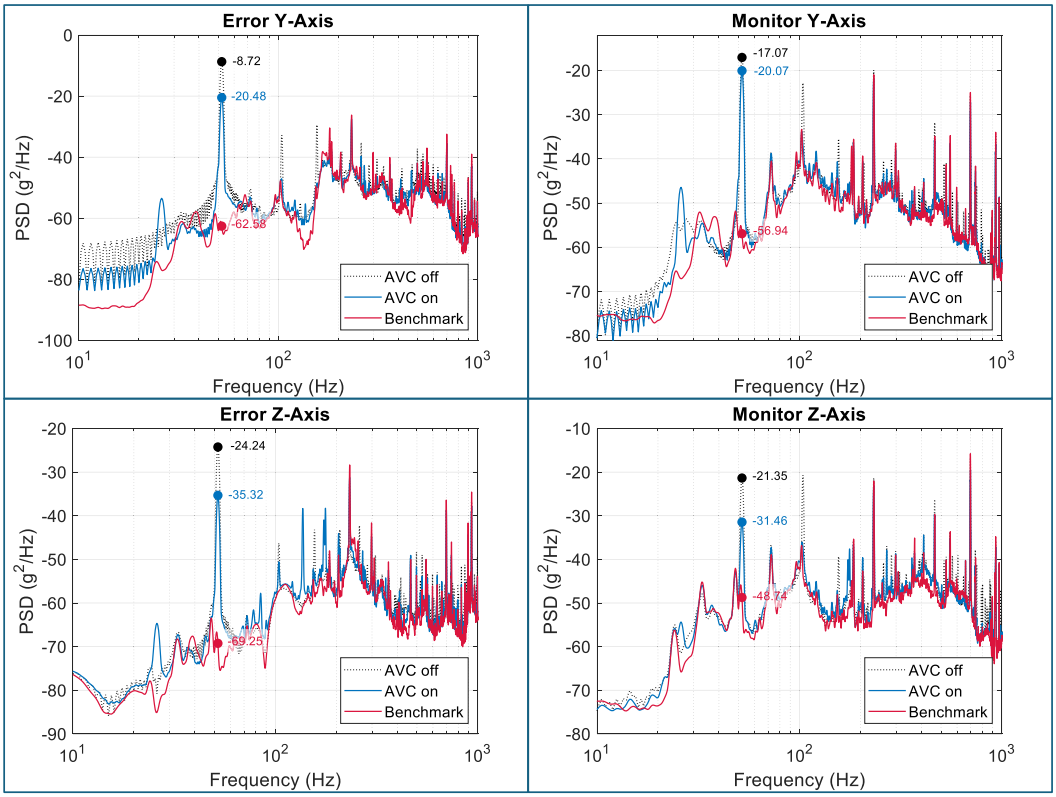

Figure 5.13: Comparison of AVC performance at the error sensor (first column) and monitor sensor (second column) for the y-axis (first row) and z-axis (second row) for AVC off, AVC on, and benchmark under single-frequency and amplitude excitation.

amplitude in secondary path modelling. The time-varying dynamics induced by print head motion and variations in the print head z-axis position during the printing process contribute to the error of the modelling.

5.5.2 AVC under variable-frequency excitation

In this section, the AVC performance under variable-frequency external vibration was experimentally investigated under conditions similar to those in **Section 5.4.2**. During the first half of the printing process, the external vibration frequency was set to 60 Hz, with an external force amplitude of approximately 0.34 N and an external acceleration amplitude of around 3.35 g. During the second half of the printing, the external vibration frequency was switched to 50 Hz, while the force amplitude remained unchanged, and the acceleration amplitude increased slightly to 3.42 g.

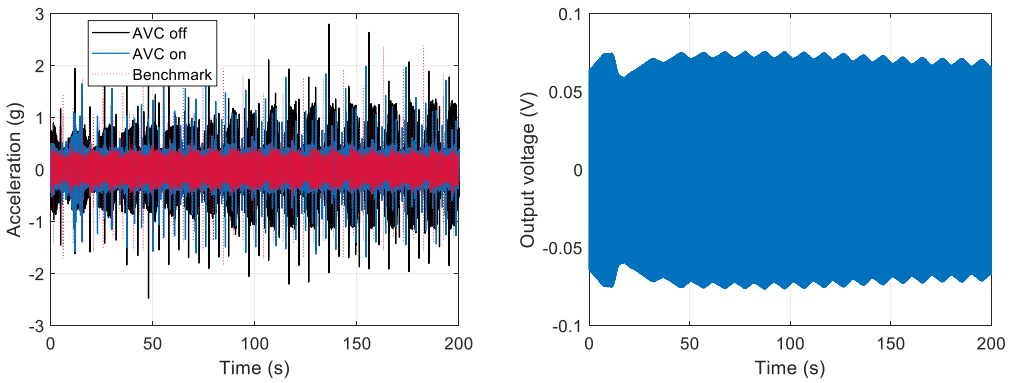

(a) (b)

Figure 5.14: (a) Time-domain error signal in y-axis, and (b) controller output voltage of the first 200 seconds.

A comparison of the PSD spectra for the error and monitor sensors in y- and z-axis is presented in Figure 53, showing a significant reduction in both axes. The peaks at 50 Hz and 60 Hz are reduced by more than 10 dB. While print head vibrations are better controlled at 60 Hz than at 50 Hz, both frequencies exhibit similar attenuation levels at the error sensor location. Notably, in the y-axis, the 50 Hz peak is only slightly reduced, as shown in the top-right corner of **Figure 5.15**. The control performance of the AVC system, in terms of PSD reduction for the error and monitor sensors in all three axes, is summarised in **Table 5.3**, with all axes achieving more than 1 dB overall PSD reduction except the print head vibration in z-axis. The 60 Hz peak is better controlled than the 50 Hz peak for both signals in all three axes. Compared to the simulation results, the experimental data demonstrate improved overall PSD reduction and greater attenuation at both frequency peaks.

A time-domain comparison of the error signals after AVC for benchmark and no AVC in y-axis during the frequency transition period is shown in **Figure 5.16a**. Initially, a high level of oscillation occurs as the controller continues to output a 60 Hz control signal before adapting to the 50 Hz external vibration, eventually reducing the overall vibration amplitude. Notably, the controller output voltage, depicted in **Figure 5.16b**, exhibits amplitude differences compared to the simulation case, especially with higher output voltage levels when the external vibration frequency is 50 Hz. This reveals the modelling errors between the modelled and the real experimental conditions.

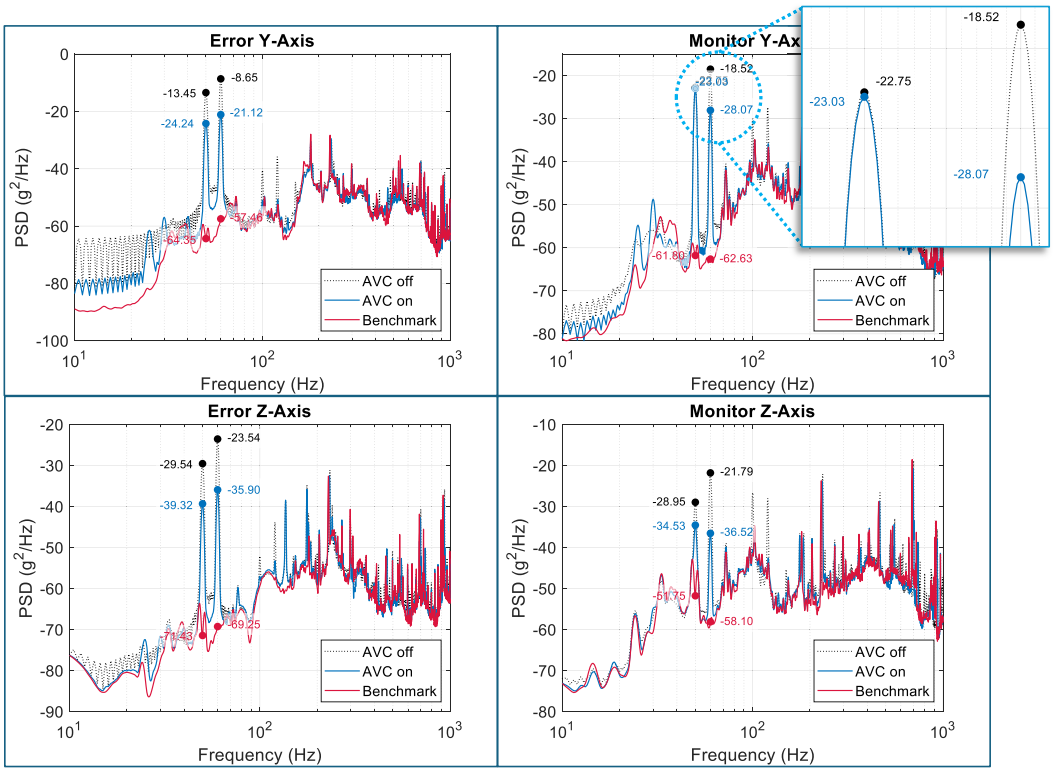

Figure 5.15: Comparison of AVC performance at the error sensor (first column) and monitor sensor (second column) for the y-axis (first row) and z-axis (second row) for AVC off, AVC on, and benchmark under variable-frequency excitation.

Table 5.3: AVC performance of error and monitor sensor in three axes under variable-frequency excitation.

Sensor type	**Axis**	**Overall PSD reduction (dB)**	**50 Hz peak reduction (dB)**	**60 Hz peak reduction (dB)**
Error accelerometer	X-axis	1.39	11.32	12.20
	Y-axis	9.19	10.79	12.47
	Z-axis	2.52	9.78	12.37
Monitor accelerometer	X-axis	1.01	2.51	10.14
	Y-axis	1.84	0.28	9.55
	Z-axis	0.81	5.57	14.73

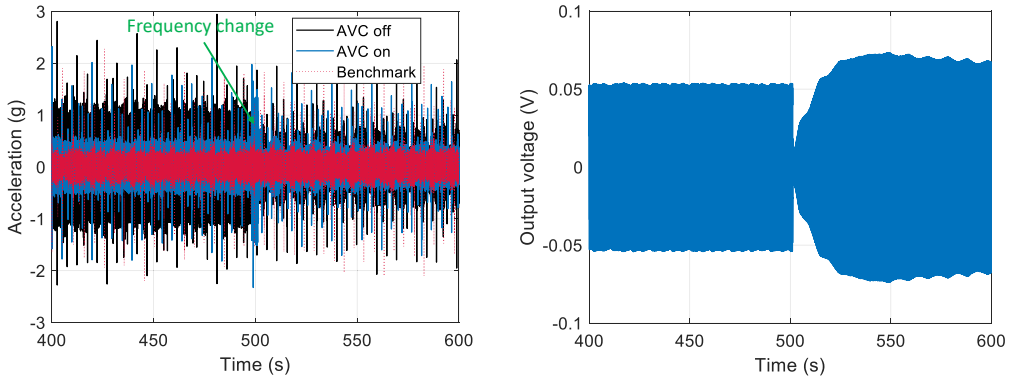

(a) (b)

Figure 5.16: (a) Time-domain error signal in y-axis, and (b) controller output voltage during the frequency transition period.

5.5.3 AVC under variable-amplitude excitation

Next, the AVC performance under variable-amplitude external vibration is evaluated. The external vibration was set at 60 Hz with amplitudes of 0.2 V and 0.15 V. All controller parameters remain consistent with those in **Section 5.4.3**. During the first half of the printing process, the external force amplitude was approximately 0.34 N, decreasing to 0.24 N in the second half. The acceleration amplitude decreases from around 3.38 g to 2.37 g.

A comparison of the PSD spectra is presented in **Figure 5.17**, showing that both axes achieve more than 1 dB overall PSD reduction and more than 8 dB reduction at the 60 Hz peak. The control performance of the AVC system, in terms of PSD reduction for the error and monitor sensors in all three axes, is summarised in **Table 5.4**, with all axes achieving more than 1 dB overall PSD reduction except the print head vibration in x-axis. In this scenario, experimental results closely align with simulation results in both the overall PSD and 60 Hz peak vibration reduction.

A time-domain comparison of the error signals after AVC for benchmark and no AVC results in y-axis during the amplitude transition period is shown in **Figure 5.18a**. A slight reduction in acceleration is observed immediately after the amplitude change, with the output voltage level adjusting proportionally to the acceleration variation. Notably, the experimental controller output voltage, depicted in **Figure 5.18b**, exhibits a lower amplitude compared to the simulation case, as shown in **Figure 5.11b**. This is also due to the inaccuracy

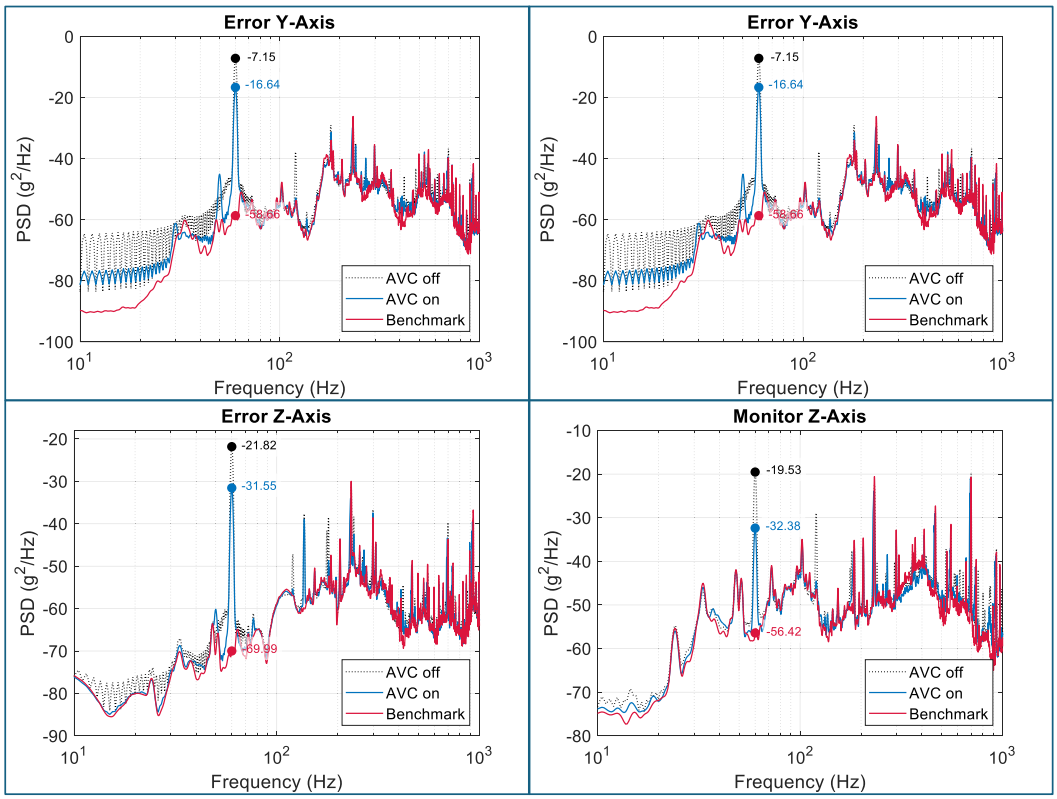

Figure 5.17: Comparison of AVC performance at the error sensor (first column) and monitor sensor (second column) for the y-axis (first row) and z-axis (second row) for AVC off, AVC on, and benchmark conditions under variable-amplitude excitation.

Table 5.4: AVC performance of error and monitor sensor in three axes under variable-amplitude excitation.

Sensor type	**Axis**	**Overall PSD reduction (dB)**	**60 Hz peak reduction (dB)**
Error accelerometer	X-axis	1.91	8.77
	Y-axis	7.88	9.49
	Z-axis	3.30	9.73
Monitor accelerometer	X-axis	0.88	7.07
	Y-axis	2.43	8.19
	Z-axis	1.02	12.85

of the secondary path modelling of amplitude at this frequency.

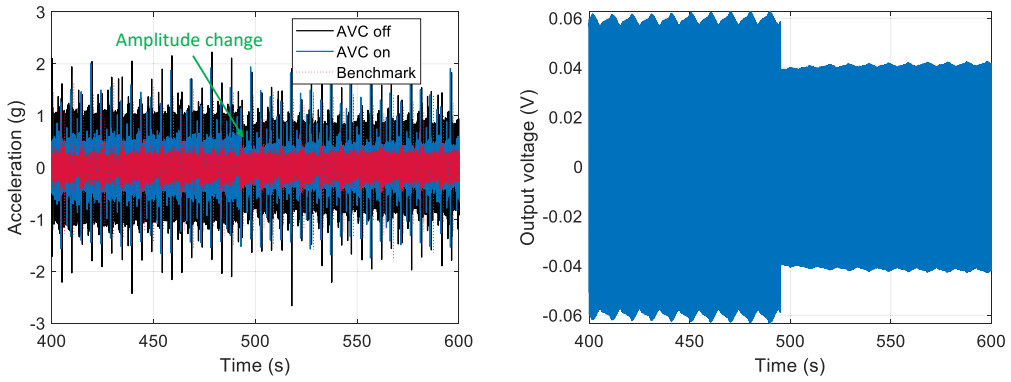

(a) (b)

Figure 5.18: (a) Time-domain error signal in y-axis, and (b) controller output voltage during the amplitude transition period.

5.6 Surface finish of 3D printed parts

The surface finish of 3D printed components is influenced by external vibrations, which show as surface roughness and surface waviness. These effects depend on the direction of vibrational disturbances relative to the build orientation. Surface roughness is defined as small-scale deviations in the out-of-plane direction, primarily induced by vibrations along the x- and y-axis. These vibrations lead to height variations on the printed surface. In contrast, surface waviness refers to larger scale deviations occurring in the in-plane direction and is primarily influenced by vibrations along the z-axis. These vibrations introduce periodic fluctuations in layer positioning during the printing process, resulting in wave-like patterns that extend over a broader spatial scale. The waviness of the surface can often be visually identified as a repetitive and fluctuating pattern.

Surface roughness, characterised by fine-scale height variations on a given surface, requires precise measurement techniques for quantitative evaluation. Standard roughness parameters, such as R_a (the arithmetic average of profile height deviations from the mean line) and R_q (the root mean square average of profile height deviations from the mean line), are commonly used to provide a standardised assessment of surface quality across different printed specimens.

To quantitatively assess the surface finish of all 27 3D printed components, surface roughness measurements were conducted using a digital microscope (Olympus DSX1000). A 20 times magnification was selected to provide a larger field of view, ensuring a broader measurement range for each sample. Due to the layer-by-layer nature of the printing process, individual layer textures significantly influence surface roughness measurements and may not accurately represent the impact of external vibrations on the overall surface finish. To minimise the effect of individual layers, surface roughness was measured in the horizontal direction, parallel to the layer orientation. The top photo in **Figure 5.19** shows a side face of three different 3D printed components from **Figure 5.8**, produced under the single-frequency excitation scenario, as per the annotations in the figure. Visible differences in surface roughness are observed, with the middle specimen exhibiting the roughest texture. Although the surface finish of the bottom specimen is not as smooth as the top one, it still demonstrates qualitative improvement when compared with the specimen printed with AVC off.

During the measurement process, the microscope captured a series of images at different focal planes using automated z-axis movement. The software analysed pixel sharpness across these planes to reconstruct a 3D height map of the surface. Then the captured image data was processed using the built-in Olympus Stream software to compute the roughness parameter, R_a, defined as the arithmetic mean of surface deviations along a profile. The image processing follows three main steps. First, the region of interest on the surface image is selected. Next, a Gaussian filter is applied, along with tilt correction and a noise removal procedure. Finally, surface roughness is measured based on the grey scale intensity at two horizontal reference lines, indicated in red and green. The R_a value is calculated as the average of these two measurements, taken at the same location on the sample side surface. An example of a 3D surface height map for a specimen printed without AVC is shown in the bottom right corner of **Figure 5.19**.

Figure 5.20 compares the images captured by the digital microscope, showing the differences in surface quality across different samples. It can be observed that wave-like patterns appear on the AVC-off sample, indicating periodic deviations in layer deposition. Additionally, voids are present between some layers, which are attributed to layer delamination. These surface irregu-

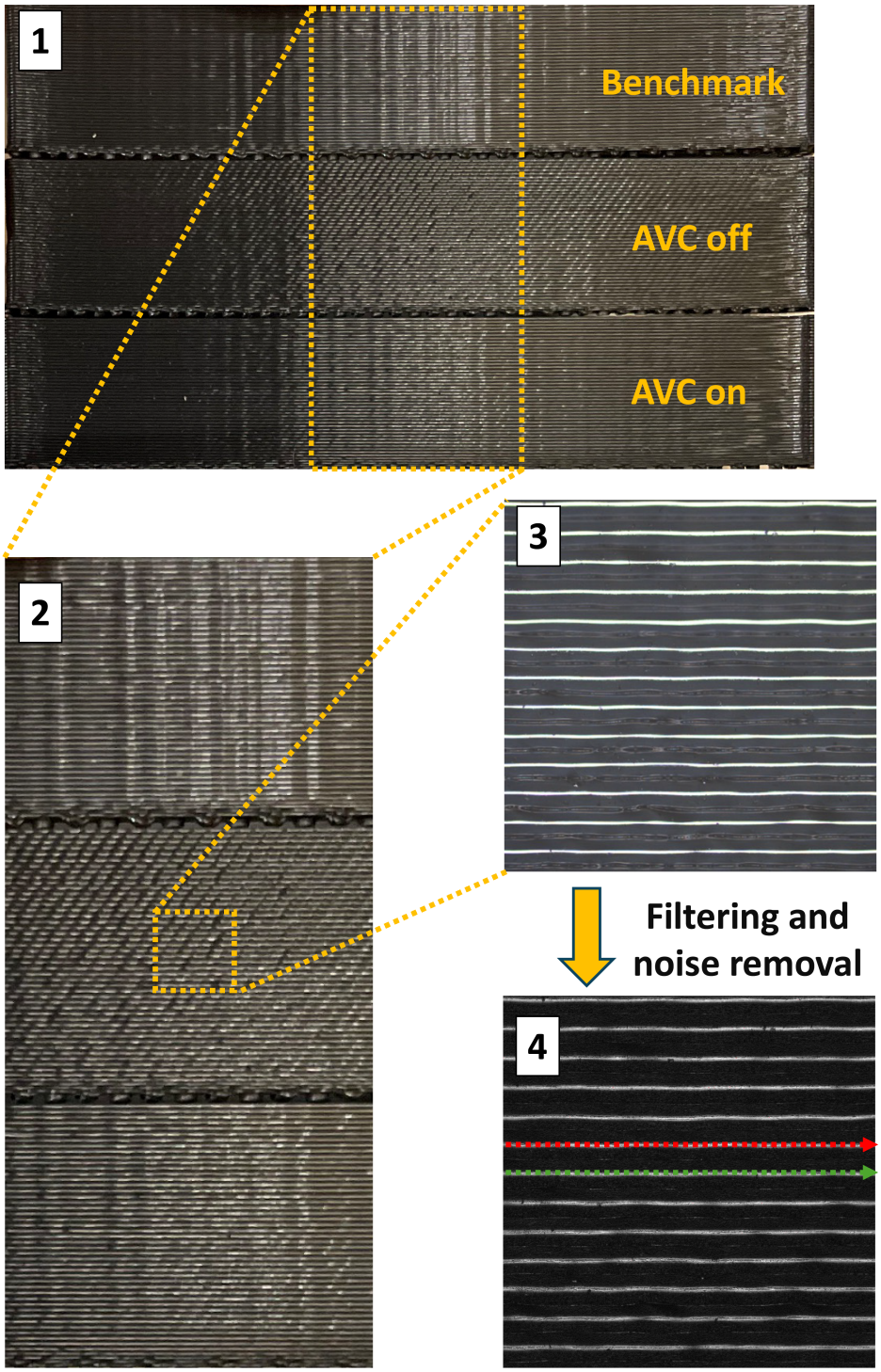

Figure 5.19: 1: Photo of the surface finish of benchmark, AVC-off, and AVC-on specimens. 2: Field of view of the AVC-off specimen using a microscope. 3: Raw image of the measurement area (20 × magnification). 4: Filtered and pre-processed 3D height map (20× magnification).

larities result from deviations in the print path vertically caused by vibrations in z-axis, which disrupt the uniform deposition of material during the printing process.

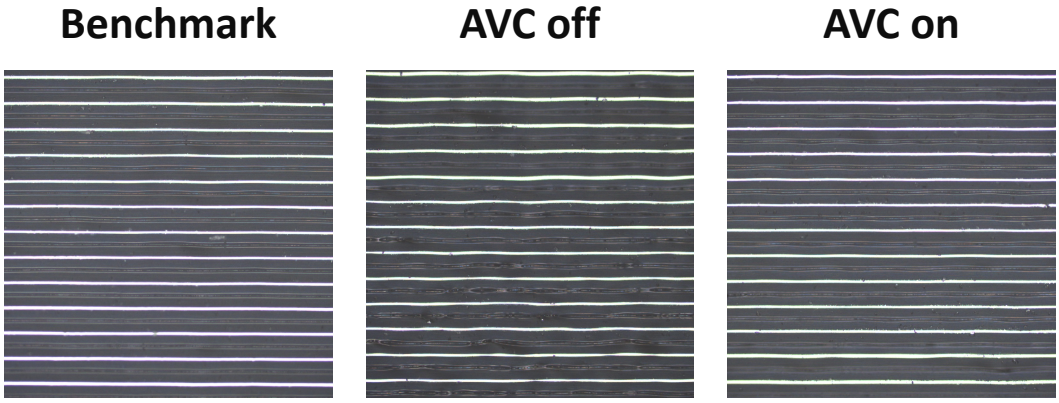

Figure 5.20: The surface quality comparison between a benchmark, AVC-off, and AVC-on specimen (20× magnification).

The surface roughness R_a values for all 27 printed components, measured in micrometre, are summarised in **Table 5.5**. The highest improvement in surface roughness is observed in the AVC with single-frequency excitation scenario, achieving an average improvement of over 30%. The lowest improvement is recorded in the AVC with variable-frequency excitation scenario, with an average improvement of over 20%. Overall, the effectiveness of the FxLMS algorithm in AVC for 3D printing under external vibration conditions is demonstrated by the enhanced surface quality of the printed components.

Table 5.5: A comparison of surface roughness (R_a) with and without AVC under different vibration excitations.

External vibration type	**AVC off** (μm)	**AVC on** (μm)	**Improvement percentage**
Single-frequency and amplitude	7.078	4.909	30.64%
Variable-frequency	6.906	5.335	22.74%
Variable-amplitude	7.187	5.161	28.19%
No vibration benchmark	4.491 — No AVC applied (reference case)		

5.7 Summary

This study demonstrates a feedforward FxLMS AVC system applied to a compact multi-axis positioning platform representative of a desktop-scale FFF 3D printer operating under dynamic environmental conditions. The study first identified and modelled the dominant vibration transmission paths by selecting error and sensor locations that yield a nearly time-invariant secondary path during printing. This configuration enabled practical and stable controller operation despite variations in the print head dynamics.

Controller performance was evaluated in simulation and experiment under single-frequency, variable-frequency, and variable-amplitude excitation scenarios. Across scenarios, the FxLMS controller achieved consistent reductions in vibration energy at the error and monitor locations, with overall PSD reductions exceeding 1.6 dB and peak attenuation above 10 dB at targeted frequencies. Differences between simulated and experimental performance are due to modelling error in the secondary-path amplitude and time-varying dynamics at the moving print head, which are largely mitigated by the chosen sensor placement.

The surface quality of the printed components was used as a secondary validation of vibration suppression of the AVC system. Surface roughness measurements across 27 specimens showed average improvements above 20%, with a maximum improvement above 30% in the single-frequency case. These results demonstrate that reducing structural vibration in the positioning systems translates to improved printed outcomes.

The laboratory actuator was an electrodynamic shaker, chosen for its ability to deliver high-amplitude low-frequency control forces. This hardware is not intended for embedded use. Practical deployment requires compact actuators that are collocated with structural elements and offer sufficient bandwidth. As demonstrated in **Chapter 4**, piezoelectric actuators offer high bandwidth, rapid dynamic response, and enable seamless integration into structural components such as gantries or motor mounts via a customised bracket. Future work should focus on embedded implementation and broader operating conditions of the proposed approach. These include integration of the AVC system with compact actuators, evaluation under broadband and multi-axis excitations, and online adaptation of secondary path estimates to

manage time-varying dynamics.

Additionally, extending the approach to other positioning architectures could help to generalise the applicability and robustness of the proposed AVC system in more diverse and practical manufacturing scenarios. Delta mechanisms positioning platform - with their parallel kinematic configurations - and robotic arm-based systems - with extended degrees of freedom and higher structural flexibility - present distinct dynamic profiles that may affect vibration transmission and control performance. Additional studies varying motion profiles, speeds, and part trajectories will stress the control system under richer dynamic regimes and help to quantify the limits of the single-model secondary-path assumptions.

CHAPTER 6

Conclusions and future work

6.1 Conclusions

This thesis addressed the critical challenge of maintaining print quality and structural integrity in fused filament fabrication (FFF) processes conducted in dynamic, vibration-prone environments. Motivated by the increasing adoption of additive manufacturing (AM) in mobile and onsite fabrication contexts, such as transportation-based systems, this work established a comprehensive framework to characterise the effects of environmental vibration on 3D printed structures and to develop active vibration control strategies to mitigate these effects during fabrication.

The first part of the research (**Chapter 2** and **Chapter 3**) examined how different infill designs and environmental vibrations affect the dynamic properties and surface quality of printed components. Infill pattern and infill density differences were found to change the stiffness-to-mass ratio and damping behaviour of the printed structures. Among the explored patterns, the gyroid infill at 40% density showed the highest natural frequency, while lower infill densities produced higher damping. Clamping forces also influenced the measured natural frequencies, meaning that fixture stiffness must be considered when assessing printed components.

When printing under controlled external vibration profiles, the response of the printer structure depended strongly on the frequency content of vi-

brations. Low-frequency excitation caused larger surface roughness, while mid-frequency, harmonic conditions generated internal defects that lowered the stiffness and natural frequencies of printed components. These observations show that identical overall vibration energy can produce different forms of quality degradation, depending on how it interacts with the system's structural modes.

The second part (**Chapter 4** and **Chapter 5**) developed and validated active vibration control (AVC) approaches for moving stage systems and small-scale FFF printers. In the moving stage platform, an adaptive affine projection algorithm with online switching of positionally dependent models reduced dominant resonances by around 4 dB, showing that adaptive control can stabilise systems whose dynamics change with position. Extending this to an FFF printer, the feedforward filtered-x least mean squared (FxLMS) control system reduced measured vibration on the printer structure, and improved surface quality of printed components by more than 20% on average. This demonstrates that active control approach can mitigate environmental disturbances in small-scale FFF printers.

Beyond the quantitative outcomes, this research offers new insight into the interaction between vibration spectra and the structural dynamics of FFF systems. The adaptive control framework developed here provides a flexible and reliable alternative to conventional passive vibration suppression, maintaining print consistency even when operating conditions change during fabrication.

Overall, the work redefines vibration control in FFF as a problem of adaptability rather than rigidity. High-quality fabrication in dynamic environments can be achieved through active and adaptive control rather than static structural modifications alone. The framework established here linking modal characterisation, environmental vibration testing, and adaptive control, provides a foundation for control system design of 3D printers and other motion systems that combine responsiveness with precision.

6.2 Future work

The methodology and results presented in this thesis form a basis for dynamic characterising and mitigating the effects of vibration on FFF. Several directions

can extend and deepen the findings.

The experimental study in **Chapter 2** considered a limited range of infill-related process parameters. Future research could explore how internal structure influences modal and damping properties in more complex geometries. A broader range of standardised specimens with different process parameters could account for the imperfections, such as voids and weak layer bonding.

In **Chapter 3**, the surface roughness analysis was conducted on 3D printed structures with a specific geometry. Future studies could expand this to include a variety of geometries. Furthermore, applying advanced microscopy techniques would enable detailed examination of the internal microstructure of the printed parts fabricated under different vibration conditions. This would provide deeper insights into how vibration frequency content influences the internal microstructure of printed structures.

The moving stage system described in **Chapter 4** was evaluated at a constant operating speed. Testing under variable trajectories and accelerations would show how adaptive algorithms handle rapidly changing dynamics. Hybrid schemes combining feedback and feedforward approaches may further improve stability without increasing much computational load.

Chapter 5 investigated vibration control of the FFF system under narrowband excitation, which does not reflect the real-world vibration conditions specified in **Chapter 3**. The next step should incorporate different broadband vibration profiles to more accurately simulate real-world disturbances and evaluate the effectiveness of the control algorithm under more dynamic and challenging conditions.

APPENDIX A

Supplementary theoretical and experimental analysis

This appendix provides supplementary materials related to the theoretical calculation of natural frequencies of the beam and additional experimental investigations on boundary conditions presented in **Chapter 2**, as well as a detailed description of the shaker fixture used in **Chapter 3**.

A.1 Vibration of beam structures

Slender beams are the focus in this study due to their widespread applications in engineering structures. When a slender beam oscillates in a direction perpendicular to its longitudinal axis, the primary mode of deformation is bending. This type of vibration is referred to as transverse or lateral vibration. The response of the beam under transverse vibration can be described as follows [43, 117]:

$$\frac{d^2}{dx^2}\left(EI\frac{d^2w(x,t)}{dx^2}\right)+m\frac{d^2w(x,t)}{dt^2}=0 \tag{A.1}$$

where E is Young's modulus, I is the cross-sectional moment of inertia of the beam, m is the mass per unit length, and $w(x,t)$ represents the lateral displacement of the beam at position x and time t. Considering the beam is uniform, the equation can be rewritten as:

$$\frac{d^4w(x,t)}{dx^4}+\frac{m}{EI}\frac{d^2w(x,t)}{dt^2}=0 \tag{A.2}$$

This governing equation is known as the Euler-Lagrange equation, which forms the foundation of Euler-Bernoulli beam theory or classical beam theory. The theory makes several key assumptions: plane sections remain plane and perpendicular to the neutral axis before and after deformation, shear deformation and rotational inertia effects are negligible, the material of the beam is homogeneous, and the beam undergoes only small deflection angles. According to modal analysis, the displacement of the beam can be separated in space and time:

$$w(x,t) = \Phi(x)\eta(t) \tag{A.3}$$

where $\Phi(x)$ is the mode shape function, $\eta(t)$ is the modal coordinate. Substitute the equation back into the former equation and separate variables for time and space, and two ordinary differential equations can be obtained:

$$\frac{d^4\Phi(x)}{dx^4} - \frac{m\omega^2}{EI}\Phi(x) = 0 \tag{A.4}$$

$$\frac{d^2\eta(t)}{dt^2} + \omega^2\eta(t) = 0 \tag{A.5}$$

where ω represents the natural angular frequency of the beam vibration. To solve the spatial equation, a general solution is given:

$$\Phi(x) = A_1 cosh(\beta x) + A_2 sinh(\beta x) + A_3 cos(\beta x) + A_4 sin(\beta x) \tag{A.6}$$

where $\beta = \left(\frac{m\omega^2}{EI}\right)^{\frac{1}{4}}$, A_1, A_2, A_3, A_4 are constants. For the fixed-free boundary condition of a cantilevered beam of length L shown in **Figure A.1**, non-trivial solutions are found to exist when:

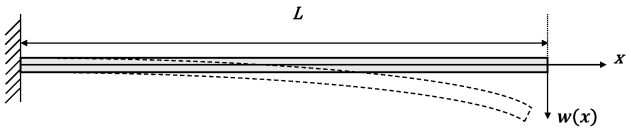

Figure A.1: Schematic diagram of a vibrating cantilever beam.

$$cosh(\beta_n L)\, cos(\beta_n L) + 1 = 0 \tag{A.7}$$

and the first three roots are approximately $\beta_1 L = 1.875, \beta_2 L = 4.694, \beta_3 L = 7.855$. Then substitute them back to $\beta = \left(\frac{m\omega^2}{EI}\right)^{\frac{1}{4}}$, the angular natural frequencies ω_n can be calculated using:

$$\omega_n = {\beta_n}^2 \sqrt{\frac{EI}{m}} \tag{A.8}$$

and the natural frequencies are:

$$f_n = \frac{k_n}{2\pi}\sqrt{\frac{EI}{mL^4}} \tag{A.9}$$

where $k_1 = 1.875^2, k_2 = 4.694^2, k_3 = 7.855^2$ for the first three natural frequencies, respectively.

This means that if the material properties and the geometry of a beam are known, its modal properties can be calculated. This is typically the case for homogeneous materials. However, in AM, 3D printed samples often exhibit non-homogeneous characteristics due to factors such as raster angle and wall structures. Consequently, the material properties cannot be directly applied to the above equation. In such cases, the effective elastic modulus is used to accurately assess the modal properties of the printed structure.

A.2 Effects of boundary conditions on natural frequencies

A more comprehensive assessment of the validity of the modal characteristics observed under the nominal experimental conditions was achieved by introducing three additional levels of clamping force, lower than the initial 320 N. By investigating how these variations affect the measured natural frequencies, the study aimed to quantify and understand the uncertainty introduced by potential variations in boundary conditions. The all four clamping force levels are 70 N, 160 N, 250 N and 320 N. Comparisons of the first three natural frequencies under different clamping forces are presented in **Figure A.2**, where a clear upward trend is observed as the clamping force increases, especially for infill percentages of 40% and higher.

The FRFs of the specimens under different clamping forces are compared and presented in **Figure A.3**. It is observed that a higher level of clamping force leads to higher natural frequencies, especially for 70% and 100% infill specimens, where all three natural frequencies shift to higher values when the 320 N clamping force is applied. This might be because the higher clamping force could potentially improve the stiffness of the test specimen, which improves the effective elastic modulus and thus shifts the natural frequencies to higher values. In contrast, the 10% and 40% infill specimens exhibit a

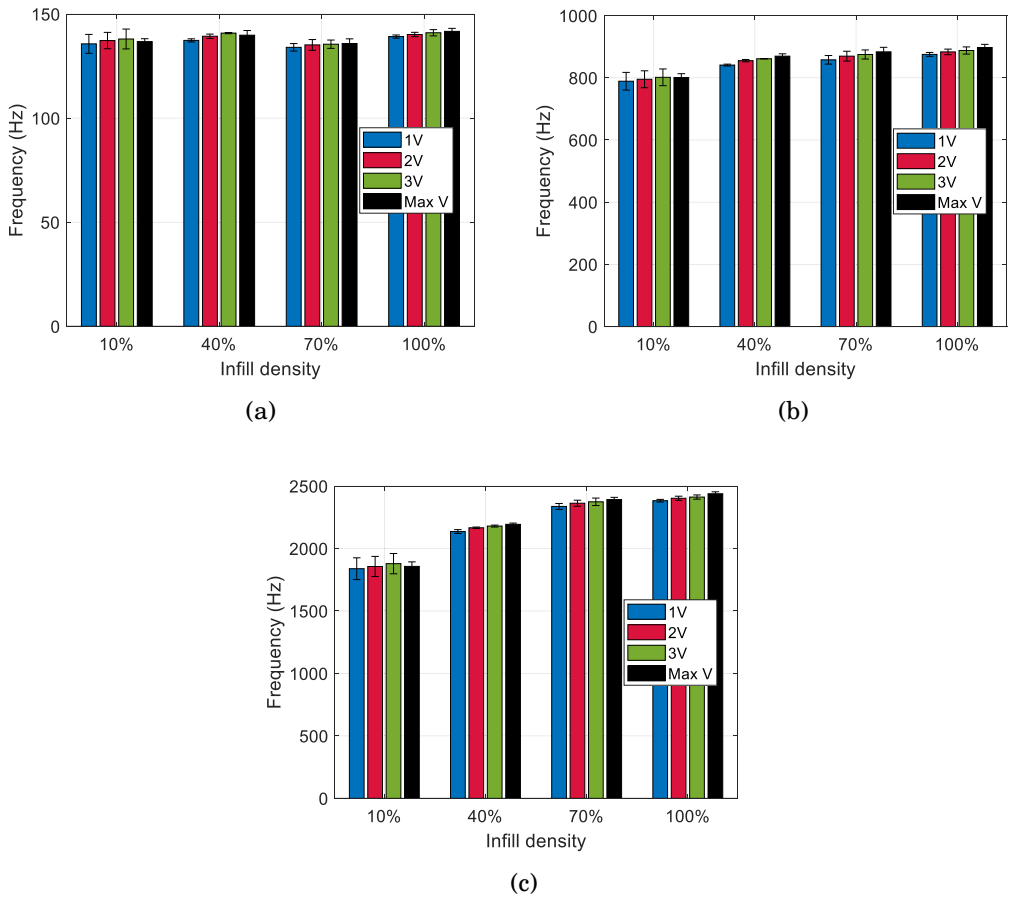

Figure A.2: The averaged experimental (a) first, (b) second, and (c) natural frequencies of specimens under different levels of clamping forces.

relatively low third natural frequency magnitude, and the clamping force has less influence on the natural frequencies. In **Figure A.3a** and **A.3b**, the phase response does not cross zero at the third natural frequency under most of the clamping forces, and the peak in the magnitude response appears smooth. In **Figure A.3c** and **A.3d**, a gradual phase transition is observed at the third natural frequency, while at the first and the second natural frequencies, a steeper phase transition is found. These findings suggest a lightly damped third natural frequency for these low infill density specimens, which has been confirmed by the system damping ratio calculations presented in **Table 2.7** in the previous section.

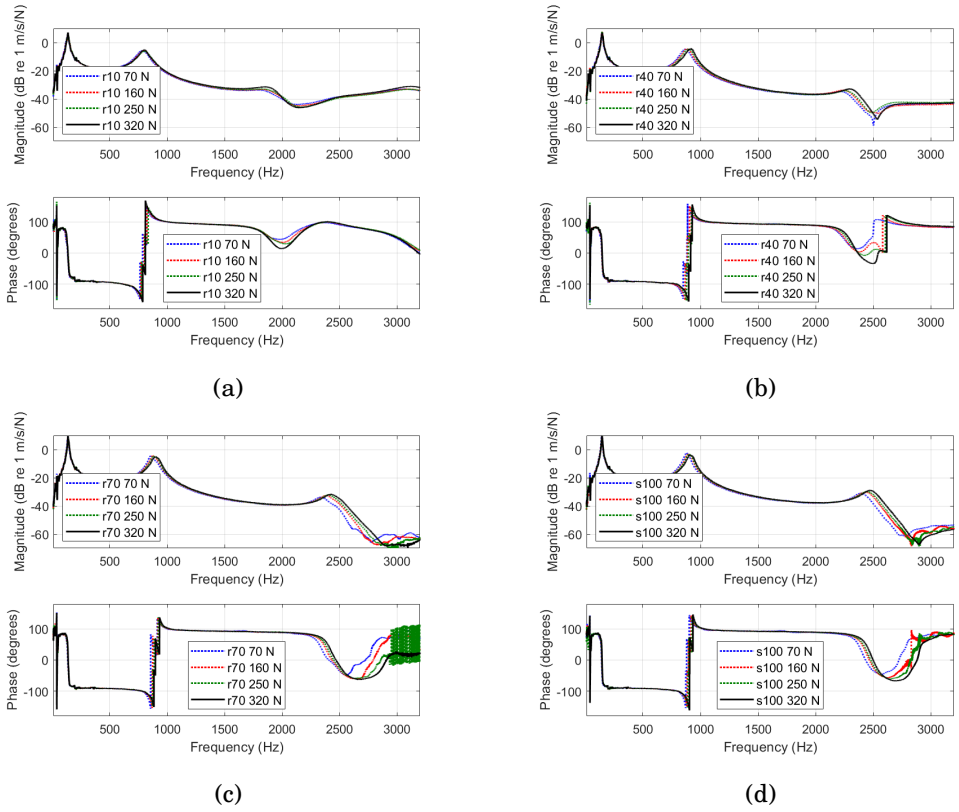

Figure A.3: FRF of different specimens under variable clamping forces shown in magnitude (left column) and phase (right column). (a) 10% infill, (b) 40% infill, (c) 70% infill, and (d) 100% infill specimens.

A.3 Customised shaker fixture

The fixture functions as a mechanical adapter structure, mounted on top of the vibration shaker to increase the mounting surface area, thereby accommodating larger components. Additionally, it also facilitates even transmission of vibrational energy to the test object and enables testing of objects that cannot be directly mounted to the shaker armature. The fixture was machined from a 300 mm by 300 mm square-shaped block of 6061 aluminium alloy. To enhance the structural rigidity of the fixture, multiple ribs are designed to attach at the bottom of the fixture surface. This fixture incorporates thirty-six M6 threaded mounting holes arranged in a 6×6 grid with a 50 mm pitch. Additionally, it includes five M5 socket cap head screw holes on a 50 mm pitch circle diameter to secure the fixture centrally to the shaker armature using M5 $\times$ 40 mm stainless steel socket cap head screws. The complete design of the fixture is shown in **Figure A.4**. The fixture has a total height of 60 mm,

weighs approximately 3.35 kg, and has its centre of mass at x = y = 0.15 m, and z = 0.012 m. When mounted on the armature of the shaker, the fixture exhibits a first natural frequency of around 1.7 kHz, as illustrated in the FRF of the fixture in **Figure A.5**. This frequency is sufficiently higher than the predominant excitation frequency range used in this study, which ensures the fixture resonance does not interfere with the test results. A low-frequency resonance of the shaker structure is observed at 12.5 Hz, while its magnitude is 18 times lower than that of the fixture resonance, and therefore does not have a major influence on the experiment.

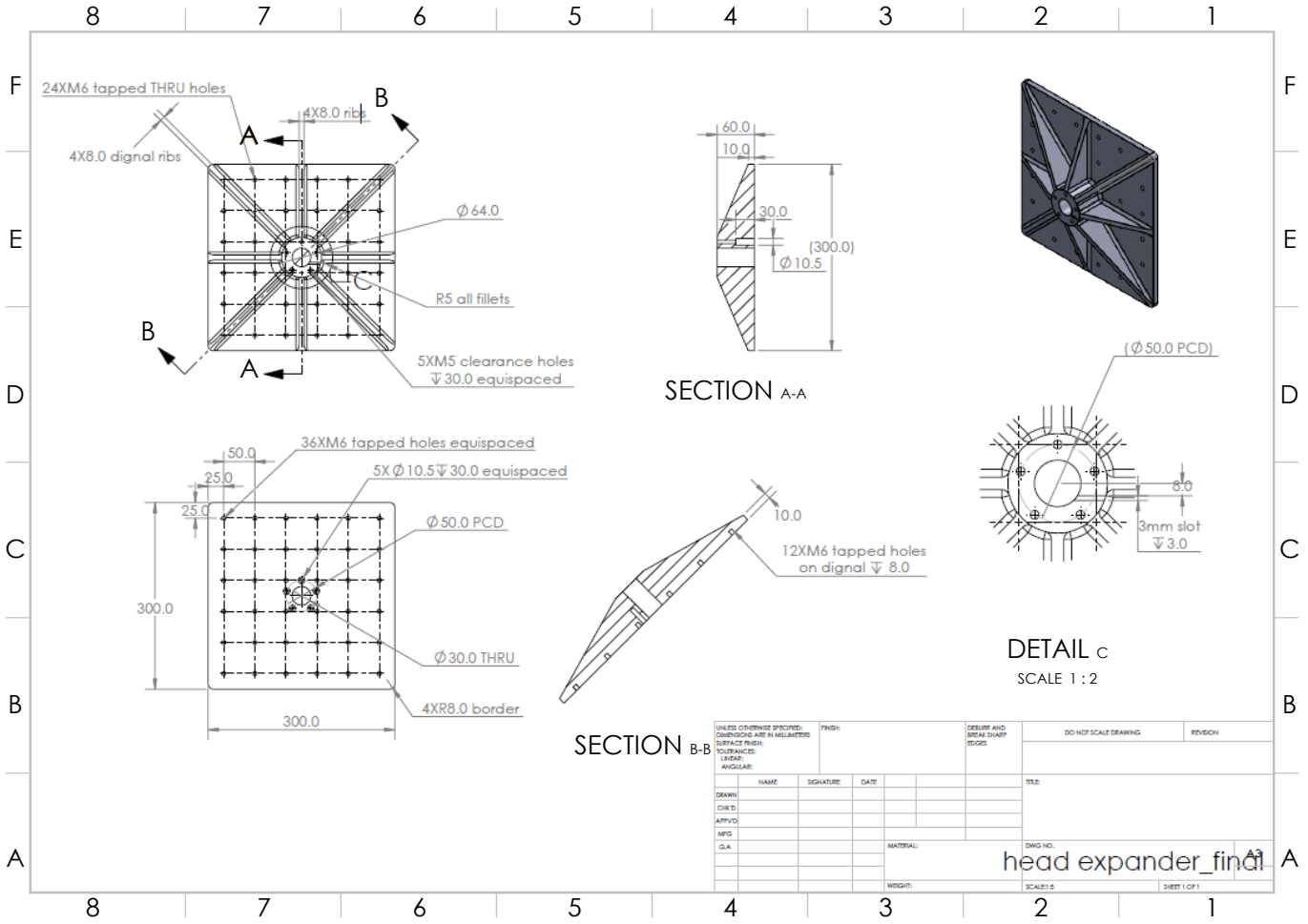

Figure A.4: Dimensions of the customised head expander.

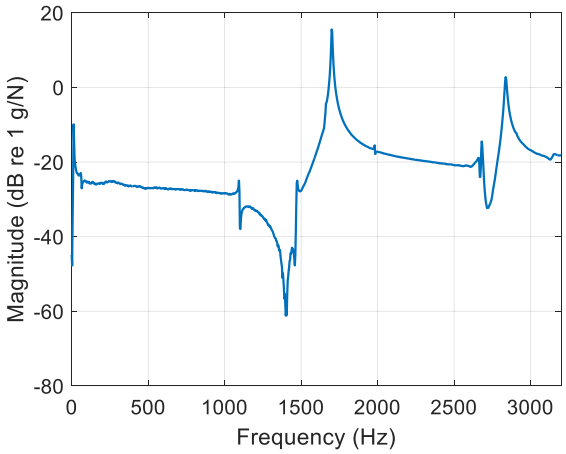

Figure A.5: FRF of the fixture.

Bibliography

[1] OpenAI. Chatgpt. https://chatgpt.com/. Accessed: October 27, 2025.

[2] C. Hull. Apparatus for production of three dimensional objects by stereolithography. Technical report, 1986.

[3] T. D. Ngo, A. Kashani, G. Imbalzano, K. T. Q. Nguyen, and D. Hui. Additive manufacturing (3d printing): A review of materials, methods, applications and challenges. *Composites Part B: Engineering*, 143:172–196, 2018.

[4] Research and Markets. Additive manufacturing market to surge, projections estimate robust growth with us$ 31 billion valuation by end of 2024. https://www.globenewswire.com/news-release/2024/01/29/2819340/28124/en/Additive-Manufacturing-Market-to-Surge-Projections-Estimate-Robust-Growth-with-US-31-Billion-Valuation-by-End-of-2024.html. Accessed: October 24, 2025.

[5] V. Mazzanti, L. Malagutti, and F. Mollica. Fdm 3d printing of polymers containing natural fillers: A review of their mechanical properties. *Polymers*, page 1094, 2019.

[6] K. V. Wong and A. Hernandez. A review of additive manufacturing. *ISRN Mechanical Engineering*, 2012:1–10, 2012.

[7] Additive manufacturing — general principles — fundamentals and vocabulary (iso/astm 52900:2021). Technical report, ISO, ASTM, 2021.

[8] A. Haghighi and L. Li. Study of the relationship between dimensional performance and manufacturing cost in fused deposition modeling. *Rapid Prototyping Journal*, 24:395–408, 2018.

[9] J. Shah, B. Snider, T. Clarke, S. Kozutsky, M. Lacki, and A. Hosseini. Large-scale 3d printers for additive manufacturing: design considerations and challenges. *International Journal of Advanced Manufacturing Technology*, 104:3679–3693, 2019.

[10] Z. Huang, J. Y. Dantan, A. Etienne, M. Rivette, and N. Bonnet. Geometrical deviation identification and prediction method for additive manufacturing. *Rapid Prototyping Journal*, 24:1524–1538, 2018.

[11] I. Gibson, D. Rosen, and B. Stucker. Development of additive manufacturing technology. In *Additive Manufacturing Technologies*, pages 19–42. Springer New York, 2015.

[12] S. A. Khairallah, A. T. Anderson, A. Rubenchik, and W. E. King. Laser powder-bed fusion additive manufacturing: Physics of complex melt flow and formation mechanisms of pores, spatter, and denudation zones. *Acta Materialia*, 108:36–45, 2016.

[13] F. Honarvar and A. Varvani-Farahani. A review of ultrasonic testing applications in additive manufacturing: Defect evaluation, material characterization, and process control. *Ultrasonics*, 108:106227, 2020.

[14] H. Kim, Y. Lin, and T. L. B. Tseng. A review on quality control in additive manufacturing. *Rapid Prototyping Journal*, 24:645–669, 2018.

[15] Creality. Creality official website. `https://www.creality.com/`. Accessed: October 10, 2025.

[16] Ultimaker. Ultimaker official website. `https://ultimaker.com/`. Accessed: October 10, 2025.

[17] D. Popescu, A. Zapciu, C. Amza, F. Baciu, and R. Marinescu. Fdm process parameters influence over the mechanical properties of polymer specimens: A review. *Polymer Testing*, 69:157–166, 2018.

[18] J. Torres, J. Cotelo, J. Karl, and A. P. Gordon. Mechanical property optimization of fdm pla in shear with multiple objectives. *JOM*, 67:1183–1193, 2015.

[19] R. B. S. Gowda, C. S. Udayagiri, and D. D. Narendra. Studies on the process parameters of rapid prototyping technique (stereolithography) for the betterment of part quality. *International Journal of Manufacturing Engineering*, 2014:1–11, 2014.

[20] X. Liu, M. Zhang, S. Li, L. Si, J. Peng, and Y. Hu. Mechanical property parametric appraisal of fused deposition modeling parts based on the gray taguchi method. *International Journal of Advanced Manufacturing Technology*, 89:2387–2397, 2017.

[21] Additive manufacturing — general principles — main characteristics and corresponding test methods. Technical report, ISO/ASTM, 2024.

[22] J. M. Chacón, M. A. Caminero, P. J. Núñez, E. García-Plaza, I. García-Moreno, and J. M. Reverte. Additive manufacturing of continuous fibre reinforced thermoplastic composites using fused deposition modelling: Effect of process parameters on mechanical properties. *Composites Science and Technology*, 181:107688, 2019.

[23] T. Hofstätter, D. B. Pedersen, G. Tosello, and H. N. Hansen. State-of-the-art of fiber-reinforced polymers in additive manufacturing technologies. *Journal of Reinforced Plastics and Composites*, 36:1061–1073, 2017.

[24] V. K. Balla, K. H. Kate, J. Satyavolu, P. Singh, and J. G. D. Tadimeti. Additive manufacturing of natural fiber reinforced polymer composites: Processing and prospects. *Composites Part B: Engineering*, 174:106956, 2019.

[25] Z. Pilch, J. Domin, and A. Szlapa. The impact of vibration of the 3d printer table on the quality of print. In *2015 Selected Problems of Electrical Engineering and Electronics, WZEE 2015*, pages 1–6. Institute of Electrical and Electronics Engineers Inc., 2015.

[26] A. Boschetto, V. Giordano, and F. Veniali. 3d roughness profile model in fused deposition modelling. *Rapid Prototyping Journal*, 19:240–252, 2013.

[27] J. B. Deb, S. Chowdhury, S. Chowdhury, G. Paul, T. Pal, J. Deb, and S. Deb. Machine acceleration time series prediction for dimensional

accuracy of 3d printed parts. *Data Science and Management*, 7:218–227, 2024.

[28] SimplyPrint. 3d printing: Missing layers and how to avoid them. `https://simplyprint.io/print-troubleshoot/missing-layers`. Accessed: October 24, 2025.

[29] D. Zhang, Z. Li, S. Qin, and S. Han. Optimization of vibration characteristics of fused deposition modeling color 3d printer based on modal and power spectrum method. *Applied Sciences*, 9:4154, 2019.

[30] G. S. Dos Ribeiro and Z. C. Silveira. Structural and modal analysis of a desktop 3-d printer considering an interchangeable mini screw extrusion head. In *High Value Manufacturing: Advanced Research in Virtual and Rapid Prototyping*, pages 525–530, 2014.

[31] P. Minetola and M. Galati. A challenge for enhancing the dimensional accuracy of a low-cost 3d printer by means of self-replicated parts. *Additive Manufacturing*, 22:256–264, 2018.

[32] Maharshi A. Sharma and Albert E. Patterson. Passive vibration control of a 3-d printer gantry. *arXiv preprint arXiv:2505.19311*, 2025.

[33] M. Duan, D. Yoon, and C. E. Okwudire. A limited-preview filtered b-spline approach to tracking control – with application to vibration-induced error compensation of a 3d printer. *Mechatronics*, 56:287–296, 2018.

[34] N. Edoimioya, C. H. Chou, and C. E. Okwudire. Vibration compensation of delta 3d printer with position-varying dynamics using filtered b-splines. *International Journal of Advanced Manufacturing Technology*, 125:2851–2868, 2023.

[35] N. Edoimioya, K.S. Ramani, and C.E. Okwudire. Software compensation of undesirable racking motion of h-frame 3d printers using filtered b-splines. *Additive Manufacturing*, 47:102290, 2021.

[36] L. K. Apsley, C. I. Bodell, J. C. Danton, S. R. Hayden, S. Kapila, E. Lessard, and R. B. Uhl. Us9684919b2 - item delivery using 3d manufacturing on demand. Technical report, 2017.

[37] B. T. Phillips, J. Allder, G. Bolan, R. S. Nagle, A. Redington, T. Hellebrekers, J. Borden, N. Pawlenko, and S. Licht. Additive manufacturing aboard a moving vessel at sea using passively stabilized stereolithography (sla) 3d printing. *Additive Manufacturing*, 31:1407–1423, 2020.

[38] N. Leach. 3d printing in space. *Architectural Design*, 84:108–113, 2014.

[39] B. Krassenstein. Denmark shipping company, maersk, using 3d printing to fabricate spare parts on ships. `https://3dprint.com/9021/maersk-ships-3d-printers/`. Accessed: October 24, 2025.

[40] J. Savolainen and M. Collan. How additive manufacturing technology changes business models? – review of literature. *Additive Manufacturing*, 32:101070, 2020.

[41] N. J. Jensen, G. G. Parker, and J. R. Blough. Base vibration effects on additive manufactured part quality. *Experimental Techniques*, 48:159–170, 2024.

[42] J. Garofalo, R. Shah, G. Thomas, K. Shirvani, M. Marian, and A. Rosenkranz. Additive manufacturing in the maritime industry: A perspective on current trends and future needs. *Journal of Ship Production and Design*, 40:36–43, 2024.

[43] C. R. Fuller, S. J. Elliott, and P. A. Nelson. *Active control of vibration*. Academic Press, 1996.

[44] L. Lu, K. L. Yin, R. C. de Lamare, Z. Zheng, Y. Yu, X. Yang, and B. Chen. A survey on active noise control in the past decade—part i: Linear systems. *Signal Processing*, 183:108039, 2021.

[45] Y. S. Wang, H. Guo, Y. R. Li, N. N. Liu, and C. Yang. Active control for vehicle interior noise based on dwt-fxlms algorithm using a piezoelectric feedback system. *Applied Acoustics*, 167:107409, 2020.

[46] Q. Jia, Q. Li, and L. Liu. Sufficient active control of uncertain low-frequency space micro-vibrations near measurement limit of acceleration sensors. *Aerospace Science and Technology*, 149:109136, 2024.

[47] W. Li, Z. Yang, K. Li, and W. Wang. Hybrid feedback pid-fxlms algorithm for active vibration control of cantilever beam with piezoelectric stack actuator. *Journal of Sound and Vibration*, 509:116243, 2021.

[48] HBK (Hottinger Brüel & Kjær). Shaker systems | hbk world — vibration testing. `https://www.hbkworld.com/en/products/integrated-systems/vibration-testing/shaker-systems`. Accessed: October 24, 2025.

[49] Z. Guo, B. Halkon, and L. Clemon. Effects of infill parameters on the vibration characteristics of additively manufactured specimens. In *Proceedings of ISMA 2022 - International Conference on Noise and Vibration Engineering and USD 2022 - International Conference on Uncertainty in Structural Dynamics*, pages 1908–1917, 2022.

[50] Z. Guo, S. Zhao, B. J. Halkon, and L. Clemon. Simulation of active vibration control of a moving stage. pages A164–A164. The Journal of the Acoustical Society of America, AIP Publishing, 2023.

[51] Z. Guo, B. J. Halkon, and S. Zhao. Enhancing 3d printing quality: active vibration control for fdm in challenging environments. In *INTER-NOISE and NOISE-CON Congress and Conference Proceedings*, pages 946–954. Institute of Noise Control Engineering, 2025.

[52] J. Humar, A. Bagchi, and H. Xu. Performance of vibration-based techniques for the identification of structural damage. *Structural Health Monitoring: An International Journal*, 5:215–241, 2006.

[53] G. Jin, T. Ye, and Z. Su. *Structural vibration: A uniform accurate solution for laminated beams, plates and shells with general boundary conditions*. Springer, Heidelberg, 2015.

[54] Z.-F. Fu and J. He. *Modal Analysis*. Butterworth Heinemann, 2001.

[55] C. Hansen, S. Snyder, X. Qiu, L. Brooks, and D. Moreau. *Active Control of Noise and Vibration*. CRC Press, London, 2nd edition, 2012.

[56] J. H. Porter, T. M. Cain, S. L. Fox, and P. S. Harvey. Influence of infill properties on flexural rigidity of 3d-printed structural members. *Virtual and Physical Prototyping*, 14:148–159, 2019.

[57] P. K. Yadav, K. Singh Abhishek, and J. Bhaskar. Effect of infill percentage on vibration characteristic of 3d-printed structure. In *Lecture Notes in Mechanical Engineering*, pages 565–573, Singapore, 2021. Springer.

[58] K. Sreedhara, K. Reddy, and S. N. S. H. Ch. Vibration properties of 3d printed/rapid prototype parts. *International Journal of Innovative Research in Science, Engineering and Technology*, 3297:4602, 2015.

[59] M. Ö. Öteyaka, F. H. Çakir, and M. A. Sofuoğlu. Effect of infill pattern and ratio on the flexural and vibration damping characteristics of fdm printed pla specimens. *Materials Today Communications*, 33:104912, 2022.

[60] F. Medel, V. Esteban, and J. Abad. On the use of laser-scanning vibrometry for mechanical performance evaluation of 3d printed specimens. *Materials & Design*, 205:109719, 2021.

[61] F. Ali and B. V. Chowdary. Natural frequency prediction of fdm manufactured parts using ann approach. *IFAC-PapersOnLine*, 52:403–408, 2019.

[62] S. C. Ekerer, C. Boğa, M. Seyedzavvar, T. Koroglu, and T. Farsadi. Optimizing parameters for additive manufacturing: a study on the vibrational performance of 3d printed cantilever beams using material extrusion. *Rapid Prototyping Journal*, 31:218–230, 2024.

[63] B. V. Chowdary and F. Ali. Optimisation of natural frequency modes of fdm manufactured polycarbonate samples using i-optimal design and ann-ga approach. *International Journal of Quality Engineering and Technology*, 9:321–348, 2023.

[64] R. C. Parpala, D. Popescu, and C. Pupaza. Infill parameters influence over the natural frequencies of abs specimens obtained by extrusion-based 3d printing. *Rapid Prototyping Journal*, 27:1273–1285, 2021.

[65] S. Kannan, M. Ramamoorthy, E. Sudhagar, and B. Gunji. Mechanical characterization and vibrational analysis of 3d printed petg and petg reinforced with short carbon fiber. In *AIP Conference Proceedings*, page 030004. AIP Publishing, 2020.

[66] Material datasheet of carbon fiber. Technical report, Markforged, 2021.

[67] A. F. Kreger and G. A. Teters. Use of averaging methods to determine the viscoelastic properties of spatially reinforced composites. *Mechanics of Composite Materials*, 15:377–383, 1980.

[68] G. W. Melenka, B. K. O. Cheung, J. S. Schofield, M. R. Dawson, and J. P. Carey. Evaluation and prediction of the tensile properties of continuous fiber-reinforced 3d printed structures. *Composite Structures*, 153:866–875, 2016.

[69] J. F. Rodríguez, J. P. Thomas, and J. E. Renaud. Mechanical behavior of acrylonitrile butadiene styrene fused deposition materials modeling. *Rapid Prototyping Journal*, 9:219–230, 2003.

[70] Standard test method for tensile properties of polymer matrix composite materials (d3039/d3039m). Technical report, ASTM Internatinoal, 2014.

[71] R. M. Jones. *Mechanics of Composite Materials*. CRC Press, 2018.

[72] P. Böröcz and S. P. Singh. Measurement and analysis of delivery van vibration levels to simulate package testing for parcel delivery in hungary. *Packaging Technology and Science*, 31:342–352, 2018.

[73] Standard practice for performance testing of packages for single parcel delivery systems. Technical report, ASTM Internatinoal, 2025.

[74] V. Chonhenchob, S. P. Singh, J. J. Singh, J. Stallings, and G. Grewal. Measurement and analysis of vehicle vibration for delivering packages in small-sized and medium-sized trucks and automobiles. *Packaging Technology and Science*, 25:31–38, 2012.

[75] Mil-std-810h - environmental engineering considerations and laboratory tests. Technical report, Department of Defense, 2019.

[76] Standard test methods for vibration (vertical linear motion) test of products. Technical report, ASTM Internatinoal, 2022.

[77] B. Weiss, D. Storti, and M. Ganter. Low-cost closed-loop control of a 3d printer gantry. *Rapid Prototyping Journal*, 21:482–490, 2015.

[78] D. P. Desai and D. M. Patel. Design of control unit for cnc machine tool using arduino based embedded system. In *2015 International Conference on Smart Technologies and Management for Computing, Communication, Controls, Energy and Materials*, pages 443–448, 2015.

[79] Y. Chen, K. W. Kwok, and Z. T. H. Tse. An mr-conditional high-torque pneumatic stepper motor for mri-guided and robot-assisted intervention. *Annals of Biomedical Engineering*, 42:1823–1833, 2014.

[80] D. A. Vicente, R. L. Hecker, F. J. Villegas, and G. M. Flores. Modeling and vibration mode analysis of a ball screw drive. *International Journal of Advanced Manufacturing Technology*, 58:257–265, 2012.

[81] V. V. Afnani. *Stepper Motors (Fundamentals, Application and Design)*. New Age International, 2005.

[82] F. An, H. Sun, and X. Li. Adaptive active control of periodic vibration using maglev actuators. *Journal of Sound and Vibration*, 331:1971–1984, 2012.

[83] J. Liu, X. Chen, J. Gao, and X. Zhang. Multiple-source multiple-harmonic active vibration control of variable section cylindrical structures: A numerical study. *Mechanical Systems and Signal Processing*, 81:461–474, 2016.

[84] F. Li, T. Yang, W. Li, M. J. Brennan, L. Wu, and X. Li. Predicting the performance and optimizing the control parameters of an active vibration control system by pre-identifying the secondary path. *Journal of Sound and Vibration*, 568:117953, 2024.

[85] M Hu and J Lu. Active control of line spectral noise with simultaneous secondary path modeling without auxiliary noise. In *ICASSP, IEEE International Conference on Acoustics, Speech and Signal Processing - Proceedings*, pages 466–470. Institute of Electrical and Electronics Engineers Inc., 2020.

[86] B. Farhang-Boroujeny. *Adaptive Filters: Theory and Applications*. Wiley, 2013.

[87] K. Ozeki and T. Umeda. An adaptive filtering algorithm using an orthogonal projection to an affine subspace and its properties. *Electronics and Communications in Japan (Part I: Communications)*, 67:19–27, 1984.

[88] J. Da Wu, C. W. Huang, and J. C. Chen. An order-tracking technique for the diagnosis of faults in rotating machineries using a variable step-size affine projection algorithm. *NDT & E International*, 38:119–127, 2005.

[89] S. C. Douglas. The fast affine projection algorithm for active noise control. *Conference Record - Asilomar Conference on Signals, Systems and Computers*, 2:1245–1249, 1995.

[90] M. Bouchard. Multichannel affine and fast affine projection algorithms for active noise control and acoustic equalization systems. *IEEE Transactions on Speech and Audio Processing*, 11:54–60, 2003.

[91] S. Lee, I. Y. Kim, and Y. C. Park. Approximated affine projection algorithm for feedback cancellation in hearing aids. *Computer Methods and Programs in Biomedicine*, 87:254–261, 2007.

[92] Y. Pasco, O. Robin, P. Bélanger, A. Berry, and S. Rajan. Multi-input multi-output feedforward control of multi-harmonic gearbox vibrations using parallel adaptive notch filters in the principal component space. *Journal of Sound and Vibration*, 330:5230–5244, 2011.

[93] T. Yeom, T. W. Simon, M. Zhang, M. T. North, and T. Cui. High frequency, large displacement, and low power consumption piezoelectric translational actuator based on an oval loop shell. *Sensors and Actuators A: Physical*, 176:99–109, 2012.

[94] J. F. Tressler, S. Alkoy, and R. E. Newnham. Piezoelectric sensors and sensor materials. *Journal of Electroceramics*, 1998(2-4):2, 1998.

[95] Y. H. Guan, T. C. Lim, and W. S. Shepard. Experimental study on active vibration control of a gearbox system. *Journal of Sound and Vibration*, 282:713–733, 2005.

[96] M. Li, T. C. Lim, and W. S. Shepard. Modeling active vibration control of a geared rotor system. *Smart Materials and Structures*, 13:449–458, 2004.

[97] G. Pinte, S. Devos, B. Stallaert, W. Symens, J. Swevers, and P. Sas. A piezo-based bearing for the active structural acoustic control of rotating machinery. *Journal of Sound and Vibration*, 329:1235–1253, 2010.

[98] G. Zhao, N. Alujević, B. Depraetere, G. Pinte, J. Swevers, and P. Sas. Experimental study on active structural acoustic control of rotating machinery using rotating piezo-based inertial actuators. *Journal of Sound and Vibration*, 348:15–30, 2015.

[99] K. Erkorkmaz and A. Kamalzadeh. High bandwidth control of ball screw drives. *CIRP Annals*, 55:393–398, 2006.

[100] M. Hanifzadegan and R. Nagamune. Tracking and structural vibration control of flexible ball-screw drives with dynamic variations. *IEEE/ASME Transactions on Mechatronics*, 20:133–142, 2015.

[101] P. Belanger, A. Berry, Y. Pasco, O. Robin, Y. St-Amant, and S. Rajan. Multi-harmonic active structural acoustic control of a helicopter main transmission noise using the principal component analysis. *Applied Acoustics*, 70:153–164, 2009.

[102] M. Glugla and R. K. Schulz. Active vibration control using delay compensated lms algorithm by modified gradients. *Journal of Low Frequency Noise Vibration and Active Control*, 27:65–74, 2008.

[103] L. Wu, X. Qiu, and Y. Guo. A generalized leaky fxlms algorithm for tuning the waterbed effect of feedback active noise control systems. *Mechanical Systems and Signal Processing*, 106:13–23, 2018.

[104] L. Wu, X. Qiu, and Y. Guo. A simplified adaptive feedback active noise control system. *Applied Acoustics*, 81:40–46, 2014.

[105] L. Luo, J. Sun, and B. Huang. A novel feedback active noise control for broadband chaotic noise and random noise. *Applied Acoustics*, 116:229–237, 2017.

[106] H. Kim, H. Adeli, and F. Asce. Hybrid feedback-least mean square algorithm for structural control. *Journal of Structural Engineering*, 130:120–127, 2004.

[107] H. Adeli, F. Asce, and H. Kim. Wavelet-hybrid feedback-least mean square algorithm for robust control of structures. *Journal of Structural Engineering*, 130:128–137, 2004.

[108] J. Duan, M. Li, T. C. Lim, M. R. Lee, M. Te Cheng, W. Vanhaaften, and T. Abe. Combined feedforward-feedback active control of road noise inside a vehicle cabin. *Journal of Vibration and Acoustics, Transactions of the ASME*, 136, 2014.

[109] J. Pillans. Reducing position errors by vibration optimization of stepper motor drive waveforms. *IEEE Transactions on Industrial Electronics*, 68:5176–5183, 2021.

[110] S. J. Elliott. *Signal Processing for Active Control*. Academic Press, 2001.

[111] S. Kim and M. E. Altinsoy. Active control of road noise considering the vibro-acoustic transfer path of a passenger car. *Applied Acoustics*, 192:108741, 2022.

[112] S. D. Snyder and C. H. Hansen. The effect of transfer function estimation errors on the filtered-x lms algorithm. *IEEE Transactions on Signal Processing*, 42:950–953, 1994.

[113] Y. Sun, Z. Zhang, J. Zhang, X. Jin, B. Xu, Y. Deng, and G. Zhao. Effects of transient slamming and harmonic swings on the marine compound nc machine tool. *Ocean Engineering*, 108:606–619, 2015.

[114] T. R. Lin, J. Pan, P. J. O'Shea, and C. K. Mechefske. A study of vibration and vibration control of ship structures. *Marine Structures*, 22:730–743, 2009.

[115] D. Meng, W. Lu, W. Xu, Y. She, X. Wang, B. Liang, and B. Yuan. Vibration suppression control of free-floating space robots with flexible appendages for autonomous target capturing. *Acta Astronautica*, 151:904–918, 2018.

[116] L. Wang, H. Liu, L. Yang, J. Zhang, W. Zhao, and B. Lu. The effect of axis coupling on machine tool dynamics determined by tool deviation. *International Journal of Machine Tools and Manufacture*, 88:71–81, 2015.

[117] Q. Mao and S. Pietrzko. *Control of noise and structural vibration: A MATLAB®-based approach*. Springer-Verlag, London, 2013.